Torleif Weydahl

A framework for mixing-reaction closure with the Linear Eddy Model

Thesis for the degree of Philosophiae Doctor

Trondheim, June 2010

Norwegian University of Science and Technology
Faculty of Engineering Science and Technology
Department of Energy and Process Engineering

NTNU

Norwegian University of Science and Technology

Thesis for the degree of Philosophiae Doctor

Faculty of Engineering Science and Technology
Department of Energy and Process Engineering

ISBN 978-82-471-2061-3 (printed version)
ISBN 978-82-471-2062-0 (electronic version)
ISSN 1503-8181

Doctoral theses at NTNU, 2010:53

Printed by Tapir Uttrykk

Abstract

This thesis presents a novel framework for mixing-reaction closure build on the Linear Eddy Model by Kerstein (1991b). The development of the modeling concept has been motivated by the need for better predictive tools for turbulent combustion. Such tools are essential in the design of combustion technology with reduced emissions and improved efficiency, and in the development of new combustor configurations, e.g. for CO_2 capture. The original standalone Linear Eddy Model (LEM) is based on a phenomenological description of turbulent mixing on a one-dimensional domain, which can be considered to be a line of sight through the turbulent flow. LEM treats the three-dimensional advective turbulent stirring by one-dimensional stochastic re-arrangements, while the diffusive molecular mixing and the chemical reactions are solved directly.

The new framework, denoted LEM3D, extends the capabilities of the standalone LEM by creating a Cartesian three-dimensional structure of LEM domains coupled to a flow solver. Mean flow scalar advection is implemented by discrete Lagrangian displacements of LEM cells. Directional coupling is provided by random rotations of intersecting sections of LEM cells, which define a supergrid. Thermal expansions are performed by discrete dilatations. A detailed description of each part of the framework is presented in this thesis.

The present work has been focused on assessing LEM3D through a number of relatively simple test cases. It is found that the random rotations introduce additional dispersion and enhance molecular diffusion. The random rotations also cause a relatively broad distribution of travel times for a scalar through the domain.

Even though the displacements in LEM3D on average represents the prescribed velocity field, the discrete fluid cell treatment causes instantaneous deviations. A method which corrects the displacements in order to reduce these deviations has been developed.

LEM3D has also been developed to handle reacting flows by introduc-

ing discrete dilatations of LEM cells and coupling of LEM3D to a solver for the Reynolds-averaged Navier Stokes (RANS) equations. The mean density field is supplied from LEM3D to RANS, and RANS provides the updated velocity field to LEM3D. This approach leads to artifacts, due to the matching of the *non-conservative* velocities. Suggestions for future work are presented based on these results.

LEM3D has been further discussed by comparing results from a reduced dimensional version of the model (LEM2D) with experimental data from a line source in homogeneous turbulence by Warhaft (1984). The full-featured non-reacting LEM3D has been assessed by considering a scalar point source in a turbulent jet (Tong and Warhaft, 1995). The results from the non-reacting LEM3D simulations are promising considering the rather early stage of development.

Preface

First of all, I would like to thank my advisor Prof. Inge R. Gran for his positive and encouraging way of guiding me through the work. His knowledge and experience has been invaluable to my progress. I would also like to acknowledge my two co-advisors; Dr. Sigurd Sannan for fruitful discussions, for sharing his LEM-code, and for reading and commenting large parts of the thesis, and Prof. Ivar S. Ertesvåg for being available for questions and clarifications related to turbulent flows and modeling.

I am most grateful for the support that Dr. Alan R. Kerstein has given me from the early start of the project in 2005 to the finalization of the thesis. This project relies heavily on his ideas and persistent, positive encouragement. I will express my gratitude to Sandia National Laboratories in Livermore, California, and all the staff at the Combustion Research Facility for hosting me during my stays in 2005-2006 and in Sept.-Oct. 2007. Furthermore, I would also like to thank Prof. Jyh Yuan Chen for hosting me at the University of California, Berkeley in 2005-2006 , and also his students for making my time there enjoyable.

Many thanks to my colleagues at SINTEF Energy Research, in particular to Anders Gjelsvik, Andrea Gruber, Nils Erland Haugen, and Sven Tollak Munkejord, who all have participated in discussions and contributed with useful ideas along the way.

A big thanks to my office co-workers Audun Aspelund, Knut Arild Maråk, Konrad Eichorn, Lars Nord, and Liang Wang at NTNU for making the finalization stage a time to remember with joy. I am grateful to Ole Martin Hansen and Eugen Uthaug of NTNU for being helpful when PC support was needed, and to Anita Yttersian, Gerd Randi Fremstad, Gunhild V. Engdal, Toril Larssen, Wenche Johansen, and all the staff at the Department of Energy and Process Engineering for excellent administrative assistance.

Finally, I would like to thank my family for support, and my loving wife Sigrun Skårberg for encouragement when the motivation was low and

for reminding me that there are more important things in life than a PhD thesis.

Acknowledgments

This publication forms a part of the BIGCO2 project, performed under the strategic Norwegian research program Climit. The author acknowledges the partners: StatoilHydro, GE Global Research, Statkraft, Aker Clean Carbon, Shell, TOTAL, ConocoPhillips, ALSTOM, the Research Council of Norway (178004/I30 and 176059/I30) and Gassnova (182070) for their support. The cooperation with Alan R. Kerstein at Sandia National Laboratories was supported by the U. S. Department of Energy, Office of Basic Energy Sciences, Division of Chemical Sciences, Geosciences, and Biosciences.

Contents

Nomenclature

Abbreviations

3DCV Control volume in LEM3D

CFD Computational fluid dynamics

CFL Courant-Friedrichs-Lewy number

CMC Conditional moment closure

EDC Eddy dissipation concept

FV The finite volume method

IEM Interaction by exchange with the mean

LEM/LEM1D The standalone Linear Eddy Model

LEM2D The two-dimensional model framework based on LEM

LEM3D The three-dimensional model framework based on LEM

LES Large eddy simulation

ODE Ordinary differential equation

ODT The one-dimensional turbulence model

PaSR Partially stirred reactor

PFR Plug flow reactor

PSR Perfectly stirred reactor

RANS Reynolds-averaged Navier-Stokes

rms root mean square

TDMA Tridiagonal Matrix Algorithm

Greek letters

γ	Prescribed numbers of wafers displaced	-
Δ	Integer correction to the displacements	-
Δt_{w}	Diffusive time step for the LEM domain	s
Δx	3DCV size / Side face length of a wafer	m
Δx_{w}	Wafer thickness	m
Δy	3DCV size / Side face length of a wafer	m
Δz	3DCV size / Side face length of a wafer	m
δ	Number of wafers displaced over a 3DCV face	-
δ_{th}	Lower threshold for integer corrections	-
δ_r	Flame/reaction zone thickness	m
ε	Rate of turbulence energy dissipation	$\mathrm{m}^2/\mathrm{s}^3$
ε_φ	Scalar dissipation rate	$1/\mathrm{s}$
η	Kolmogorov scale	m
η_φ	Batchelor scale	m
Θ	Number of wafers that are donated or received from a domain	-
κ	Wavenumber	$1/\mathrm{m}$
λ	Event frequency parameter	$1/\mathrm{ms}$
μ_r	Statistical central r-th moment	-
μ	Dynamic molecular viscosity	kg/ms
ν_t	Turbulence viscosity	m^2/s
ν	Kinematic molecular viscosity	m^2/s
ν_r	The relative rotation frequency of 3DCVs	-
Φ	Integer expansion/dilatation factor	-

φ	General scalar quantity	-
ϱ	The spatial autocorrelation function	-
ρ	Fluid density	$\mathrm{kg/m^3}$
σ	Spreading of the mean scalar field	m
σ_t	Turbulence Schmidt-number	-
τ	The travel time for a wafer	s
τ_{adv}	Advective time scale	s
τ_{chem}	Chemical time scale	s
τ_{ij}	Cartesian stress tensor	$\mathrm{kg/(ms)^2}$
τ_t	Large eddy turnover time	s
τ_m	Mixing time	s
$\tau^{\min}$	The minimum travel time for a wafer	s
ψ	Random variable for a scalar	-
ω_φ	Chemical reaction term for φ	$\mathrm{1/s}$

Latin letters

$\mathcal{A}$	The analytical expression for scalar spreading	
b	Body force	$\mathrm{m/s^2}$
C	The prefactor to the analytical expression for scalar spreading	-
C_φ	Constant in the model for scalar dissipation rate	-
c_μ	Constant in the k-ε-model	-
d^2	The square sum of deviations	-
D_{T}	Turbulence diffusivity	$\mathrm{m^2/s}$
D_j	The jet nozzle diameter	m
D_{M}	Molecular diffusivity	$\mathrm{m^2/s}$
E	Turbulence energy spectrum	$\mathrm{m^3/s^3}$

$\mathbf{f}$	Probability density function	-
$\widetilde{F}$	Control volume boundary mass flow in RANS	$^{\mathrm{kg}}/_{\mathrm{s}}$
f	Event size distribution	-
f_{nn}	The velocity fraction of the maximum velocity at face nn	-
H	Turbulence generating grid width	m
I	Turbulence intensity	-
K_{ν_t}	Constant determining the spatial variation of the turbulence diffusivity	
K_u	Constant determining the Gaussian shape of the jet velocity profile	
k	Turbulence energy	$^{\mathrm{m}^2}/_{\mathrm{s}^2}$
k	The number of wafers involved in a triplet map is $3k$	-
$k_{\max}$	The largest triplet map involves $3k_{\max}$ wafers	-
$k_{\min}$	The smallest triplet map involves $3k_{\min}$ wafers	-
L	LEM integral scale / Size of the largest triplet map	m
L_{K}	LEM Kolmogorov scale	m
L_{K}^*	The size of the smallest triplet map	m
l	Turbulence length scale	m
l_t	Turbulence integral scale	m
M	1D-resolution of LEM domains	-
$\mathbf{n}$	Surface normal vector	-
N_s	The total number of samples	-
N_{p}	The total number grid nodes	-
N_{t}	The total number of time steps	-
N_x	Number of LEM domains in the x-direction	-
N_y	Number of LEM domains in the y-direction	-

N_z	Number of LEM domains in the z-direction	-
P	The probability of a function	-
p	Thermodynamic pressure	Pa
p^+	Pressure indicator	Pa
Pe	Peclet number	-
$\mathcal{R}$	The rotation frequency	$^1/_\mathrm{s}$
R	The mean rate of triplet map events	1/s
Re_j	Jet Reynolds number	-
Re_S	LEM Reynolds number	-
Re_t	Turbulence Reynolds number	-
R_φ	Scalar spatial autocovariance function	-
R_{ij}	Autocorrelation between velocity components	$^{\mathrm{m}^2}/_{\mathrm{s}^2}$
R_mix	Mixture gas constant	$^\mathrm{J}/_{(\mathrm{kg\ K})}$
$r_{1/2}$	The half-width of the jet at a given position	m
r	Residual from the prescribed displacements	-
r	Radial coordinate with Cylindrical coordinates	m
S	Surface Area	m^2
Sc	Molecular Schmidt-number	-
Sc_S	The LEM viscous cut-off Schmidt number	-
t	Time	s
t_j	Time for a given time step j	s
T	Temperature	K
T_L	Model eddy turnover time	s
T_pt	The time spend for one time step on each grid node	-
T_tot	The total simulation time	-

U_c	The mean jet center velocity	$^{m}/_{s}$
U_j	The jet exit velocity	$^{m}/_{s}$
$\mathbf{u}$	Fluid velocity vector	$^{m}/_{s}$
u	Fluid velocity	$^{m}/_{s}$
V	Volume	m^3
v	Random variable for velocity	$^{m}/_{s}$
w	Wafer velocity	$^{m}/_{s}$
$w^{'}$	The jitter of the wafer velocity (see Chapter 5.2.1)	$^{m}/_{s}$
w^{*}	The normalized jitter of the wafer velocity	$^{m}/_{s}$
X	Size of the LEM3D domain in the x-direction	m
$\boldsymbol{X}^0$,X_i^0	Particle reference position	m
X^+	Particle position	m
x_0	The streamwise position of the point source /line source	m
$\mathbf{x}$	Position vector	m
x_{virt}	The virtual origin of the jet	m
Y	Size of the LEM3D domain in the y-direction	m
Z	Size of the LEM3D domain in the z-direction	m

Subscripts and indices

b	Index denoting the bottom face of a 3DCV	-
cl	Centerline	-
e	Index denoting the east face of a 3DCV	-
i, j	Spatial indices	-
l	Index specifying a wafer in the 3DCV	-
n	Index denoting the north face of a 3DCV	-
nn	Index denoting a general 3DCV or control volume surface	-

p_d	The wafer positions below 3DCV centers	-
p_u	The wafer positions above 3DCV centers	-
p	Spatial wafer index within a given LEM domain	-
q	3DCV index in x-direction	-
r	Spatial index in Cylindrical coordinates	-
r	3DCV index in y-direction	-
s	Index denoting the south face of a 3DCV	-
s	3DCV index in z-direction	-
t	Index denoting the top face of a 3DCV	-
w	Index denoting the west face of a 3DCV	-
x	Spatial index in Cartesian/Cylindrical coordinates	-
y	Spatial index in Cartesian coordinates	-
z	Spatial index in Cartesian coordinates	-

Superscripts

j	Time or sample index	-

Chapter 1

Introduction

1.1 Motivation and scope

In efficient and successful commercial design of combustion equipment, the use of validated predictive tools that describe the relevant aspects of the combustion physics is crucial in order to increase efficiency, reduce emissions and develop new concepts e.g. related to new combustor configurations for CO_2 capture. The car engine, the gas turbine combustion chamber and the industrial furnace are all operated at high flow rates for optimum energy output, which induces turbulent, chaotic behavior. Turbulent flows are characterized by three-dimensional, rotational, irregular, intermittent structures on a wide range of scales (Bradshaw, 1971; Hinze, 1975; Pope, 2000). Turbulence appears also in nature for instance in atmospheric and oceanic flows (Sreenivasan, 1999; Warhaft, 2002). More knowledge of such phenomena is central to a better understanding of the earth's climate and the global temperature trends. Turbulence is still regarded as one of the unsolved problems in physics, even though the equations for these processes basically are known. The reason is that the broad range of scales in most practical problems renders the accurate direct numerical simulation (DNS) unfeasible because of the tremendous computer resources required to perform the simulations. Since DNS generally is out of reach, models that simplify the problem by limiting the resolved range of scales have been the solution for scientific and engineering purposes. The compromise is that the turbulent stirring, which by nature is an *advective* process, is treated by *diffusive* models. This blurs the distinction to molecular diffusive mixing and complicates the determination of the chemical reaction rates. In this lies the essential challenge of turbulent combustion modeling, which is the main motivation for the present work.

One model that does capture the distinction between the advective turbulent stirring and the diffusive molecular mixing is the Linear Eddy Model (LEM) developed by Kerstein (1991b). The LEM is based on a phenomenological description of turbulent mixing. All relevant length scales are resolved in one dimension which renders the model affordable even for reacting flows at higher Reynolds-numbers. The trade-off is that the effect of three-dimensional turbulent eddies is *emulated* by stochastic rearrangements of fluid elements on the one-dimensional (1D) domain. The model is run by time stepping the 1D reaction-diffusion equations punctuated by the rearrangements or mapping events.

Consider a scalar emerging in a turbulent flow depicted in Figure 1.1. The turbulent eddies act on the scalar field by continuously compressing and folding the scalar structures. This process enhances the scalar gradients and increases the mixing by molecular diffusion, which is the necessary precursor for chemical reactions. The mapping scheme applied in LEM, which is denoted the *triplet map*, mimics this process by creating three (triple) compressed copies of a segment of the scalar field. By inverting the center copy, the mapping maintains the property of a continuous scalar field. The triplet map sizes are selected with a given rate from a distribution, which represents the scaling of the turbulence spectrum in the inertial range. One of the most comprehensive descriptions of the model is given in Kerstein (1991b). Further details of the LEM are presented here in Sections 3.2 and 4.3.

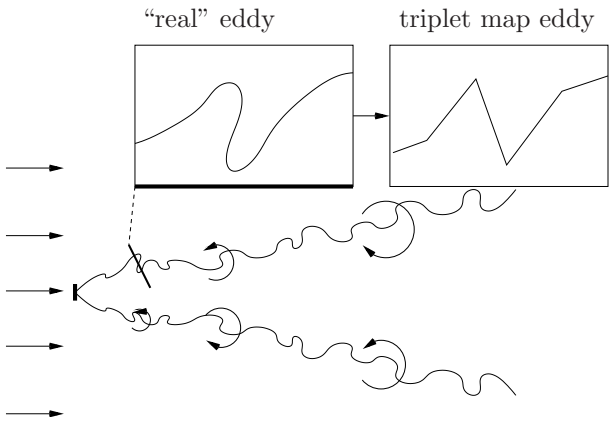

Figure 1.1: A schematic illustration of spreading of a scalar in a turbulent flow. The left box is the “real” effect of an eddy on the scalar gradient normal to the scalar iso-surface. The right box shows the triplet map model of such an eddy event.

The LEM in standalone 1D mode is limited to a simplified representation of the flow geometry which curbs the range of possible applications. Thus, the aim of the present work has been to extend LEM to general reacting flows by creating a three-dimensional structure of LEM domains and couple the structure to a *flow solver*.[1] The principal guideline for the model development has been that the distinction between advective and diffusive processes should be maintained. Hence, the present model treats mean flow advection and thermal heat release as discrete non-diffusive processes.

The work is limited to free shear flows, thus near-wall effects are not considered.[2] The focus of the present work is on assessing the novel elements and the potential of the modeling concept. Hence, relatively simple and transparent steady-state flow configurations are considered. The treatment of chemical reactions and volumetric expansion is still at an early stage of development; however, a strategy to arrive at a more mature representation is outlined. Other combustion related issues such as radiation, soot formation and treatment of particles are omitted.

1.2 Previous work

The topic of turbulent combustion modeling is vast. A brief introduction is given in Sec. 2.4, however, we generally refer to the books by Pope (2000), Warnatz *et al.* (2001), Veynante and Vervisch (2002), and Fox (2003) for more complete reviews. Here we consider LEM and the one-dimensional turbulence (ODT) model only. The ODT extends LEM by also evolving the velocity field (Kerstein, 1999). Even though this work is limited to LEM, ODT is also considered in the following brief review since common issues arise with flow solver coupling.

1.2.1 Standalone non-reacting applications

The standalone 1D LEM has been adapted and utilized to simulate a considerable amount of different applications. In the various cases, the interpretation of the LEM domain changes with the alignment in the flow (McMurtry *et al.*, 1993). Mixing in homogeneous turbulence with a uniform passive scalar gradient is studied in Kerstein (1988, 1991a,b); Kerstein

[1] The term *flow solver* is used for a solver that provides the mean flow quantities. This is generally Reynolds-averaged Navier-Stokes (RANS) or Large Eddy Simulation (LES) for turbulent flows. See Sec. 2.4.3 for further description.

[2] A structure of ODT-domains has successfully been utilized to improve modeling of wall-bounded flows by Schmidt *et al.* (2003). ODT is briefly explained in Sec. 1.2.

et al. (1995). For these cases, the 1D LEM domain is aligned with the mean scalar gradient. Mixing in homogeneous turbulence with scalar point and line sources or a two-stream shear layer is reported in Kerstein (1989), where the domain represents a transverse line moving with the flow. In the latter case, the growth of the shear layer is an empirical input to the model. This is implemented by confining the rearrangement events to the growing shear layer.

Mixing in round jets is presented in Kerstein (1990) where the domain represents a radial line in the jet that moves streamwise with the flow. The radial variation of streamwise velocity is neglected. The growth of the vortical zone is implemented by letting the upper bound on stirring events, and hence the model integral scale, vary with axial position.

Atmospheric science is one of many areas of application of LEM and ODT. LEM has been utilized to calculate the entrainment of air in a stratus cloud (Krueger (1993); Krueger *et al.* (1997)). The 1D-domain is oriented horizontally in the cloud and moves vertically with the downdraft. The entrainment is modeled explicitly. Su *et al.* (1998) accounts in addition for droplet growth and the results yield good agreement with droplet spectra obtained from airplane measurements. The ODT model takes the buoyancy effect on turbulence into account, and several works study atmospheric flows where density gradients are important (Kerstein, 1999; Wunsch and Kerstein, 2001; Wunsch, 2003).

1.2.2 LEM and ODT in turbulent combustion modeling

Due to the full resolution of scales in LEM and ODT, the incorporation of chemical reactions requires no additional modeling. The models have no presumption of whether the reactants are *premixed* before reaction, or if the reactants are introduced separately and react as they mix as in *non-premixed* combustion. The 1D standalone reacting LEM/ODT has been used for several applications and combustion regimes.

When thermal expansion from heat release is negligible, the extension of LEM to reacting flow is straightforward. Frankel *et al.* (1995) calculate binary scalar mixing and isothermal reaction in homogeneous turbulence, and Kerstein (1992b) successfully simulates the reactive mixing layer of nitric oxide and ozone.

Turbulent non-premixed flames are simulated with infinite-rate (Kerstein, 1992a) and finite-rate (Menon *et al.*, 1992, 1994) chemical kinetics. In these applications, the LEM domain is oriented in the streamwise direction on the axis of the jet. Varying LEM cell volumes reflects the downstream growth of the jet. Fuel is introduced by inserting fuel cells in the upstream

part of the domain. The entrainment of air is implemented explicitly by randomly inserting fluid parcels with size characteristic to the local jet diameter. Thermal expansion from heat release is modeled by transferring portions of the cell content to downstream parcels. Multi-species transport with differential diffusion effects is included in Calhoon *et al.* (1995). They compare reduced and full chemical mechanisms for non-premixed turbulent H_2-air jet flames.

Turbulent premixed flames have also been studied using LEM (Smith and Menon, 1996, 1997; Sankaran and Menon, 2000). The premixed flame travels along the LEM domain, which is set up with a moving observation window to avoid the flame to extend out of the domain. Different chemical mechanisms have been applied as well as a G-field approach that considers transport of one or several flame fronts. The latter is primarily applicable to combustion in the flamelet regime. Sankaran and Menon (2000) employ a detailed chemistry model and study combustion in several flame regimes.

In Echekki *et al.* (2001); Hewson and Kerstein (2001), a non-premixed turbulent diffusion jet flame is simulated by a radial ODT-domain that moves downstream with the bulk flow. The chemical integration time is adjusted to account for residence time variation in the radial direction of the jet.

Computational cells of equal size (i.e., width) are currently a necessity for the triplet mapping applied in ODT and LEM. This restriction affects the implementation of thermal expansion from heat release. A frequently used approach is to increase the cell volume and perform a regridding operation before every triplet map event (Sankaran and Menon, 2000; Echekki *et al.*, 2001). The regridding will inevitably introduce artificial diffusion. Another approach, which has been utilized in the present work, is to account for thermal expansion by creating new cells in integer steps (Menon and Calhoon, 1996). A third option is to let the expansion induce a flow out of the fluid cell in an Eulerian manner (Oevermann *et al.*, 2008). The latter option will also cause artificial diffusion, since fluid will cross the fluid cell boundary and mix with the adjacent cells.

In total, LEM and ODT have been used to simulate a considerable range of practical cases from cloud formation (Su *et al.*, 1998), through HCCI[3] combustion (Oevermann *et al.*, 2008), to supernova explosions (Woosley *et al.*, 2008). Even though the results from the works are promising, the representation of multi-dimensional flows is still limited by the 1D formulation. Thus, in order to be able to represent e.g. complex atmospheric flows or gas turbine combustion chambers, a coupling to multi-dimensional flow

[3]Homogeneous Charge Compression Ignition

solvers is needed.

1.2.3 LEM and ODT as subgrid models

The methods for coupling between LEM/ODT and a flow solver can be subdivided into direct or indirect methods. In the indirect methods, LEM/ODT provides submodels for the scalar or turbulence stress closure through tabulation given by a number of pre-runs. For the direct methods, the flow solver evolves concurrently with LEM/ODT, and the two are linked by one-way or two-way exchange of information.

Indirect methods

In contrast to the assumed probability density function (pdf) methods where the shape of the pdf is assumed *a priori* (see e.g. Sec. 2.4.3), the constructed pdf method by Goldin and Menon (1997) determines the shape of the pdf from simulations with LEM of scalar distribution in homogeneous turbulence. The constructed pdf is parameterized by the first two statistical moments. Comparison with assumed β-pdf and experiments is given in Goldin and Menon (1998); Goldin (2005). A slightly different approach is provided by Sankaran *et al.* (2009). They use LEM simulations along with experimental data to create a tabulated closure for LES. The closure is parameterized by the LES filtered scalar dissipation rate and the filtered Reynolds-number, and hence is better customized to LES. LEM has also been used to assess mixing-reaction models, specifically the flamelet model and conditional moment closure (CMC) in Desjardin and Frankel (1996, 1997).

Where LEM provides the subgrid closure for the scalar, ODT gives the subgrid turbulence stresses for closure of the momentum equation. Ranganath and Echekki (2006, 2008) use ODT to generate look-up tables for the density needed in a RANS solver. The ensemble mean closure (EMC), which is a closure model (eddy-viscosity type) for the sub-grid LES stresses, is introduced by McDermott *et al.* (2005). The model is derived entirely from ODT.

Direct methods

The direct methods can be categorized as Eulerian or Lagrangian, depending on how the LEM subdomains relate to the processes on the LES domain (Kerstein, 2002). For the Eulerian methods, one LEM domain is assigned

to each LES cell, whereas the Lagrangian methods transport the individual subgrid elements with the LES/RANS predicted flow.

Pit *et al.* (2007) pursue a Lagrangian approach where the individual Lagrangian particles constitute LEM sub-structure.

The approach of (Menon *et al.*, 1993) is Eulerian in the sense that every LES cell has one associated LEM domain. The LEM domain, which in this case has no specific orientation, interacts with its neighboring domains through a splicing operation.[4] The model, often referred to as LEMLES, has been applied to both premixed (Menon *et al.*, 1993; Chakravarthy and Menon, 2001; Sankaran and Menon, 2005) and to non-premixed combustion (Menon *et al.*, 1993; McMurtry *et al.*, 1992a,b; Menon and Calhoon, 1996) for a variety of combustion regimes. An attractive feature of LEMLES (as well as the standalone LEM) is the absence of application-specific adjustments, i.e., the model does not need to be adapted to different combustion regimes. Goldin *et al.* (1995) pursues an LEM-RANS approach, where, in essence, the splicing procedure described above handles the mean scalar advection, while a separate "diamond" mapping is developed for the large scale turbulence transport. To this author's knowledge, no further publications have been released on the LEM-RANS.

The ODT model can provide the subgrid turbulence stresses to a flow solver. In Kerstein *et al.* (2001); Schmidt *et al.* (2003) the ODT has been used to supply the subgrid turbulence stresses close to a wall, which generally is a challenge to LES due to the high resolution requirement. The sub structure constitutes ODT-domains that are oriented perpendicular to the wall. Coupling of ODT-domains in the direction parallel to the wall is provided by finite differencing. This approach is further developed by Schmidt *et al.* (2005, 2008) to yield a three-dimensional (3D) formulation. ODT-lines are orthogonally oriented on a 3D Cartesian LES grid. Transport transverse to the ODT-lines is implemented by interpolation from the nearest transverse ODT-lines. Continuity is enforced on the 3D level by a pressure projection method. The resolved transport is transferred to the subgrid structure by a reconstruction method that preserves the small scale structure. Cao and Echekki (2008) have built a LES substructure of ODT-domains in 3D similar to Schmidt *et al.* (2005), but with a different approach for advective coupling between the ODT-domains.

In the approaches mentioned in the previous paragraph, finite differencing is used for the fluxes normal to the resolved 1D-domains. The splicing operation as presented in Sankaran (2003) involves regridding after non-

[4]The splicing operation has been subject to major revisions from Menon *et al.* (1993) to Sankaran (2003)

integer LEM cell advection. Thus, these approaches introduce artificial diffusion. Kerstein (2002) has suggested replacing this scheme by a method transferring fluid packets in between domains. This method involves a coupling of ODT and LES where the main idea is to avoid blurring the distinction between molecular diffusion and turbulent stirring.

1.3 The LEM3D approach

The work presented here introduces a novel framework for mixing-reaction closure with LEM as the main building block. In contrast to the LEMLES approach (Menon *et al.*, 1993), the LEM domains have physical orientation in space. The model structure is based on the work presented in Schmidt *et al.* (2005, 2008). However, in this work, the distinction between turbulent stirring and molecular diffusion is preserved through an LEM domain coupling by non-diffusive Lagrangian fluid cell displacements rather than Eulerian finite differencing. Besides the LEM processes previously presented, the model constitutes the following elements: Mean flow advection by discrete Lagrangian displacements of fluid cells, discrete implementation of fluid cell dilatations from heat release, and a necessary auxiliary coupling by random rotation of supergrid[5] control volumes. The fluid cells are characterized as *wafers* due to their shape, and the supergrid control volumes are denoted *3DCVs*.

The model, which is given the name LEM3D, has been developed as a joint effort, where the conceptual ideas of Kerstein (2002, 2004, 2009) through the collaboration Kerstein *et al.* (2007, 2005-2006) have been implemented by Sannan *et al.* (2008, 2009) and further developed and tested in the present work. The model is also described in Weydahl *et al.* (2007). The specific contributions to the different parts are pointed out in the main text.

The main contributions presented in this thesis are as follows:

- A detailed and complete description of the modeling framework and the numerical implementation.
- A novel method for reducing the deviations related to the discrete representation of mean flow advection has been developed, implemented and assessed.
- The LEM3D has been extended to non-reacting flows by developing and implementing an algorithm for discrete dilatation of wafers and

[5]Defined in Sec. 4.2.

establishing a coupling to a RANS flow solver. The artifacts related to this treatment of dilatations are pointed out, and suggestions for improvements are proposed.

- Essential characteristics of the LEM3D have been investigated through a number of test cases. Several issues are related to the random rotations of 3DCVs; the degree of directional coupling of LEM domains, the amount of additional dispersion and mixing, and the residence time distribution. In addition, the discrete representation of the mean flow advection has been evaluated.

- The non-reacting LEM3D has been utilized to simulate passive scalar mixing from a point source placed in grid turbulence and the self-similar region of a turbulent jet. Sensitivity to resolution, frequency of random rotations, and the selected LEM integral scale have been investigated. The results are compared to experimental data from Warhaft (1984) and Tong and Warhaft (1995) for the grid and jet turbulence cases, respectively. Numerical solutions to model transport equations for the scalar mean and variance have also been employed for comparison.

1.4 Survey of the thesis

The present work has been focused on assessing LEM3D through a number of relatively simple test cases. Tab. 1.1 gives an overview of the various cases considered and the model elements of LEM3D that are included for each case. The LEM processes refer to molecular mixing and triplet map stirring.

In Chapter 2 the foundation for the physical and statistical description of reacting flows is presented. A brief review of the models for turbulent mixing and reaction is given, and the role of LEM in this context is discussed. The chapter also presents a phenomenological description of scalar mixing for some basic turbulent flows.

Chapter 3 presents the established models including the standalone 1D LEM that are utilized in the present work. In addition, a conceptual equation for scalar transport in the applied framework is given.

The modeling concept, the mathematical formulation, and the numerical implementation and simulation procedure for the reacting LEM3D are presented in Chapter 4. A simplified two-dimensional version of LEM3D, denoted LEM2D, which is utilized to study the isolated effects of random

3DCV rotations, is also presented. The computational cost is considered and compared to DNS.

The discrete representation of the mean flow advection and the auxiliary coupling by random rotations have been thoroughly studied in Chapter 5 and 6. Chapter 5 considers the discrete representation of the mean shear flow in a turbulent jet. The wafer residence time in a quasi 1D channel is also studied. Chapter 6 presents results of dispersion of a passive scalar in grid turbulence (Warhaft, 1984) and investigates the effects of random rotations.

Chapter 7 presents the model for discrete dilatation. The model is evaluated by considering a simple artificial numerical test case.

Chapter 8 compares simulations with LEM3D and experimental data of Tong and Warhaft (1995) of scalar dispersion from a point source in the self-similar region of a turbulent jet. The results are also compared to numerical solutions of model transport equations for the scalar mean and variance.

A summary of the main findings and some concluding remarks are given in Chapter 9 along with recommendations for further work.

Table 1.1: Overview of the various cases considered and the LEM3D model elements that are included in each of them. The LEM processes constitute molecular mixing and triplet map stirring.

	A1	A2	B1/B2	C	Jet passive mixing
Chapter	5.2	5.3	6	7	8
LEM processes			X		X
Random rotations		X	X	X	X
Mean scalar advection	X	X		X	X
Thermal expansion				X	

Chapter 2

Theoretical background

2.1 Introduction

Turbulent flows are characterized by random velocity fluctuations in time and space (Hinze, 1975). This does not, however, mean that the velocity field evolves in an unpredictable way. It is always governed by the Navier-Stokes equations[1], but due to the non-linear terms in these equations that are inherently sensitive to small perturbations, random behavior arises at high Reynolds numbers.

The physical background of the continuum description of fluids implies that the molecular mean free path, i.e., the average distance molecules travel between collisions with partner molecules, is orders of magnitude smaller than any macroscopic scale of the flow; for instance the gradient scales of the velocity - and temperature fields. When we observe the continuum properties of for instance air at atmospheric conditions in a wind tunnel at $1\,\mathrm{m/s}$, we actually measure the average effect from about 20 quintillions (10^{18}) of molecules per second that passes over a probe volume of about $1\,\mathrm{mm}^3$. The *continuum hypothesis* states that the fluid and its macroscopic properties are continuously distributed over the space that the fluid occupies (Pope, 2000; Irgens, 2004). The hypothesis is the underlying assumption for all fluid equations in this thesis.

This chapter briefly reviews the foundation for the physical and statistical description of reacting flows. A brief review of the models for turbulent mixing and reaction is also given. Finally, a phenomenological description of scalar mixing in basic turbulent flows is presented.

[1]The statement presupposes that the fluid is a Newtonian fluid, which is described by a linear stress-strain relationship. This work considers Newtonian fluids only.

2.2 Conservation equation

2.2.1 Mass conservation

Neglecting the mass sources and sinks from nuclear reactions, the mass for a defined system is conserved. This can be represented by the continuity equation

$$\frac{\partial \rho}{\partial t} + \frac{\partial}{\partial x_j}\left(\rho u_j\right) = 0, \tag{2.1}$$

where ρ is the density and u_j is the velocity component in the direction x_j.[2]

2.2.2 Momentum conservation

The momentum equation for a continuum fluid is given by

$$\frac{\partial}{\partial t}(\rho u_i) + \frac{\partial}{\partial x_j}\left(\rho u_j u_i\right) = \frac{\partial}{\partial x_j}(\tau_{ij}) + \rho b_i, \tag{2.2}$$

and follows from Euler's first axiom (Irgens, 2004), which corresponds to Newton's second law of motion. The Cartesian stress tensor τ_{ij} represents the effect of pressure and viscous forces on the fluid acceleration and b_i is the effect from body forces as for instance gravitation. Applying Stokes' postulates and hypothesis (White, 1991), and assuming the fluid to be Newtonian, we obtain the *Navier-Stokes* equations

$$\begin{aligned}\frac{\partial}{\partial t}(\rho u_i) + \frac{\partial}{\partial x_j}\left(\rho u_i u_j\right) = \\ -\frac{\partial p}{\partial x_j} + \frac{\partial}{\partial x_j}\left[\mu\left(\frac{\partial u_i}{\partial x_j} + \frac{\partial u_j}{\partial x_i} - \frac{2}{3}\frac{\partial u_k}{\partial x_k}\delta_{ij}\right)\right] + \rho b_i,\end{aligned} \tag{2.3}$$

where μ is the dynamic viscosity and p is the pressure. The bulk viscosity is zero in the expression (2.3) above (White, 1991).

2.2.3 Scalar conservation

The general transport equation for a reactive scalar φ is written as

$$\frac{\partial(\rho\varphi)}{\partial t} + \frac{\partial}{\partial x_j}\left(\rho u_j \varphi\right) = \frac{\partial}{\partial x_j}\left[\rho D_{\mathrm{M}} \frac{\partial \varphi}{\partial x_j}\right] + \rho\omega_\varphi, \tag{2.4}$$

where ω_φ is the reaction source or sink term. Note that the equation above assumes a gradient type model for the diffusive flux, and also assumes that

[2] Einstein's summation convention is applied (White, 1991)

the molecular diffusivity D_{M} is represented by a mixture averaged quantity. With these assumptions, if φ in Eq. (2.4) is replaced by the mass fraction Y_k of species k, the equation is valid if we apply Fick's law for mass diffusion with a mixture averaged diffusion coefficient D_k and neglect contributions from thermal (the Soret effect) and pressure diffusion (see e.g. Bird *et al.* (1960)).

When the reaction term $\rho\omega_\varphi$ in Eq. (2.4) is zero, φ is considered a *conserved scalar* since it has no sinks or sources. In two-stream mixing cases, the *mixture fraction* is a conserved scalar that determines the amount of elements from stream 1 and 2 through a linear relation (Bilger, 1976). A *passive scalar* has no direct effect on the material properties of the flow as the density, viscosity and transport properties (Pope, 2000). Assuming no spatial variation of the density and the diffusivity due to other sources, the transport equation for a passive reacting scalar can be written as

$$\frac{\partial \varphi}{\partial t} + \frac{\partial}{\partial x_j}\left(u_j \varphi\right) = D_{\mathrm{M}} \frac{\partial^2 \varphi}{\partial x_j \partial x_j} + \omega_\varphi. \tag{2.5}$$

In the present work we assume that the scalar transport can be described by Eq. (2.4) for flows with varying density and Eq. (2.5) when the density and diffusivity are constant. The multicomponent energy transport in terms of temperature will require additional transport terms. Further details are found in textbooks (Bird *et al.*, 1960; Warnatz *et al.*, 2001).

2.3 Statistical description of scalar mixing in turbulent flows

2.3.1 Statistical description of turbulent flows

Let $u_i(\mathbf{x}, t)$ be the random velocity field. For a fixed time $t = t^*$, the velocity varies randomly with respect to $\mathbf{x}$. For a fixed position $\mathbf{x}^*$, u_i is a random process with respect to t (Pope, 2000). At given time and position, the velocity component u_i is completely determined by the one-point probability density function (pdf)

$$\mathbf{f}_{u_i}(v_i; \mathbf{x}, t) dv_i \equiv P\left\{v_i \leq u_i(\mathbf{x}, t) \leq v_i + dv_i\right\}, \tag{2.6}$$

where v_i is the sample space variable for u_i, and $\mathbf{f}_{u_i}(v_i; \mathbf{x}, t)dv_i$ is the probability that u_i is in the interval between v_i and $v_i + dv_i$. With the pdf known, the mean velocity component is directly given from the mathematical expectation

$$\overline{u}_i(\mathbf{x}, t) \equiv \int_{+\infty}^{\infty} v_i \mathbf{f}_{u_i}(v_i; \mathbf{x}, t) dv_i, \tag{2.7}$$

as well as all higher order statistical moments. It is important to notice that the pdf does not completely describe the random processes, $u_i(\mathbf{x}, t)$, in sufficient detail. The random velocity gradient in the x_1 direction defined by

$$\frac{\partial u_i(x_1, x_2, x_3, t)}{\partial x_1} \equiv_{\lim(x_1 - x_1^*) \to 0} \frac{u_i(x_1, x_2, x_3, t) - u_i(x_1^*, x_2, x_3, t)}{x_1 - x_1^*}, \quad (2.8)$$

can for instance not be determined unless we have simultaneous information from the points (x_1, x_2, x_3) and (x_1^*, x_2, x_3). The general two-point pdf is defined by

$$\begin{aligned} \mathbf{f}_{u_i, u_i^*}(v_i, v_i^*; \mathbf{x}, t) dv_i \equiv & P\left\{v_i \leq u_i(\mathbf{x}, t) \leq v_i + dv_i\right\} \\ & \cap P\left\{v_i^* \leq u_i^*(\mathbf{x}, t) \leq v_i^* + dv_i^*\right\}. \end{aligned} \quad (2.9)$$

The fluctuating velocity component in the Cartesian x_i-direction is given from the Reynolds decomposition as

$$u_i^{'} \equiv u_i - \overline{u}_i. \quad (2.10)$$

The turbulence energy[3] is defined as $k \equiv \frac{1}{2}\overline{u_i^{'} u_i^{'}}$ (Reynolds, 1895). This property is exactly given if the one-point velocity pdf (2.6) is known. A transport equation for the turbulence energy can be derived by applying the Reynolds decomposition to the momentum equation (2.3) and taking the average. By this derivation, the dissipation rate of turbulence energy appears as

$$\varepsilon \equiv \overline{\tau_{ij}^{'} \frac{\partial u_i^{'}}{\partial x_j}}. \quad (2.11)$$

From the discussion above, we realize that an exact representation of this term requires that the two-point pdf (2.9) is known. Another statistical property that requires two- or multi-point information is the velocity correlation defined by

$$R_{ij}(\mathbf{r}, \mathbf{x}, t) \equiv \overline{u_i^{'}(\mathbf{x}, t) u_j^{'}(\mathbf{x} + \mathbf{r}, t)}. \quad (2.12)$$

This multi-point correlation function contains information needed to predict turbulence length scales and the turbulence energy spectrum.

[3]Often denoted the turbulence *kinetic* energy

2.3.2 Statistical description of scalar mixing

We consider a scalar field $\varphi(\mathbf{x},t)$ in a turbulent flow. The flow has strong influence on the scalar, and we need the joint information of velocity and scalar fields to describe the random turbulent scalar mixing process. The one-point joint velocity scalar pdf is defined as

$$\begin{aligned}\mathbf{f}_{\varphi,u_i}(\psi,\mathbf{v};\mathbf{x},t)d\psi d\mathbf{v} \equiv \\ P\left\{\psi \le \varphi(\mathbf{x},t) \le \psi + d\psi\right\} \cap P\left\{v_i \le u_i(\mathbf{x},t) \le v_i + dv_i\right\},\end{aligned} \tag{2.13}$$

where ψ is the sample space variable for the scalar φ. $\mathbf{f}_{\varphi,u_i}(\psi,v_i;\mathbf{x},t)d\psi$ is the probability that φ lies in the interval between ψ and $\psi + d\psi$ and, while at the same time, u_i in the interval between v_i and $v_i + dv_i$. The one-point scalar pdf can be found by integrating over the velocity sample space

$$\mathbf{f}_{\varphi}(\psi;\mathbf{x},t) = \iiint_{-\infty}^{\infty} \mathbf{f}_{\varphi,u_i}(\psi,v_i;\mathbf{x},t)dv_i. \tag{2.14}$$

With the pdf known, the mathematical expectation (the mean) of the scalar can be calculated by

$$\overline{\varphi} = \int_{-\infty}^{\infty} \psi \mathbf{f}_{\varphi}(\psi;\mathbf{x},t)d\psi, \tag{2.15}$$

as well as all higher order statistical *central moments* given by

$$\mu_r = \int_{-\infty}^{\infty} (\psi - \overline{\varphi})^r \mathbf{f}_{\varphi}(\psi;\mathbf{x},t)d\psi. \tag{2.16}$$

The scalar pdf is often far from Gaussian, even in cases when the velocity field resembles Gaussian shape (Warhaft, 2000). One example is binary mixing in homogeneous turbulence, where the pdf evolves from a non-Gaussian shaped pdf. One of the major challenges in the modeling of turbulent mixing is developing models that describe the evolution of the scalar pdf.

A scalar subject to turbulent fluctuations can be decomposed in terms of its mean and instantaneous value such that $\varphi' \equiv \varphi - \overline{\varphi}$. Similar to the turbulence energy, a "scalar fluctuation intensity" equation commonly denoted the *scalar variance* ($\overline{\varphi'^2}$) equation can be derived by applying the decomposition to the scalar transport equation (2.5). The dissipation rate of scalar variance is usually referred to as the *scalar dissipation rate*, and is defined by

$$\varepsilon_{\varphi} \equiv 2D_{\mathrm{M}} \overline{\frac{\partial \varphi'}{\partial x_i} \frac{\partial \varphi'}{\partial x_i}}. \tag{2.17}$$

As for the velocity pdf, neither the one-point scalar pdf (2.14) nor the one-point joint scalar velocity pdf (2.13) include length-scale information and

hence no exact estimate of the scalar dissipation rate. This is provided only by two-point statistics. The scalar spatial *autocovariance* function, given by

$$R_\varphi(\mathbf{r}, \mathbf{x}, t) \equiv \overline{\varphi'(\mathbf{x}, t)\varphi'(\mathbf{x}+\mathbf{r}, t)} \tag{2.18}$$

from spacial points at $\mathbf{x}$ and $\mathbf{x}+\mathbf{r}$, can be constructed from such information. Scalar length scales and the scalar power spectrum can be derived from the autocovariance function (2.18).

2.4 Modeling of scalar mixing and reaction — a brief review

Modeling scalar mixing in turbulent flows has been a challenge for scientists and engineers for more than a century. The phenomenon appears within several fields ranging from atmospheric science; how pollution spreads in water and air, cloud formation, to engineering applications; in gas turbines, internal combustion engines, and fires, among several.

In a well *macromixed* field, scalars are distributed homogeneously on the larger scale and are independent of $\mathbf{x}$. Hence, the scalar pdf (2.14) becomes $\mathbf{f}_\varphi(\psi; \mathbf{x}, t) \rightarrow \mathbf{f}_\varphi(\psi; t)$, i.e., independent of $\mathbf{x}$. The scalar mixing at the smallest scales is directly linked to the scalar variance. A scalar field that is well *micromixed* on the molecular level is represented by a pdf with zero scalar variance (Fox, 2003). These processes are referred to as *macromixing* and *micromixing*, respectively.

2.4.1 Ideal reactor models

An ideal reactor model makes *a priori* assumptions of the macromixing and micromixing conditions.

A perfectly stirred reactor (PSR) is a reactor that is both well macromixed and well micromixed (Fox, 2003). The PSR is based on a chamber with continuous inflow and outflow. In a Lagrangian sense, the entering fluid elements are mixed infinitely fast with the elements occupying the chamber. The fluid elements exiting the reactor are picked randomly from the occupying elements. For an Eulerian description (Turns, 2000), the reactor is described by a set of ordinary differential equations (ODEs). In any case, to determine the steady state of the reactor, an average residence or macromixing time must be provided.

A plug flow reactor (PFR) is a one-dimensional reactor with no interaction between elements along the reactor axis. Locally, the model assumes

that the individual elements are perfectly mixed. Hence, the reactor is not macromixed, but perfectly micromixed. The Lagrangian approach to the PFR consists of fluid elements with no interaction and the same residence time in the reactor. Following an Eulerian description, the one-dimensional transport equations for mass, momentum and energy can be written as a system of ODEs, and readily solved (Turns, 2000).

2.4.2 Zone models

A zone model splits the reactor up in N zones, while interaction between the zones is given empirically by predefined transport rates (Fox, 2003). The local micromixing, i.e., internal mixing within zones, cannot be captured by the zone models. Mathematically, the model can be expressed as a system of balance equations for each of the N zones

$$\frac{d\varphi^{(i)}}{dt} = \sum_{j=0}^{N+1} \left(g_{ji}\varphi^{(j)} - g_{ij}\varphi^{(i)} \right) + \omega_{\varphi}^{(i)} \quad i = 1, ..., N, \tag{2.19}$$

where g_{ij} is the transport rate from zone i to j. The inlet and the outlet zones are indexed by $j = 0$ and $j = N + 1$, respectively. Zone models apply an Eulerian description of fluid elements. The similarities with Computational Fluid Dynamics (CFD) models are apparent, though some obvious differences exist. The zones, contrary to grid cells in CFD, are for instance optimized for scalar transport and reaction regardless of the velocity and turbulence field. Arbitrary combinations of ideal reactors (PSRs and PFRs) with predefined transport rates are often used as simple models of combustion systems (Turns, 2000).

2.4.3 Moment methods

Moment methods solve the equations for the first statistical moments. When Reynolds decomposition and averaging is applied to the transport equation for a passive reacting scalar (2.5), we get

$$\frac{\partial \overline{\varphi}}{\partial t} + \frac{\partial}{\partial x_j}\left(\overline{u}_j \overline{\varphi}\right) = \frac{\partial}{\partial x_j}\left(D_{\mathrm{M}} \frac{\partial \overline{\varphi}}{\partial x_j} - \overline{u_j' \varphi'} \right) + \overline{\omega}_{\varphi}, \tag{2.20}$$

where the turbulence transport and the reaction terms appear unclosed. The former is usually modeled by a gradient diffusion approach. When Eq. (2.20) is solved along with the Reynolds-averaged mass and momentum equations, the computations are referred to as RANS (Pope, 2000).

In large eddy simulations (LES) the small scale fluctuations are filtered by solving the filtered transport equations. The filtered scalar transport equation reads

$$\frac{\partial \widehat{\varphi}}{\partial t} + \frac{\partial}{\partial x_j}\left(\widehat{u}_j \widehat{\varphi}\right) = \frac{\partial}{\partial x_j}\left(D_{\mathrm{M}} \frac{\partial \widehat{\varphi}}{\partial x_j} - \tau^r_{\varphi j}\right) + \widehat{\omega}_\varphi, \tag{2.21}$$

where $\tau^r_{\varphi j}$ is the sub grid scale (SGS) unresolved scalar flux. This term is commonly represented by a gradient model. Even though the large scale turbulence is better resolved in LES than in RANS, all SGS scalar fluctuation information is lost during the filtering operation (Fox, 2003). The reactions in turbulent combustion usually take place at the SGS level. Thus, the challenge of closing the microscale mixing and reaction remains a challenge for LES as well as for RANS.

A closure of the reaction term is generally given by

$$\overline{\omega}_\varphi = \int ... \int \omega(\psi, ..., ...) f(\psi, ..., ...) d...d\psi. \tag{2.22}$$

With the probability density function f known, the mean source term is given[4]. Presumed pdf methods assume the shape of the pdf *a priori*. The pdf is usually parameterized by the first and second moments. As pointed out in Sec. 2.3.2, the scalar dissipation rate is an important parameter in the closure of the second moment equation. The simplest presumed pdf methods assume infinitely fast chemistry, hence ω and f are functions of a single parameter (Warnatz *et al.*, 2001). *Flamelet* models for non-premixed combustion also prescribe the pdf in (2.22), but ω and f are functions of the mean mixture fraction and scalar dissipation rate (2.17), thus, taking finite-rate chemistry effects into account (Veynante and Vervisch, 2002).

The eddy dissipation concept (EDC) by Magnussen (1976), see also Ertesvåg and Magnussen (2000), or simpler eddy breakup type of models (Veynante and Vervisch, 2002) are other approaches to the closure of the mean reaction term. They are based on the assumption that the chemical reactions occur in regions where the turbulence dissipation takes place. Thus the mean reaction rate is ultimately governed by the scalar dissipation rate.[5] The original versions of these models employ fast chemistry, which essentially means that the species in the mixed regions react immediately. A more recent version of EDC (Gran, 1994) avoids this *mixed-is-burned*

[4]The term $\omega(\psi, ..., ...)$ is generally given by the chemical mechanism applied, and accurate representation of this term is usually more a cost than a modeling issue.

[5]In EDC, the limiting species in the reactions are also an important parameter.

assumption by considering the mixed regions to be PSRs and including detailed chemistry.

Conditional moment closure (CMC) is yet another type of moment closure (see Klimenko and Bilger (1999) for a review). It has been experimentally observed that the mean scalar (species mass fraction) conditioned on the mixture fraction has relatively small fluctuations around the mean (Fox, 2003). This is utilized to derive equations for mean scalars conditioned on mixture fraction. A certain resolution is required in mixture fraction space[6] in order to provide sufficient precision (Veynante and Vervisch, 2002). Closures for the convective and the micromixing terms and the conditional scalar dissipation rate are necessary as input to the model. The mixture fraction pdf must generally be presumed.

The scalar dissipation rate, which needs two-point pdfs for accurate description, is a central part in the closures for the reaction term in most modeling approaches. Usually, the scalar dissipation rate is modeled to be proportional to the turbulence dissipation rate. Many of the models for the mean chemical source term can essentially be considered as mixing models. In the next section we will see that the scalar dissipation rate is crucial also to the modeling of the scalar micromixing.

2.4.4 Pdf transport methods

Pdf transport models combine the exact closure of the chemical source term with a closure for the turbulence field (Pope, 1985). While simpler models apply Eqs. (2.15) and (2.16) and assume the shape of the pdf *a priori*, this approach solves the pdf itself. Statistics that are computed with the moment methods can be recovered once the pdf and the functional dependences of ψ are known.

For simplicity we consider the one-point scalar pdf transport equation which can be deduced from the scalar transport equation. Following Pope (2000) the equation reads

$$\begin{aligned}\frac{\partial \mathbf{f}_\varphi}{\partial t}+\frac{\partial}{\partial x_j}\left[\mathbf{f}_\varphi \overline{u}_j\right]+\frac{\partial}{\partial \psi}\left[\mathbf{f}_\varphi \omega(\psi)\right]=\\ \frac{\partial}{\partial x_j}\left[\mathbf{f}_\varphi\ \overline{(u_j|\psi)}\right]+\frac{\partial}{\partial \psi}\left[\mathbf{f}_\varphi \overline{\left(D_{\mathrm{M}}\frac{\partial \varphi}{\partial x_i}\frac{\partial \varphi}{\partial x_i}|\psi\right)}\right].\end{aligned} \tag{2.23}$$

The terms on the left hand side of the equation appear in closed form. Note that this also implies the reaction source term. However, the right hand side

[6] One equation set of conditional means is needed per node in mixture fraction space.

terms need closure. The first term, which is the evolution of the pdf due to the conditional velocity fluctuations, is often modeled by a gradient diffusion model. The gradient diffusion assumption can be avoided by introducing an equation for the joint velocity-scalar pdf (2.13). The second term is essentially the scalar dissipation conditioned on the scalar itself. This term represents the micromixing.

2.4.5 Micromixing models

Several micromixing models have been developed to close the last term in Eq. (2.23). These comprise both deterministic and stochastic models. An overview of the most commonly used is given below.

Subramaniam and Pope (1998) list a number of performance criteria for micromixing models, which essentially are summarized in the following list.

(1) Mean values should be preserved and the modeled mixing should result in decay of all variances.

(2) Scalar values should not travel out of their bounds in composition space, i.e., boundedness.

(3) A set of passive scalars should evolve independently.

(4) The scalar pdf should relax to a Gaussian in homogeneous turbulence.

(5) Fluid elements that are separated in composition space should not mix, i.e., localness.

(6) Differential diffusion effects should be taken into account.

(7) The mixing should be dependent on turbulence length scales.

Consider a reactor with a number of stochastic fluid elements which interact by some mixing process. This is commonly referred to as a partially stirred reactor (PaSR) (see e.g. Correa (1993)). The Curl's model, for instance described in Subramaniam and Pope (1998), is a stochastic mixing model that mixes pairs of fluid elements by first randomly selecting the elements to be mixed and secondly equalizing the content in the elements by linear combination. The events are sampled by a rate given as the inverse ratio of the mixing time, τ_m. The mixing time is defined by the ratio of the scalar variance to the scalar dissipation rate (Fox, 2003), but is often modeled to be proportional to the turbulence time scale as follows

$$\tau_m \equiv \frac{\overline{\varphi'^2}}{\varepsilon_\varphi} \sim k/\varepsilon. \tag{2.24}$$

The interaction by exchange with the mean model (IEM) by Dopazo (1975) is another mixing model for the PaSRs, where the fluid elements mix by relaxing toward the mean. A given set of fluid elements $\varphi^{(n)}$ evolves by

$$\frac{d\varphi^{(n)}}{dt} \sim -\frac{1}{\tau_m}(\varphi^{(n)} - \overline{\varphi}), \tag{2.25}$$

where $\overline{\varphi}$ is the mean over all fluid elements. Even though the IEM model in the PaSR context has some random components, it is considered deterministic due to the nature of Eq. (2.25).

The IEM and the Curl's mixing model satisfy the criteria no. (1) (2), and (3) above. In homogeneous turbulence, the IEM leaves the shape of the pdf unchanged, and the Curl's model approaches a non-Gaussian pdf (Fox, 2003). Neither of the models take localness (5) into consideration; however, the effect with the Curl's model where fluid elements are mixed instantaneously is more severe. Differential diffusion effects for IEM is treated in Chen and Chang (1998). The dependence of length scales (7) is not met by the models.

The Euclidean minimum spanning tree (EMST) mixing model by Subramaniam and Pope (1998) takes localness into account by only allowing mixing between fluid elements that are local in composition space. However, the model does not comply with the criterion (7).

In general, the IEM, the Curl's model and the EMST have shortcomings in their description of scalar mixing. In addition to the criteria listed above that are not met, none of the models distinguish between the diffusive molecular mixing and the advective turbulent stirring, which are completely different physical phenomena. A mixing time scale must be provided to all models, and the time scale is a function of the scalar dissipation rate.

2.4.6 LEM in relation to the mixing models

The Linear Eddy Model (LEM) is not a mixing model for pdf transport models per se, but rather an advection model where the modeling of molecular mixing and chemical reactions is rendered unnecessary due to the resolution of the small scales in 1D. By its construction, LEM meets all the criteria stated in the previous section. Concerning localness, LEM is local in the 1D *physical* space, which is physically more appealing than relating localness to composition space. One of the most important additional features is that LEM takes into account the effect of turbulence mixing length scales, and that molecular mixing and turbulent stirring are treated explicitly as distinct processes. Single- and multipoint moments of any order,

probability density functions (joint scalar) and conditional statistics can be extracted from LEM simulations. However, unless LEM is replaced by ODT (see Sec. 1.1 for a brief description), the scalar dissipation rate is needed as input also to the standalone LEM indirectly through the turbulence viscosity. LEM represents the microscale and *mesoscale*[7] mixing. Description of macroscale structures needs special adaptation or coupling to flow solvers.

2.5 Phenomenology

This section reviews a few of the classical phenomenological analyses of turbulence and turbulent mixing relevant to the numerical tests given in later sections and the derivation of LEM.

2.5.1 The spectrum of turbulence scales

The hypotheses of Kolmogorov are based on turbulent flows at high Reynolds numbers. Kolmogorov's hypotheses state that the smaller (fast) eddies in turbulence are isotropic and statistically independent of the larger (slow) eddies or the mean flow (Kolmogorov, 1941). The smaller eddies exists in equilibrium with the energy supplied from larger scales and the energy dissipated by the fluid viscosity. Hence, these scales are defined to be in the *universal equilibrium range*. The *inertial subrange* contains the eddies that are much smaller than the large turbulence structures, but still much larger than the diffusive scales. Thus, the inertial subrange turbulence is only dependent on the energy transfer from larger scales. Kolmogorov also assumes that the dissipation of turbulence energy occurs mainly at the smallest *dissipative* scales, denoted the *Kolmogorov scales*. From the hypotheses and dimensional analysis it follows that the Kolmogorov length scale is

$$\eta \equiv \left(\frac{\nu^3}{\varepsilon}\right)^{1/4}. \tag{2.26}$$

Similar expressions can be written for the time and velocity scales (see e.g. Tennekes and Lumley (1972)).

The energy is transferred from the largest to the smallest scales through a spectrum of scales. If we assume that all energy dissipation occurs in the dissipative range, the energy dissipation at the Kolmogorov scales equals the energy transfer from the largest scales. The energy transfer can be

[7]Here meaning the large, but not the largest scales.

estimated as

$$\varepsilon \sim \frac{u^{'2}}{\tau_t} \sim \frac{u^{'3}}{l_t}, \tag{2.27}$$

where the large eddy turnover time is $\tau_t = l_t/u^{'}$, and l_t is the integral scale.

If we combine the equations (2.27) and (2.26), an expression for the relation between the Kolmogorov and integral scales appears as

$$\frac{\eta}{l_t} \sim \left(\frac{u^{'} l_t}{\nu}\right)^{-3/4} = Re_t^{-3/4}, \tag{2.28}$$

where Re_t is the turbulence Reynolds number. By dimensional analysis (Tennekes and Lumley, 1972; Ertesvåg, 2000) we can show that the energy spectrum of turbulent eddies scales as

$$E(\kappa) \sim \varepsilon^{2/3}\kappa^{-5/3}, \tag{2.29}$$

where κ is the wavenumber which is proportional to a turbulence length scale l^{-1}. Equation (2.29) is commonly referred to as the *Kolmogorov's* 5/3 *law*. Similarly, we can estimate the scaling of the turbulence viscosity to

$$\nu_t(l) \sim \varepsilon^{1/3} l^{4/3}. \tag{2.30}$$

The latter is a central assumption in the derivation of the eddy distribution in LEM (Kerstein, 1991b).

When the Reynolds or Peclet numbers are large, the scalar structures, like the turbulence eddies, are distributed on a spectrum of scales. The stretching and folding of the scalar field occur at the large scales, while the enhanced gradients are smoothed out by the molecular diffusion at the small Kolmogorov or *Batchelor*[8] length scales (Fox, 2003). In this picture, the dissipation rate of scalar variance is independent of molecular diffusion and inversely proportional to the eddy turnover time; $\varepsilon_\varphi \sim \overline{\varphi^{'2}}/\tau_t$. Years of investigations have revealed that the phenomenon of scalar mixing poses great challenges and that this simplified picture is insufficient. The scalar, normally introduced on a single length scale, is subject to turbulent stirring that acts over a wide range of length scales. Further details on this subject will not be elaborated here. Good reviews are provided by Shraiman and Siggia (2000); Warhaft (2000, 2002) among several. This work focuses on the gross characteristics of scalar mixing. The two next sections present classical scalar mixing situations, which have been studied in this work and are reported in the Chapters 6 and 8.

[8]The Batchelor scale η_φ is related to the Kolmogorov scale by the Schmidt number (Tennekes and Lumley, 1972).

2.5.2 Scalar dispersion in isotropic turbulence

Stationary isotropic turbulence is invariant to translation, rotation or reflection of the coordinate system (Kolmogorov, 1941). The canonical flow has been thoroughly investigated since the early days of turbulence research.

Dispersion of scalars in isotropic turbulence undergoes basically three regimes of spreading as a function of distance from the source. The analytical description of this phenomenon was first presented in Taylor (1922) and later reviewed in Taylor (1935), Tennekes and Lumley (1972), and Pope (2000), among several. The first and last regimes are governed by diffusive growth, while in the second this growth is scaling by the size of characteristic eddies. In the *molecular diffusive* regime, which is on a time scale of the order of Kolmogorov time, the turbulence has no time to act on the scalar, and the spreading is governed by molecular diffusion only. In this regime the spreading of the mean scalar field is given by

$$\sigma \sim \sqrt{2D_{\mathrm{M}}t}, \tag{2.31}$$

where σ indicates the width of the scalar plume or the standard deviation if the scalar follows a Gaussian shaped curve.

In the *turbulent convective* regime, the fluid elements are correlated and the spreading of the mean scalar field scales linearly with t by

$$\sigma \sim u^{'}t. \tag{2.32}$$

In the *turbulent diffusive* regime, the time from the scalar release is much larger than the eddy turnover time τ_t and the fluid elements are completely uncorrelated. This gives that the mean scalar field spreads with the square root of the time by

$$\sigma \sim \sqrt{2u^{'2}\tau_t t} \sim \sqrt{2D_{\mathrm{T}}t}. \tag{2.33}$$

Details in the derivations are outlined in Pope (2000). This tri-partition of the growth has been verified in experiments by for instance Warhaft (1984). The mean square displacement of a fluid element subject to random motion follows the scaling (2.33), given that the diffusive time is large compared to the time it takes to travel the distance of one typical displacement (Hinze, 1975).

The simplest solution to the unsteady diffusion equation (Eq. (2.5) without the convective or the source term) is a Gaussian function. Experiments have verified that the mean scalar distribution of point sources in isotropic or homogeneous turbulence is nearly Gaussian even in the regimes close to

the source (Tennekes and Lumley, 1972). It can be shown that the distribution of fluid elements subject to random motion also follows Gaussian behavior (Hinze, 1975).

2.5.3 Passive scalar mixing in turbulent jets

Experiments show that axisymmetric turbulent jets spread linearly with axial distance from the origin (Tennekes and Lumley, 1972). In a turbulent round jet, the velocity fluctuations also decay with x^{-1} (Pope, 2000), so the ratio of velocity fluctuations to the mean velocity approaches a constant value. There are experimental evidences that the mean scalar, sufficiently far from the scalar source, decays roughly in the same way as the velocity (see for instance Villermaux and Innocenti (1999); Panchapakesan and Lumley (1993b)). However, the lateral profiles for the mean scalar is normally wider than the mean velocity. In an axisymmetric round air jet, the turbulence viscosity to the turbulence diffusivity, denoted the turbulence Schmidt number, is approximately 0.7. This result is supported by a number of experiments (see e.g. Panchapakesan and Lumley (1993b) and references therein).

The profiles of the scalar variance are reported to be comparable to those of the velocity fluctuations. However, the spreading of the scalar variance is somewhat wider, and the off-axis peak in the lateral profiles is more clear (Panchapakesan and Lumley, 1993a). In the previous citation, the eddy turnover time is measured and estimated to be 1.5 times larger than the mixing time scale (2.24), which implies that the scalar fluctuations decay somewhat faster than the turbulence itself.

Chapter 3

The governing models

The concept of Reynolds-averaged Navier-Stokes (RANS) modeling was introduced in Sec. 2.4.3. Here, we review the model equations that are applied in the present work, including the model equations related to the linear eddy model (LEM), and a conceptual scalar transport equation for the three-array structure of LEM domains.

3.1 RANS equations

Density fluctuations arise in reacting flows with non-isothermal reactions. If regular Reynolds averaging is applied to the transport equations, correlation terms between density and other properties cause undesirable modeling and computational difficulties (Poinsot and Veynante, 2001). By introducing density-weighting or Favre-averaging (Warnatz *et al.*, 2001) we avoid these problems. The Favre-decomposition of a scalar φ is given by

$$\varphi = \widetilde{\varphi} + \varphi'', \tag{3.1}$$

where the Favre-average is

$$\widetilde{\varphi} \equiv \frac{\overline{\rho\varphi}}{\overline{\rho}}, \tag{3.2}$$

and φ'' is the fluctuation of φ about the Favre-average. The Favre-average is interpreted as a time average for steady state solutions, or an ensemble average for time varying RANS computations (Ferziger and Peric, 2002).

3.1.1 Conservation of mass

Introducing the Favre-decomposition in the mass conservation equation (2.1), we get after averaging

$$\frac{\partial \overline{\rho}}{\partial t} + \frac{\partial}{\partial x_j}\left(\overline{\rho}\widetilde{u}_j\right) = 0. \tag{3.3}$$

No additional modeling is required for this equation.

3.1.2 Conservation of momentum

Neglecting body forces in Eq. (2.3) and introducing the Favre-decomposition as above, we get after averaging

$$\begin{aligned}\frac{\partial}{\partial t}(\overline{\rho}\widetilde{u}_i)+\frac{\partial}{\partial x_j}\left(\overline{\rho}\widetilde{u}_i\widetilde{u}_j\right) = -\frac{\partial \overline{p}}{\partial x_j}+ \\ \frac{\partial}{\partial x_j}\left(\overline{\rho}\nu\left(\frac{\partial \widetilde{u}_i}{\partial x_j}+\frac{\partial \widetilde{u}_j}{\partial x_i}-\frac{2}{3}\frac{\partial \widetilde{u}_k}{\partial x_k}\delta_{ij}\right)-\overline{\rho u_i'' u_j''}\right),\end{aligned} \tag{3.4}$$

where the last term on the right hand side represents the *turbulence stresses*. The eddy viscosity/diffusivity assumption, put forward by Boussinesq in 1877 (see e.g. White (1991)), states that the turbulence flux can be modeled as an additional *eddy* viscosity ν_t. Hence, the unclosed term is expressed in terms of the known mean quantities, and the model equation becomes

$$\begin{aligned}\frac{\partial}{\partial t}(\overline{\rho}\widetilde{u}_i)+\frac{\partial}{\partial x_j}\left(\overline{\rho}\widetilde{u}_i\widetilde{u}_j\right) = -\frac{\partial \overline{p}}{\partial x_j}+ \\ \frac{\partial}{\partial x_j}\left(\overline{\rho}(\nu+\nu_t)\left(\frac{\partial \widetilde{u}_i}{\partial x_j}+\frac{\partial \widetilde{u}_j}{\partial x_i}-\frac{2}{3}\frac{\partial \widetilde{u}_k}{\partial x_k}\delta_{ij}\right)-\frac{2}{3}\overline{\rho}k\delta_{ij}\right),\end{aligned} \tag{3.5}$$

where k here is the Favre-averaged turbulence energy. The turbulence viscosity is modeled as a product of a characteristic turbulent length and velocity scale. By introducing the Favre-averaged turbulence dissipation ε the turbulence viscosity by dimensional consideration reads

$$\nu_t = c_\mu \frac{k^2}{\varepsilon}. \tag{3.6}$$

The model constant c_μ is empirically estimated to 0.09 by considering turbulence stresses in the near wall region (Ertesvåg, 1991). The turbulence viscosity can be determined by solving an equation for the turbulence energy and the turbulence dissipation rate, i.e., the k-ε-model. More accurate approaches that omit the Boussinesq assumption can also by applied[1], but are not considered in the present work.

[1] Higher moment closures such as e.g. Reynolds Stress Models (RSM), see for instance Launder (1989)

3.1.3 Turbulence scalar transport

The Favre-averaged scalar transport equation (2.4) is given by

$$\begin{aligned}\frac{\partial}{\partial t}\left(\overline{\rho}\widetilde{\varphi}\right)+\frac{\partial}{\partial x_j}\left(\overline{\rho}\widetilde{u_j}\widetilde{\varphi}\right)=\\ \frac{\partial}{\partial x_j}\left[\overline{\rho}D_{\mathrm{M}}\frac{\partial\widetilde{\varphi}}{\partial x_j}-\overline{\rho u_j''\varphi''}\right]+\overline{\rho\omega_\varphi}+\frac{\partial}{\partial x_j}\left[D_{\mathrm{M}}\overline{\rho'\frac{\partial\varphi''}{\partial x_j}}\right],\end{aligned} \tag{3.7}$$

where the latter term usually is neglected in modeling. Since we in this work only consider transport of conserved scalars, the reaction term is omitted in the following. The *turbulence flux* $-\overline{\rho u_j''\varphi''}$ in the above equation is unclosed. Following Boussinesq, the turbulence flux is modeled as an additional diffusivity D_{T} which gives

$$\frac{\partial}{\partial t}(\overline{\rho}\widetilde{\varphi})+\frac{\partial}{\partial x_j}(\overline{\rho}\widetilde{u}_j\widetilde{\varphi})=\frac{\partial}{\partial x_j}\left(\overline{\rho}(D_{\mathrm{M}}+D_{\mathrm{T}})\frac{\partial\widetilde{\varphi}}{\partial x_j}\right). \tag{3.8}$$

By the Boussinesq assumption, the molecular and turbulence diffusivity contributes to the same gradient transport. Hence, the molecular contribution, even though crucial in the real scalar mixing process, becomes insignificant since $D_{\mathrm{T}}\gg D_{\mathrm{M}}$. If we assume equal molecular diffusion coefficients for all scalars, it follows that

$$D_{\mathrm{M}}+D_{\mathrm{T}}=\frac{\nu+\nu_t}{\sigma_t}, \tag{3.9}$$

where σ_t is the turbulence Schmidt-number. For the moment-method in this work, we assume that the molecular and turbulence Schmidt-numbers are equal ($Sc=\sigma_t$).

3.1.4 Model equation for the scalar variance

A scalar variance ($\overline{\varphi'^2}$) equation can be derived by applying the Favre-decomposition to the scalar transport equation (2.4), multiplying the equation with the scalar fluctuation itself and taking the average. Hence, the transport equation for the Favre-averaged scalar variance is given as (Fox, 2003)

$$\begin{aligned}\frac{\partial}{\partial t}(\overline{\rho}\widetilde{\varphi''^2})+\frac{\partial}{\partial x_j}(\overline{\rho}\widetilde{u}_j\widetilde{\varphi''^2})=\frac{\partial}{\partial x_j}\left(\frac{\overline{\rho}(\nu+\nu_t)}{\sigma_t}\frac{\partial\widetilde{\varphi''^2}}{\partial x_j}\right)+\\ 2\frac{\overline{\rho}(\nu+\nu_t)}{\sigma_t}\frac{\partial\widetilde{\varphi}}{\partial x_j}\frac{\partial\widetilde{\varphi}}{\partial x_j}-2\frac{\overline{\rho}\nu}{\sigma_t}\overline{\frac{\partial\varphi''}{\partial x_j}\frac{\partial\varphi''}{\partial x_j}}.\end{aligned} \tag{3.10}$$

The last two terms on the right hand side are the rate of production and dissipation of the scalar variance[2], respectively. The former term is closed by applying a gradient transport assumption, while the latter is modeled by considering the scalar variance to decay with the mixing time scale. The mixing time scale is assumed to be proportional to the turbulence time scale. This gives

$$2\frac{\overline{\rho}\nu}{Sc}\overline{\frac{\partial\varphi''}{\partial x_j}\frac{\partial\varphi''}{\partial x_j}} = \frac{\overline{\rho}\widetilde{\varphi''^2}}{\tau_m} = C_\varphi\overline{\rho}\frac{\varepsilon}{k}\widetilde{\varphi''^2}, \tag{3.11}$$

where C_φ is a case dependent constant commonly adopted to be $C_\varphi = 2$, but generally varies for different flow configurations (Pope, 2000). Applying the expression for the rate of turbulence energy dissipation

$$\varepsilon = c_\mu^{3/4}\frac{k^{3/2}}{l_t}, \tag{3.12}$$

which is derived in (Ertesvåg, 2000), and combining it with the expression for the turbulence viscosity, it follows that the dissipation rate term in Eq. (3.10) is proportional to

$$\frac{\varepsilon}{k} \sim \nu_t l_t^{-2}. \tag{3.13}$$

Hence, if the turbulence viscosity is a given constant, the scalar dissipation rate is in inverse ratio to the square of the integral scale according to the model above.

3.2 The Linear Eddy Model

The Linear Eddy Model developed by Kerstein (1991b) is, unlike the Navier-Stokes equations, based on a phenomenological description of turbulent mixing. The modeled turbulent convective stirring constitutes a cascade of rearrangement events that continuously compress scalar gradients and increase the number of iso-scalar interfaces along a line of sight. The turbulent stirring enhances molecular mixing, which is a prerequisite for complete mixing and chemical reactions in reacting flows.

In contrast to the traditional models for mixing and reaction in turbulent flows, briefly presented in the previous chapter, LEM has the appealing feature that no modeling is needed for the molecular mixing and chemical reactions due to the fine resolution. This is rendered affordable due to

[2]The scalar dissipation rate

the reduced description of turbulent stirring and molecular mixing in one dimension. Another appealing aspect of LEM is that the turbulent convective stirring and diffusive molecular mixing are treated as distinct processes.

LEM provides multi-point statistics along the 1D domain, which allows for extended analyses of the scalar field. The following sections present the most commonly used standalone version of LEM. An outline of the previous works is given in Sec. 1.2, and the discrete implementation is outlined in Sec. 4.3. Since complete descriptions of LEM are given elsewhere (Kerstein, 1991b, 1992b), only a brief introduction is given here. Further details of the numerical implementation of LEM is given in Sec. 4.3.

3.2.1 Model description

The molecular mixing and chemical reactions are resolved on a one-dimensional domain. This implies that the numerical grid on which the reaction-diffusion equation is parameterized should have a resolution on the order of the Kolmogorov or Batchelor scales. The one-dimensional constant density scalar diffusion equation is written

$$\frac{\partial \varphi}{\partial t} = \frac{\partial}{\partial x}\left[D_{\mathrm{M}} \frac{\partial \varphi}{\partial x}\right]. \tag{3.14}$$

LEM is not limited to conserved scalars, and the equation above may also contain reaction source terms. For a detailed chemical representation, Eq. (3.14) can represent mass fraction and energy transport (Sankaran and Menon, 2000). However, since only conserved scalars are considered in the present work, the reaction term is omitted.

The turbulent convective stirring is treated separately by the randomly implemented rearrangement or mapping events. These events are determined by three elements; the rate of mapping events, the distribution of mapping sizes, and the spatial distribution of event locations. In addition, a mapping scheme for the rearrangement events must be chosen.

Early versions of LEM use the block inversion scheme, which represents the turbulent stirring of the scalar field by simply mirroring the scalar profile about the mapping center (Kerstein, 1988, 1989, 1990). One major artifact of this mapping scheme is that it introduces discontinuities at the ends of the event. In Kerstein (1989) the block inversion events are sampled from a distribution.

The triplet map, first introduced by in Kerstein (1991b), creates three copies of the scalar field over the span of its size, compresses these copies by a factor of three, and then inverts the center copy. This operation emulates

qualitatively the compressive strain and the increase in scalar interface crossings caused by the turbulence. Figure 3.1 illustrates the effect of a triplet map on a linear scalar gradient.

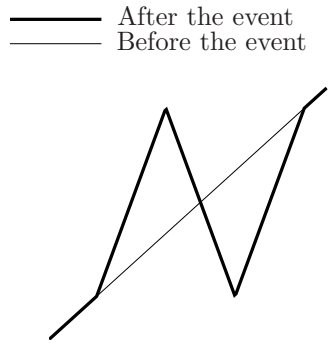

Figure 3.1: The figure illustrates a continuous linear scalar gradient before and after a triplet map has been applied to it.

Following the steps generally described in Appendix A, an expression for the turbulence diffusivity is derived as

$$D_{\mathrm{T}} = \frac{2}{27}\lambda \int_{\eta}^{L} l'^{3} f(l') dl', \tag{3.15}$$

where λ is the *event frequency parameter*, which is the frequency of rearrangement events per unit domain length, and L is the size of the largest implemented mapping event, also denoted the *model integral scale*. The size of the rearrangement events is determined using the Kolmogorov scaling for inertial range turbulence. Hence, the turbulence diffusivity induced by eddies on the order of l scales as $D_{\mathrm{T}} \sim l^{4/3}$, following Eq. (2.30). It is important to note that the model is generally not restricted to the Kolmogorov scaling applied here, meaning that other scaling exponents than 4/3 might be applied. From the 4/3 scaling law and Eq. (3.15), the event size distribution is determined to

$$f(l) = \frac{5}{3L} \frac{1}{\left(L/L_{\mathrm{K}}\right)^{5/3} - 1} \left[\frac{l}{L}\right]^{-8/3}, \tag{3.16}$$

by normalization to one. Here, L_{K} is the size of the smallest implemented triplet map, corresponding to the physical Kolmogorov scale. The size of

the rearrangements is confined to the interval $L_K < l < L$ and is generally sampled from the expression above.

By combining Eq. (3.15) and (3.16), the expression for the event frequency parameter follows as

$$\lambda = \frac{54}{5}\frac{D_T}{L^3}\frac{\left[(L/L_K)^{5/3} - 1\right]}{\left[1 - (L_K/L)^{4/3}\right]}. \tag{3.17}$$

The distribution of spatial event locations is generally uniform, but different distributions can be employed to reflect various flow configurations. In this work (Sec. 4.3.2), the spatial event distribution mimics the spatial variation in turbulence diffusivity.

3.2.2 The LEM model constants

Since the model integral scale L, which is used to determine the distribution (3.16) and rate (3.17) of mapping events, is the largest possible eddy and not defined to be equal to the physical integral scale l_t, it is scaled by a factor of order unity. For a line source experiment by Warhaft (1984), this factor was set to $L/l_t = 5.6$ to match second order moments with data (Kerstein, 1992b). Simulations of a reacting mixing layer, presented in the same paper, yielded a factor of 2.5.

The second empirical relation is a tuning of the molecular Schmidt number, which determines the viscous cut-off of the small scale eddies. The factor $Sc_S = 0.51Sc$, where Sc_S is the model Schmidt number, is based on numerous comparisons of measured and simulated spectral properties (see in general Kerstein (1991b)). Note that this only applies to the spectral properties, i.e., the viscous cut off, and does not affect the relation between molecular and turbulence transport by Eq. (3.9).

3.2.3 Input to LEM

In addition to the constants mentioned above and the scaling exponent of the inertial range, there are three necessary input parameters to LEM, namely the turbulence diffusivity D_T, the molecular diffusivity D_M, and the model turbulence integral scale L. The model Kolmogorov length scale is estimated from the model analog to Eq. (2.28), given as

$$L_K = Re_S^{-3/4} L, \tag{3.18}$$

where Re_S is the model Reynolds number given by $Re_S = Pe/Sc_S$, and the Peclet number is $Pe \equiv D_T/D_M$.

3.3 Scalar evolution in the model framework

This section anticipates the presentation of the LEM3D implementation in Chapter 4 by presenting the transport equation for the three-array structure of LEM domains. In addition, the basis for the Lagrangian fluid cell transport is outlined.

3.3.1 Conceptual transport equation

The scalar transport equation for three-dimensional LEM evolution, which in principal represents the scalar transport equation (2.4), can conceptually be written as

$$\frac{\partial}{\partial t}(\varphi)_j + \mathcal{ADV} + \mathcal{EXP} + \mathcal{TM}_j = \frac{\partial}{\partial x_j}\left[D_{\mathrm{M}}\frac{\partial \varphi}{\partial x_j}\right], \tag{3.19}$$

where the index j indicates that the terms are implemented on 1D LEM domains in three directions. Note that conventional summation over the repeated index j is not implied for the right hand side term. The molecular diffusion part is solved directly in 1D along the individual LEM domains. The diffusion process is punctuated by stochastic triplet map events $\mathcal{TM}_j$ implemented on the same domain. The advection process $\mathcal{ADV}$ is governed by a velocity field, which is prescribed from flow solvers, measurements or analytical expressions. The advection is implemented deterministically by Lagrangian displacement of fluid cells. This process involves intersecting domains. The heat release $\mathcal{EXP}$ is determined by the condition in each LEM fluid cell, however, the dilatation involves intersecting domains. The stochastic stirring and mixing process is the precursor for chemical reactions and heat release. Hence, the heat release and dilatation exhibit random behavior.

3.3.2 Scalar advection by the Lagrangian approach

A fluid particle is by definition a point that moves with the fluid (Pope, 2000). Let $\boldsymbol{X}^0$ or X_i^0 be the position of a particle at a reference time t^0. At the time t the particle has moved to the position $\boldsymbol{X}^+(t, \boldsymbol{X}^0)$. The position $\boldsymbol{X}^+$ or X_i^+ is now defined by the reference position

$$X_i^+(t^0, \boldsymbol{X}^0) = X_i, \tag{3.20}$$

and the incremental change in position due to the flow velocity

$$\frac{\partial X_i^+(t, \boldsymbol{X}^0)}{\partial t} = u_i(\boldsymbol{X}^+, t), \tag{3.21}$$

where $u_i(\boldsymbol{X}^+, t)$ is the local velocity.

The Lagrangian field is indexed by the initial position of the particle and the elapsed time, and is defined in relation to its Eulerian counterpart as

$$\varphi^+(t, \boldsymbol{X}^0) \equiv \varphi(\boldsymbol{X}^+(t, \boldsymbol{X}^0), t). \tag{3.22}$$

Hence, φ is given if $\boldsymbol{X}^+(t, \boldsymbol{X}^0)$ is known. For this reason, only Eq. (3.21) needs to be time integrated in order to determine the scalar field.

It can be shown, by taking the partial time derivative of the relation (3.22) and applying the chain rule, that the partial time derivative of φ^+ is the material derivative of φ (Pope, 2000). This implies that the scalar value for a given particle φ^+ is unchanged during advection advancement.

Chapter 4

Implementation of LEM3D

4.1 Introduction

Turbulent stirring, molecular mixing and chemical reactions are treated as distinct processes in LEM. Molecular mixing and chemical reactions appear in closed form due to the resolution of Batchelor scales, and are implemented deterministically by solving the appropriate reaction-diffusion equations. The LEM3D has been developed guided by the principle of maintaining the distinctive feature of LEM. As a consequence, scalars are not mixed at the molecular level by any other process than molecular diffusion, which rules out Eulerian treatment of advection and dilatation.

This chapter presents the framework for a three-dimensional scalar mixing model with LEM as the building block. The model, which is denoted LEM3D for further reference, constitutes a three-array structure of LEM domains. The structure is similar to the ODTLES that is presented in Schmidt *et al.* (2008); Kerstein (2009), however with two major differences. LEM instead of ODT is used as the model building block, and advection and dilatation are based on Lagrangian fluid cell displacements instead of Eulerian finite differencing across fluid cell boundaries. The model is solely a scalar transport, mixing and reaction model. Hence, the velocity and turbulence diffusivity fields must be provided from elsewhere. In general, they can be provided from measurements or from any simulation tool giving the average velocity and turbulence field.

The presented framework and methods utilized for treating advection and dilatation represent one of several options for implementation. Alternative approaches are not considered in the present chapter. All LEM3D elements described were implemented in the Fortran programming language. Data visualization in Chapters 5 through 8 was set up using Tecplot (2009).

4.2 The three-array structure

The standalone LEM operates only in one dimension along a line of sight through the domain of interest. Here we assume that the one-dimensional standalone LEM domain occupies a volume. Thus, it is discretized by wafer-shaped control volumes with thickness Δx_{w} and square cross sectional area $\Delta y \times \Delta z$ as shown in the left part of Fig. 4.1.

The domain of interest is assumed to be a cuboid of dimensions X, Y and Z. A finite number of LEM domains in the x-direction are arranged in a stack so that they span the domain, as indicated in the right part of Fig. 4.1. The total number of LEM domains in the stack is $N_y \times N_z$ where $N_y = Y/\Delta y$ and $N_z = Z/\Delta z$, respectively.

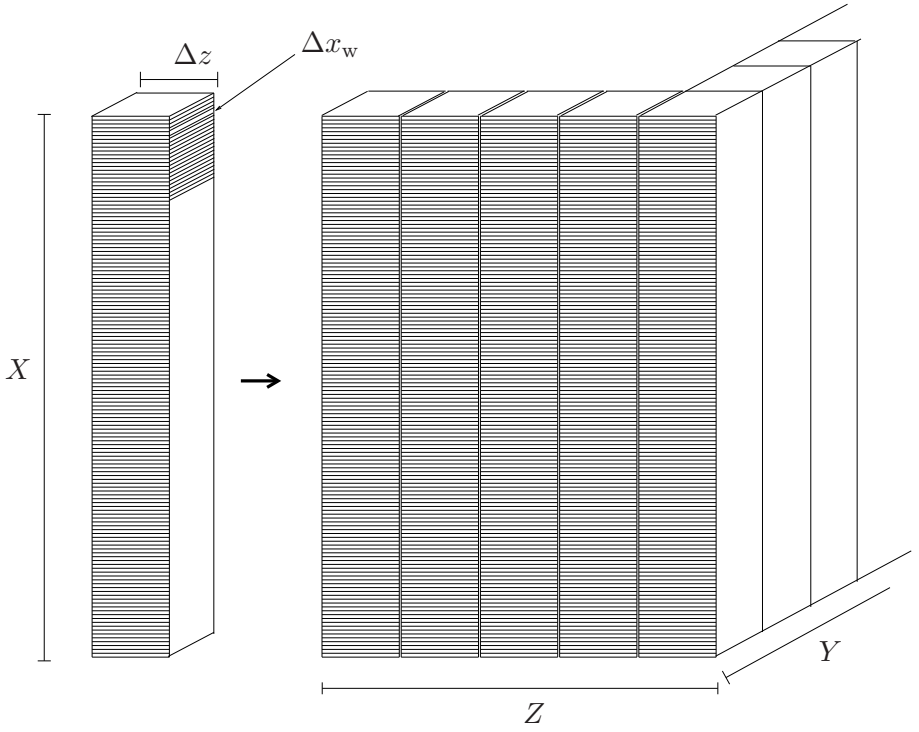

Figure 4.1: Left: A single stand-alone LEM domain discretized by wafers in the x-direction. Right: $N_y \times N_z$ such domains are arranged in a stack spanning the domain of interest.

Stacks that resolve the same domain of interest in the y and z-directions are constructed in similar manner with $\Delta z = \Delta y = \Delta x$, $N_x = X/\Delta x$, and N_y and N_z as given above. The supergrid, which is defined by the boundaries between orthogonally intersecting LEM domains, is a three di-

mensional regular Cartesian grid (see Fig. 4.2) and the cubical control volumes in this grid are denoted 3DCVs. A similar structure is described in Kerstein (2009). Further details, which are described here, were developed by Kerstein *et al.* (2005-2006).

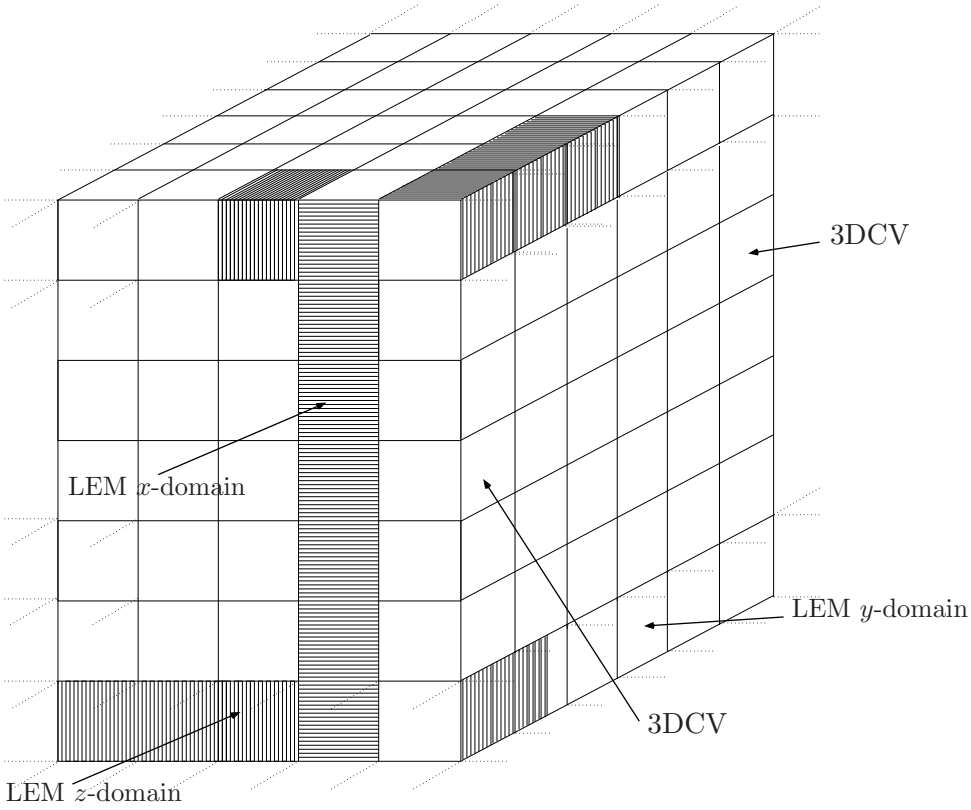

Figure 4.2: The domain of interest is resolved by three stacks of LEM domains that are resolved by wafers in the x, y and z-direction, respectively. The 3DCVs are the cubical control volumes in the supergrid that is defined by the intersecting boundaries between LEM domains.

Since the 3DCVs are cubical by construction, the side face lengths are in the following described by Δx only. Further, M denotes the number of wafers resolving the 3DCV in each direction. This is in the following referred to as the *1D-resolution*, which also is the same in the three directions. The thickness of the wafer is given by $\Delta x_{\mathrm{w}} = \Delta x/M$. This smallest model scale is typically on the order of the Kolmogorov or Batchelor scales. The subdivision of the domain in 3DCVs is denoted the *3D-resolution*. The 3DCV side lengths Δx should be large for computational efficiency, but

small enough to represent the mean flow scales with sufficient resolution.

The scalar processes of LEM3D generally take place on two levels. First, the molecular diffusion, chemical reactions and triplet map stirring are implemented on the individual LEM domains independently of the processes on the other domains. The mean flow advection, the thermal expansion and the auxiliary coupling on the other hand involve domains in all three directions. These processes are therefore treated on a 3DCV basis, meaning that the parts of the three intersecting LEM domains that span a 3DCV are considered simultaneously.

The three orthogonal stacks of LEM domains are three individual representations of the computational volume that are advanced concurrently. Hence, the superposition of stacks will constitute three times the amount of all extensive properties within the domain of interest. This implies that the overall transport rates must be multiplied with a factor 3 in order to accommodate the specific given rates. For example, since the 3DCV constitutes 3 times the mass, the maximum mean velocity used to prescribe the advection advancement in LEM3D is 3 times the physical mean velocity. This gives the correct specific flow rate (ρu). The molecular mixing is represented on each domain separately, so the molecular diffusivity is not altered by the factor 3. The turbulence diffusivity in Eq. (3.17) is also multiplied by the factor 3, however, we apply the non-altered D_{T} to estimate the Kolmogorov scale cut-off of the eddy size distribution.[1]

The three-array structure is particularly suited for parallel computing. With multi-component species diffusion and reaction, the processes on the individual LEM domains will by far be the most time consuming part of the model.

4.3 The LEM processes

This section describes the processes that take place on the individual LEM domains. Except for some minor differences and adjustments, this is equivalent to the standard LEM as it is presented in e.g. Kerstein (1991b).

4.3.1 The diffusion equation

This section concerns solving the transient non-reacting diffusion equation (3.14) on the 1D LEM domains. In this work, the molecular diffusion

[1] That is, we apply the original Peclet/Reynolds-number in the expression $L_{\mathrm{K}} = Re_S^{-3/4} L$.

equation is solely applied to passive non-reacting scalars. A brief presentation of the reacting approach is given in Sec. 4.3.3.

The properties of the wafers are defined at the wafer center. The transient term is approximated using the first order forward Euler (explicit) scheme. Second order numerical accuracy is ensured for the diffusion term by applying central schemes on the regular grid.[2] By integrating the diffusion equation (3.14) with the schemes as mentioned, we get the following set of algebraic equations

$$\varphi_i = \mathrm{CFL}\varphi_{i-1}^0 + \varphi_i^0\,(1 - 2\mathrm{CFL}) + \mathrm{CFL}\varphi_{i+1}^0, \tag{4.1}$$

where CFL is the Courant-Friedrichs-Lewy number given as

$$\mathrm{CFL} = \frac{D_\mathrm{M}\Delta t_\mathrm{w}}{(\Delta x_\mathrm{w})^2}, \tag{4.2}$$

and Δt_w is the molecular diffusive time step. The equation set (4.1) is solved directly with the requirement that CFL ≤ 0.5 for numerical stability.

Alternatively, if a first order forward Euler (implicit) scheme approximates the transient term, the equations becomes a tridiagonal linear equation system

$$-\mathrm{CFL}\varphi_{i-1} + \varphi_i\,(1 + 2\mathrm{CFL}) - \mathrm{CFL}\varphi_{i+1} = \varphi_i^0. \tag{4.3}$$

This equation system must be solved by direct or iterative methods. In this work, the Tridiagonal Matrix Algorithm (TDMA) direct method is used. The implicit scheme is unconditionally stable for any CFL-number, but the time accuracy is reduced by increasing time step. The explicit scheme was generally used for the simulations in Chapter 6 and 8. No significant difference was found between the two schemes for these cases.

4.3.2 Stirring by triplet map events

The turbulent stirring is implemented by randomly selected rearrangement events or *triplet maps*. As mentioned previously, there are three parameters that determine a triplet map on the LEM domain: The time when the event is occurring, the size of the mapping, and the location of the event on the domain.

When the turbulence diffusivity is uniform, the location is sampled from an even distribution. The turbulence diffusivity extracted from RANS or measurement data generally varies in space. This is represented in LEM3D

[2] Finite volume and finite difference methods are equivalent on the regular grid.

by associating a turbulence diffusivity D_T with each of the 3DCVs. The position of the triplet map is now sampled in two steps as follows. First, the 3DCV, in which the center of the triplet map should be located, is sampled from a cumulative probability distribution function that represents the distribution of D_T across the LEM domain. Secondly, the exact position of the triplet map center within the 3DCV is sampled with equal probability.

The triplet map operation first creates three copies of the scalar domain that it covers. Then it compresses the copies by a factor of 3 and finally inverts the middle copy. When the discrete triplet map is applied to a segment, which is a multiple of 3 wafers and labeled $[1, 2, , ..., 3k]$, the resulting sequence reads $[[1, 4, 7, ..., 3k-2]$, $[3k-1, 3k-4, 3k-7, ..., 2]$, $[3, 6, 9, ..., 3k]]$.[3] Since a triplet map of $k = 1$ wafers involves no rearrangements, the smallest possible triplet map is $k = 2$. In this work, the smallest possible triplet map was set to $k = 4$ in order to reduce the numerical inaccuracies related to the smallest triplet map. An example of a triplet map on the interval $[1, 18]$ applied to a discrete scalar field with a linear gradient is shown in Fig. 4.3.

The expressions for eddy size distribution and event frequency presented in Sec. 3.2.1 are derived assuming continuous triplet maps. However, the numerical implementation of triplet maps on the LEM domain will inevitably be discrete. Sannan *et al.* (2008) present a derivation of the discrete expressions for the event frequency (3.17) and the triplet map size distribution (3.16). From the derivation, the size distribution follows as

$$f(k') = \frac{k'^{-8/3}}{\sum_{k=k_\mathrm{min}}^{k_\mathrm{max}} k^{-8/3}}, \quad k_\mathrm{min} \leq k' \leq k_\mathrm{max}, \tag{4.4}$$

where $3k_\mathrm{min}\Delta x_\mathrm{w} = L^*_\mathrm{K}$ is the smallest[4] and $3k_\mathrm{max}\Delta x_\mathrm{w} = L$ is the largest triplet map size. The distribution of triplet map sizes (3.16) is constructed applying a common model integral scale for all LEM domains in LEM3D. The event frequency is further given by

$$\lambda = \frac{D_\mathrm{T}}{2(\Delta x_\mathrm{w})^3} \left[\sum_{k=k_\mathrm{min}}^{k_\mathrm{max}} k^{-8/3} \right] \left[\sum_{k=k_\mathrm{min}}^{k_\mathrm{max}} (k-1)k^{-2/3} \right]^{-1}. \tag{4.5}$$

If the turbulence diffusivity varies along the domain, Eq. (4.5) is estimated based on an average turbulence diffusivity for the LEM domain.

[3] The individual segment copies are separated by brackets.

[4] The star is introduced to indicate that the smallest triplet map might be chosen larger than the model Kolmogorov scale.

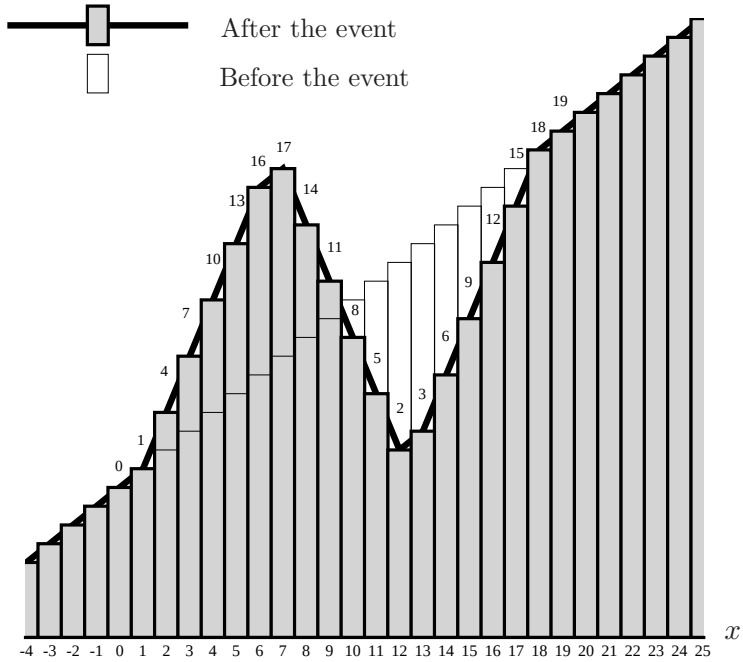

Figure 4.3: The figure illustrates a discrete scalar field with a linear gradient before (white bars) and after (grey bars) a triplet map of $6k$ has been applied to the interval $[1, 18]$

The triplet map events are assumed to be statistically independent, hence the time t to when the next single event occurs is sampled from the Poisson distribution

$$f_x(t) = R_x e^{-R_x t}, \tag{4.6}$$

where R_x is the mean rate of events on the x-oriented LEM domains given by $R_x = \lambda N_x$. Similar expressions apply to the y- and z-oriented domains.

To summarize, the triplet map is determined by sampling the time to the next event from the cumulative Eq. (4.6) and the size from the cumulative Eq. (4.4), and by determining the location from the two-step procedure described in the second paragraph of the present section.

4.3.3 Implementation of thermal expansion

The triplet map operation in its present form requires the wafers to be fixed and uniform in volume. This imposes a restriction on the implementation of the dilatation from thermal expansion. As reviewed in Sec. 1.2.2, one option is expansion of fluid wafers followed by regridding to a uniform grid before every triplet map event. Another approach is Eulerian treatment of the expansion, whereas a third alternative is only to allow expansion of wafers in discrete steps (Menon and Calhoon, 1996).

As mentioned previously, LEM3D endeavors to maintain the distinction between chemical reactions, molecular diffusion and turbulent mixing, which means that scalars should not mix at the molecular level by other processes than molecular diffusion. The option of expansion in discrete steps is chosen here since it preserves this distinction. A wafer is expanded, when necessary, by increasing the volume by an integer number of wafers and reducing the density accordingly, keeping the total mass in the system constant. This method introduces no spurious diffusion; however, it implies restricting the expansion to discrete steps.

The discrete dilatation

In the LEM3D framework, the shape and the volume of the wafers are constant. In addition, the wafer density is kept constant in between the discrete expansion events. At a given criterion, the volume of a wafer is extended by Φ multiples of its volume. This is performed by creating $\Phi + 1$ new copies of the wafer to be expanded, and replacing the original wafer by the $\Phi + 1$ copies as illustrated in Fig. 4.4. The resulting dilatation gives corresponding displacement of surrounding wafers as further explained in Sec. 4.5.2. The new wafers adopt the density $\rho = \rho_0/(\Phi + 1)$, where ρ_0 is the density from when the last expansion occurred. In this way, mass is conserved during the dilatation.

The expansion criterion

The criterion for when a wafer should be expanded may be based on the thermodynamic pressure. If we assume that the pressure can be estimated from the equation of state

$$p^+ = \rho_0 R_{\text{mix}} T, \tag{4.7}$$

where T is the temperature, R_{mix} is the gas constant for the mixture, a temperature change causes a corresponding pressure change. The superscript

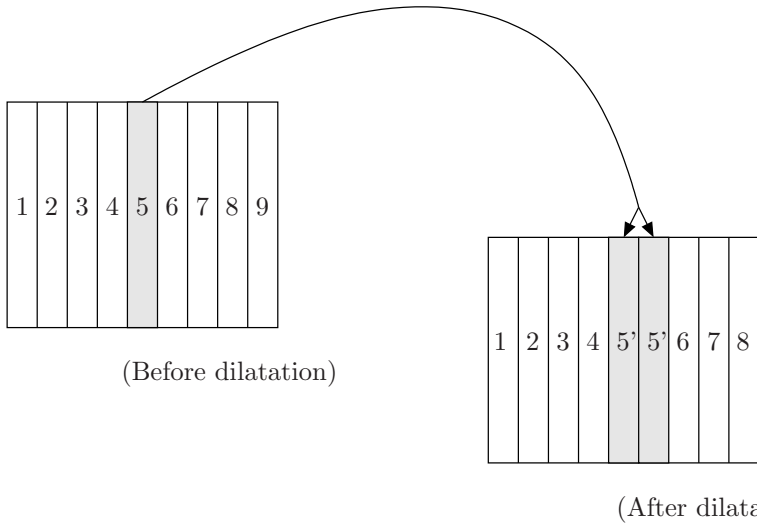

Figure 4.4: Example of a discrete expansion of wafer number 5 on an LEM domain. The dilatation results in a corresponding displacement of surrounding wafers as shown.

signifies that the pressure solely acts as an indicator for when the expansions should occur. When the pressure of a wafer exceeds the background pressure by a given factor, the wafer is expanded as explained above. The assumption of incompressibility holds, in the sense that there is no direct coupling between the LEM3D density and the pressure field in the flow solver (e.g. RANS). In other words, we neglect compressible effects, but account for thermal expansion and varying density, which commonly is denoted the zero-Mach number limit.

In the present work, the expansion events are not selected by the pressure criterion, but rather by random sampling from a distribution for test purposes. The chemical state is, however, intended to be determined by more realistic models in the future.

Representation of chemistry

Due to the resolution of Bathcelor scales, the wafers can be considered as homogeneous reactors, and the chemistry needs no additional modeling. Possibly the simplest approach is to assume adiabatic conditions, unity Lewis number, and infinitely fast chemistry. This is often denoted the Burke-Schumann approach, after the classical paper on diffusion flames by Burke and Schumann (1928). By these assumptions the chemical state is deter-

mined by the mixture fraction alone, which evolves in LEM3D.

This simple chemical implementation may be pursued in order to arrive at a reacting LEM3D with the least effort. An extension to a detailed description of chemistry with finite rate kinetics is essentially straightforward. This is basically achieved by replacing the conserved scalar diffusion equation (2.4) with a reaction-diffusion equation for mass fraction, and adding an equation for heat transport (e.g. enthalpy, total energy or temperature). In Echekki (2008), the reaction-diffusion equations are time integrated by operator splitting between diffusion and chemistry. Finite-rate chemistry involves solving a system of non-linear ordinary partial differential equations (Warnatz *et al.*, 2001). Thus, the cost in terms of computational time is significantly increased. Tabulated chemistry may be applied to reduce the computational cost (Sankaran and Menon, 2000). The method is well suited for massive parallel computing.

4.4 Coupling to a flow solver

Since LEM3D only represents the scalar transport, it relies on velocity and turbulence data provided from measurements or a separate flow solver. In this work, two approaches are applied. First, measurements of a turbulent jet in the self-similar region are used as velocity and turbulence input data. Further details are given in Sec. 5.2.2 and 8.3.1. Secondly, the turbulence and velocity data are given from solving the Favre-averaged Navier-Stokes equations for variable density. The assumption of incompressible flow is adopted, i.e., the density and pressure fields are decoupled. An in-house general-purpose CFD code is used (Melaaen, 1990; Gran, 1994). The code applies a semi-implicit algorithm for computing the velocity and pressure fields (Versteeg and Malalasekera, 1995) and comprises a wide range of closures for turbulence and chemistry. However, since the computations are not limited to this code in particular, the term RANS is used to refer to these computations and their results.

To reduce the initial development, a one-to-one correspondence between the LEM3D grid and the RANS grid was assumed. In other words, the control volumes in RANS are equal to the 3DCVs in LEM3D. Turbulence diffusivities are needed in the 3DCV centers. Due to the one-to-one grid correspondence, these values can be transferred to LEM3D without interpolation. The RANS code applies a non-staggered grid, which means that densities and velocities are stored in the control volume center. Thus, the velocities are interpolated to the control volume faces. The Rhie-Chow interpolation is used to obtain the boundary velocities during iteration to a

stationary solution (Ferziger and Peric, 2002). The boundary mass flux is given by multiplying the boundary velocity with the arithmetic mean of the density from the two adjacent control volume centers.

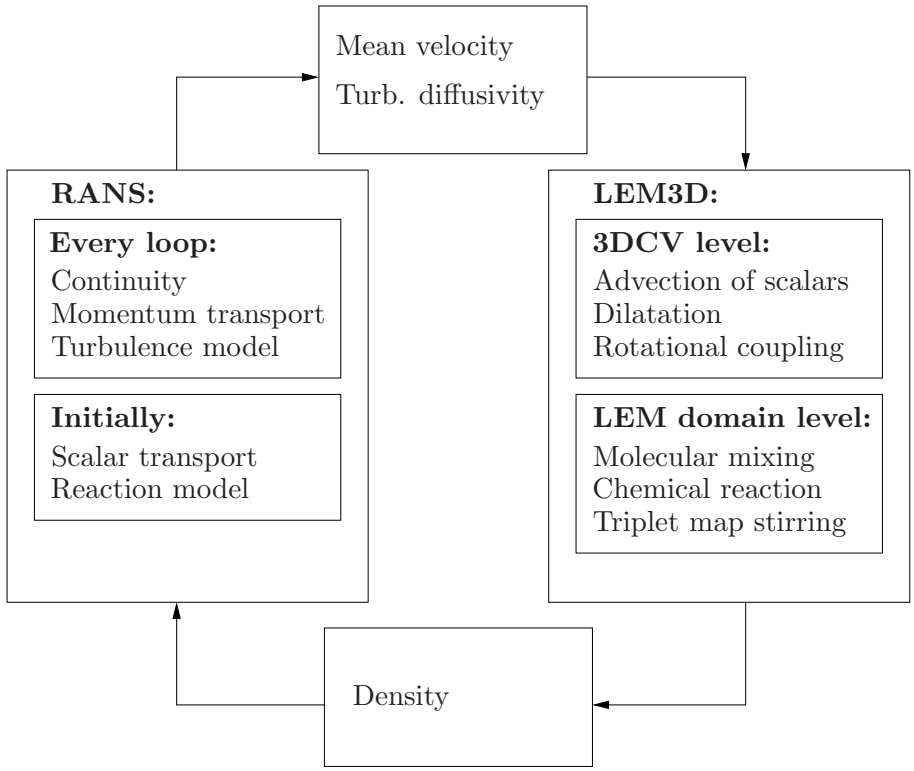

Figure 4.5: Schematic presentation of the two-way coupling between RANS and LEM3D. The one-way coupling excludes the density feed-back from LEM3D to RANS.

Figure 4.5 shows the principle coupling between LEM3D and RANS. One-way coupling is typically relevant for constant-density flows. For a one-way coupling that starts with a RANS computation, the iteration is finished after the first LEM3D simulation. The two-way coupling is necessary when the scalar evolution in LEM3D affects the density field and consequently the velocity field, e.g. for chemical reactions with heat release. The initial computation in the iteration loop between the models may be RANS involving scalar (species and energy) transport and a suitable combustion model. When RANS is run with density feedback from LEM3D, the transport equations for species and energy are not solved. In this case, RANS refers to solving the Favre-averaged transport equations for mass (3.3), mo-

mentum (3.4) and variables for the selected turbulence closure. Further in the iteration loop, LEM3D provides updated density fields to RANS. An average density for the 3DCV can be computed e.g. by Eq. (4.45). This density field, possibly altered by a relaxation factor, is directly supplied to the control volume center nodes in RANS. The coupled model is labeled RANS-LEM3D in the following.

4.5 Lagrangian implementation of wafer displacements

To maintain mean flow advection as a pure convective process, the wafer displacements are implemented in discrete, non-diffusive steps. The adopted algorithm ensures that continuity always is satisfied locally. The following sections outline the algorithm that in principle lets the RANS velocities projected at the 3DCV boundaries dictate the discrete displacement of wafers.

4.5.1 Indexing

The coordinates of the grid defined by the 3DCVs are given by the indices q, r, s in the x, y and z-direction respectively, where $q \in [1, N_x]$, $r \in [1, N_y]$, and $s \in [1, N_z]$. Thus, a scalar property φ that is defined for the 3DCVs is indexed by $\varphi_{q,r,s}$. Let $X^j_{p,r,s}$ define the position of a wafer on the r, s LEM domain in the x-direction at time t_j, where $t_j = t_0 + j\Delta t$. The index $p = p(l, q) = l + (q-1)M$ determines the position of the wafer on this LEM domain, where l is an index in the range 1 to M. Correspondingly, the position of wafers on the LEM domains in the y and z-directions at time t_j are uniquely determined by $Y^j_{p,s,q}$ and $Z^j_{p,q,r}$, where $p = l + (r-1)M$ and $p = l + (s-1)M$ for the two directions, respectively (see Fig. 4.6). A scalar property of a wafer located at $X^j_{p,r,s}$ at time t_j is further indexed by $\varphi(X^j_{p,r,s}, t_j)$ or alternatively $\varphi^j_{p,r,s}$.

When a wafer is displaced, it is moved from a given position in the domain to a destination that is originally occupied by another wafer. The wafer at the destination will have to move to another wafer position, and so forth. In other words, all wafer displacements are interdependent like bottles on a conveyor belt. This is due to the incompressibility assumption, and that each wafer represents a part of the model volume. Hence, the advection operation can be implemented simply by a shift of indices.

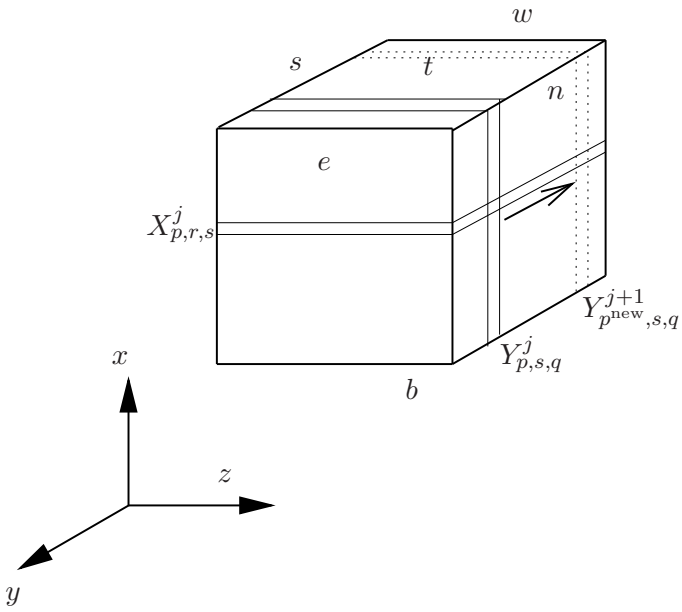

Figure 4.6: A 3DCV with definitions of face names related to the coordinate directions. Example of a wafer displacement is indicated from $Y^j_{p,s,q}$ to $Y^{j+1}_{p^{\text{new}},s,q}$.

4.5.2 Continuity equation

The mass conservation equation (2.1) can be rewritten as

$$-\frac{1}{\rho}\frac{D\rho}{Dt} = \nabla \cdot \mathbf{u}, \tag{4.8}$$

where $\nabla \cdot \mathbf{u}$ is the *dilatation*, which is the rate of increase of a material volume (Pope, 2000). The equation (4.8) is integrated over the 3DCV volume and time step Δt and Gauss divergence theorem is applied to the right-hand side to give

$$-\int_t^{t+\Delta t}\int_V \frac{1}{\rho}\frac{D\rho}{Dt} dt dV = \int_t^{t+\Delta t}\left[\int_S \mathbf{u}\cdot\mathbf{n}\, dS\right] dt, \tag{4.9}$$

where S and V are the surface area and volume of the 3DCV, respectively, and $\mathbf{n}$ is the normal surface vector. The dilatation associated with a 3DCV is approximated by the sum of all discrete volume expansions during Δt in the three intersecting domains of a 3DCV. Similarly, the right hand side of the above expression is represented by discrete displacements as presented in Sec. 4.3.3. By these approximations, the mass conservation (4.9) for a

3DCV is given by the identity

$$\sum_{i=1}^{M} \Phi_{x,i} + \sum_{i=1}^{M} \Phi_{y,i} + \sum_{i=1}^{M} \Phi_{z,i} = \delta_e - \delta_w + \delta_n - \delta_s + \delta_t - \delta_b, \tag{4.10}$$

where $\Phi_{x,i}$ is the discrete expansion (see Sec. 4.3.3) of wafer i on the LEM domain in the x-direction and δ_e, δ_w, δ_n, etc. are the integer number of wafers that are displaced over the respective 3DCV faces during the time step Δt (see Fig. 4.6 for the definition of indices). Note that by definition, a positive discrete expansion factor implies a density reduction. Due to the presented coupling between expansion and advection, the dilatation is implemented on the advective timescale. Thus, when the advective timescale is larger than the reactive timescale, the dilatation will lag the chemical reactions.

4.5.3 Approximation of the prescribed velocity field

Let $\overline{u}_{nn}$ denote the stationary mean velocity component that prescribes the wafer displacements over an arbitrary 3DCV face. The subscript nn is t or b for $i = x$, e or w for $i = y$, and n or s for $i = z$ (see Fig. 4.6). As mentioned, the velocity field is given from measurements or a flow solver. We define the *prescribed displacement* as

$$\gamma_{nn} \equiv \frac{3\overline{u}_{nn}\Delta t}{\Delta x_{\mathrm{w}}}, \tag{4.11}$$

which is the displacement in terms of the real number of wafers per time step. Note also that the transport rates in LEM3D are multiplied with a factor 3 as discussed in Sec. 4.2. The discrete approximation of γ_{nn}, denoted δ_{nn}, will vary from time step to time step unless γ_{nn} equals an exact integer number of wafers. For example if $\gamma_e = 2.4$ on average, δ_e varies between 2 and 3 in a manner that gives a displacement of 2.4 on average. The method which has been developed to ensure that the prescribed displacements are represented on average is denoted *banking* due to the bookkeeping of deviations from the prescribed value (Kerstein *et al.*, 2005-2006). Expressing the banking in general terms, the integer number of displacements of wafers over the 3DCV face nn for a given time step is

$$\delta_{nn} = \delta_{f,nn} + \delta_{r,nn}, \tag{4.12}$$

where $\delta_{f,nn}$ is the floor (see Appendix C) of the real number of displacements

$$\delta_{f,nn} = \lfloor \gamma_{nn} \rfloor, \tag{4.13}$$

and the *residual* from current and previous time steps is

$$\delta_{r,nn} = \lfloor r^0_{nn} + r_{nn} \rfloor. \tag{4.14}$$

In the expression above, r^0_{nn} is the *accumulated residual* from the previous advection advancements, whereas the residual from the current time step r_{nn} is given by

$$r_{nn} = \gamma_{nn} - \delta_{nn}. \tag{4.15}$$

The residual from the current time step is also referred to as the *deviation* between actual integer and prescribed displacements. When $\gamma_e = 2.4$, $\delta_{f,e} = 2$ by Eq. (4.13). From Eqs. (4.11), (4.14) and (4.15) it follows that the sequence of wafer displacements and residuals for consecutive time steps at this particular face will be: $[\delta_e = 2, r_e = 0.4]$, $[\delta_e = 2, r_e = 0.8]$, $[\delta_e = 3, r_e = 0.2]$, $[\delta_e = 2, r_e = 0.6]$, $[\delta_e = 3, r_e = 0.]$, etc.

The local instantaneous *wafer velocity* is further defined as

$$w_{nn} \equiv \frac{\delta_{nn} \Delta x_{\mathrm{w}}}{3\Delta t}. \tag{4.16}$$

By the *banking* the wafer velocity is on average equal to the prescribed velocity component, i.e., $\overline{w} = \overline{u}$.

If δ_{nn} was given by the banking for all boundaries enclosing a given 3DCV, there would be no degrees of freedom left for the variations in displacements and random volume expansion without a violation of continuity. Consequently, we let one of the displacement components be determined from the five respective displacements plus the dilatation during Δt. We assume that this is the top face component. Applying the discrete continuity equation given from Eq. (4.10), the displacement at this face is determined from

$$\delta_t = \delta_b + \delta_w - \delta_e + \delta_s - \delta_n + \sum_{i=1}^{M} \Phi_{x,i} + \sum_{i=1}^{M} \Phi_{y,i} + \sum_{i=1}^{M} \Phi_{z,i}. \tag{4.17}$$

To summarize, the displacements are in general estimated by two distinct methods. The banking method, which is given by Eq. (4.12), applies to inlet flow boundaries and generally all east, west, north and south 3DCV boundaries. The discrete continuity equation (4.17) estimates the top component.

For all cases considered in the present work, the bottom to top direction is considered the streamwise direction and the perpendicular directions accordingly the lateral. The displacements are calculated by starting at the

bottom upstream inlet layer of 3DCVs. First, the bottom inlet and the lateral displacements are calculated by the banking (4.12) for the first layer. Secondly, the top displacement components are given from the continuity equation (4.17). The top displacement component consequently becomes the bottom component in the following downstream layers of 3DCVs. The procedure is repeated layer by layer from the upstream to the downstream layer. In this way, all the 3DCV displacements are specified. However, the residuals from the discrete approximation of the prescribed displacements are ultimately accumulated in the streamwise components through Eq. (4.17). Hence, δ_t might deviate significantly from the prescribed value, γ_t. A method that reduces these deviations is proposed in the following section.

4.5.4 Minimizing deviations by the method of least squares

Since the displacement components are calculated successively as explained above, the deviation between the actual and prescribed displacement is prone to increase as we progress downstream. Thus, a method has been developed to minimize the deviation. This is done by applying discrete corrections $\Delta_{nn} \in (-\infty, ..., -3, -2, -1, 0, 1, 2, 3, ...\infty)$ to the displacement components such that the square sum of deviations,

$$d^2 = \sum_{nn}^{N_{\text{face}}} (r_{nn} + \Delta_{nn})^2 \,, \tag{4.18}$$

is minimized subject to the constraint $\Delta_e - \Delta_w + \Delta_n - \Delta_s + \Delta_t = 0$.[5] Since the bottom component is given from the upstream layer of 3DCVs, or the first inlet layer, this component is not subject to corrections. The deviation for the displacement component at face nn is given by the expression (4.15). The lateral components (e, w, s, n) are shared between 3DCVs, and hence the minimization procedure is only feasible for the 3DCVs belonging to a checkerboard subset of the domain. The subset is alternated between layers and from time step to time step.

Equation (4.18) is implemented stepwise as follows for a given 3DCV. If $|\delta_t - \gamma_t| > \delta_{\text{th}}$, where δ_{th} is a predefined integer threshold, the combination of $\Delta_t \pm 1$ and $\Delta_{nn} \pm 1|_{nn \neq b,t}$ that minimizes d^2 is chosen. This is performed until $|\delta_t - \gamma_t| < \delta_{\text{th}}$ or as long as d^2 is reduced.

[5] The constraint stems from the requirement that the corrections should not violate continuity principally given by $\int_S \mathbf{\Delta} \cdot \mathbf{n} \, dS = 0$, where $\mathbf{\Delta}$ is the discrete correction vector.

4.5.5 Donors and receivers

If, for a given 3DCV, the situation is such that e.g. $\delta_t \neq \delta_b + \sum_{i=1}^{M} \Phi_{x,i}$, a given number of wafers must be donated to or received from one or two of the orthogonal domains intersecting the 3DCV. Let $\Theta_{x,q,r,s}$ be the number of wafers that are donated or received from the domain in the x-direction that intersect the 3DCV at q, r, s. A positive $\Theta_{x,q,r,s}$ means that the domain is donating wafers, while a negative $\Theta_{x,q,r,s}$ means that it is receiving wafers. The following description refers also here to a given 3DCV, so the subscripts q, r, s are skipped for clarity. We define Θ_x, Θ_y and Θ_z for the three domain sections that intersect in a given 3DCV as

$$\Theta_x = \delta_b - \delta_t + \sum_{i=1}^{M} \Phi_{x,i}, \tag{4.19}$$

$$\Theta_y = \delta_w - \delta_e + \sum_{i=1}^{M} \Phi_{y,i}, \tag{4.20}$$

$$\Theta_z = \delta_s - \delta_n + \sum_{i=1}^{M} \Phi_{z,i}. \tag{4.21}$$

Adding Eqs. (4.19)–(4.21) and using the discrete continuity equation (4.17), it follows that

$$\Theta_x + \Theta_y + \Theta_z = 0. \tag{4.22}$$

Each of the 3 intersecting domain sections in a 3DCV can either be a donor, a receiver or a neutral domain. In other words, Θ_x, Θ_y and Θ_z can either be positive, negative or zero. From this we get four classes of combinations categorized by the number of donors, receivers and neutrals we have for a particular 3DCV: There are 3 possible combinations when Θ is positive for one of the domain sections and negative for the two respective. This is categorized as the first *class* of combinations. For the second class, we have 3 combinations when Θ is positive for two domains and negative for the third. When Θ is zero for one domain, there are two combination for the two respective (positive or negative), and this gives in total 6 combinations for the three directions being zero. This is the third class. Finally, the fourth class is that Θ is zero for all domains. In sum, there are 13 possible sign-combinations of Θ_x, Θ_y and Θ_z that satisfy Eq. (4.22). The 4 classes of combinations are treated separately in the numerical implementation.

Wafers that are donated from a domain are first extracted from the 3DCV center prior to advection advancement (see Fig. 4.7). Second, an open slot is created in the center of the receiver domain corresponding to

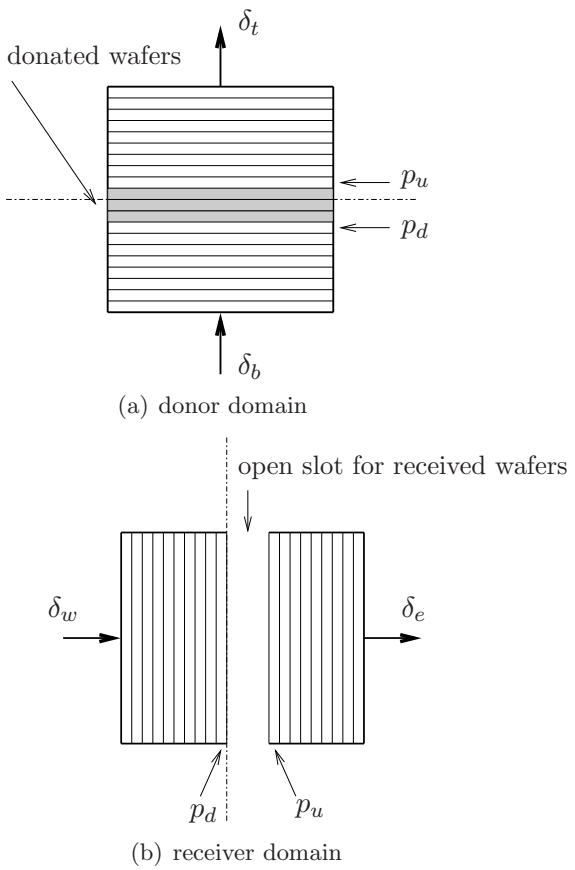

Figure 4.7: An example of flipping in a 3DCV where the part of the domain in (a) is a donor, and the part of the domain in (b) is a receiver. The domains overlap in the same 3DCV, but are shown separately for clarity. The parcel of wafers which is flipped (shaded), is extracted from the donor domain and inserted in the center of the receiver domain where indicated.

the number of donated wafers plus the number of wafer volumes needed for the possible expansion events among the donated wafers. Third, the parcel of wafers are flipped, expanded if necessary, and inserted in the open slot on the receiver domain. This operation is in the following referred to as *flipping*. Finally, the flipped wafers are displaced according to the prescribed displacement along with the wafers on the receiver domain. The motivation for orienting the flipping around the 3DCV center is that the distance the wafers are moved by the flipping, which in effect is a kind of artificial dispersion, is minimized. When more than one wafer is flipped, the wafers are either rotated clockwise or counterclockwise. The latter is

selected randomly.

The flipping is related to the representation of mean flow advection. However, the operation increases the number of scalar interfaces. Hence, there is a certain degree of spurious diffusion associated with the flipping. Similar versions of the flipping procedure are also presented in Kerstein (2002) and Sannan *et al.* (2008).

4.5.6 Implementation of wafer displacements

By the prescribed velocities and the discrete continuity equation, the displacements are given at every 3DCV face at every time step. The previous section illustrated the flipping of wafers for stagnating or accelerating flow. This section presents the expression for the displacement of non-flipped wafers for a given 3DCV, and outlines the principle procedure for numerical implementation.

The Lagrangian displacement of a fluid particle is given by Eq. (3.21). This equation is time integrated using the forward Euler scheme which gives

$$X_i^+(t_j + \Delta t, \boldsymbol{X}^0) = X_i^+(t_j, \boldsymbol{X}^0) + u_i \left[\boldsymbol{X}^+(t_j, \boldsymbol{X}^0), t_j\right] \Delta t, \tag{4.23}$$

where u_i is the fluid particle velocity. Now, let the fluid particle be represented by a wafer on an x-oriented LEM domain at the position $X^j_{p,r,s}$ at time t_j (see Sec. 4.5.1). The current description is only referring to a given LEM-domain, so we omit the indices r, s for convenience. For this particular wafer, Eq. (4.23) is written as

$$X_p^{j+1} = X_p^j + w_p^j \Delta t, \tag{4.24}$$

where w_p^j is the velocity of the wafer X_p^j at time t_j. The wafer velocity is determined from the 3DCV prescribed boundary velocities as described in the following.

We assume that the 1D-resolution, M, is an even number. Thus, the exact center of the 3DCV is on the boundary between two wafers. Let p_d and p_u denote the wafer position immediately below and above the 3DCV center on a receiver domain, respectively. On a donor domain, p_d and p_u are the wafer positions immediately below and above the parcel of flipped wafers.[6] This is illustrated in Fig. 4.7. We define the reference for the first wafer in the 3DCV q as $p_1 = (q-1)M + 1$. In the following, we refer to the wafer positions $X_p^j \leq X_{p_d}^j$ as being below the 3DCV center and $X_p^j \geq X_{p_u}^j$

[6]Remember that the donated wafers are expanded, if applicable, *before* they are inserted on the receiver domain.

as being above. This is independent of whether the domain intersecting the 3DCV is a donor, a receiver or a neutral domain.

For wafers below the 3DCV center, the displacement is given by

$$w_p^j \Delta t = \left(\delta_b + \sum_{i=p_1}^{p} \Phi_{x,i} \right) \Delta x_{\mathrm{w}}, \tag{4.25}$$

where $\sum_{i=p_1}^{p} \Phi_{x,i}$ is the dilatation below and including the wafer of consideration and the displacement across the lower 3DCV boundary δ_b is a compressed notation for $\delta_b|_{q,r,s}^{j}$. For all wafers above their respective 3DCV centers, we have that

$$w_p^j \Delta t = \left(\delta_b + \sum_{i=p_1}^{p_d} \Phi_{x,i} - \Theta_x + \sum_{i=p_u}^{p} \Phi_{x,i} \right) \Delta x_{\mathrm{w}}, \tag{4.26}$$

where Θ_x is the number of wafers donated to or received from the domain. By inserting Eq. (4.25) and (4.26) into equation (4.24) we get the new position X_p^{j+1} for all wafers in reference to the original wafer position

$$\begin{aligned} X_p^{j+1} &= X_p^j + \left(\delta_b + \sum_{i=p_1}^{p} \Phi_{x,i} \right) \Delta x_{\mathrm{w}}, \quad p_1 \le p \le p_d \\ X_p^{j+1} &= X_p^j + \left(\delta_b + \sum_{i=p_1}^{p_d} \Phi_{x,i} - \Theta_x + \sum_{i=p_u}^{p} \Phi_{x,i} \right) \Delta x_{\mathrm{w}}, \quad p_u \le p \le qM \end{aligned} \tag{4.27}$$

In practice, the wafer positions are not calculated as given above. There is no need to store the positions since they are uniquely defined by the indices. Thus, the advection advancement is implemented by a shift of indices. Let $\varphi_{p,r,s}^j$ be the scalar value at the position $X_{p,r,s}^j$ on a x-oriented LEM domain. The displacement according to Eq. (4.27) is performed by assigning a new position to the wafer property, i.e., $\varphi_{p,r,s}^j \rightarrow \varphi_{p^{\mathrm{new}},r,s}^{j+1}$, where

$$p^{\mathrm{new}} = p + \delta_b + \sum_{i=p_1}^{p} \Phi_{x,i}, \qquad p_1 \le p \le p_d, \tag{4.28}$$

$$p^{\mathrm{new}} = p + \delta_b + \sum_{i=p_1}^{p_d} \Phi_{x,i} - \Theta_x + \sum_{i=p_u}^{p} \Phi_{x,i}, \qquad p_d \le p \le qM. \tag{4.29}$$

The Eqs. (4.28) and (4.29) and corresponding expressions for the LEM domains in the y- and z-directions, along with the flipping procedure described in Sec. 4.5.5, determines the implementation of the advection advancement for every wafer in LEM3D.

In general, there is only one necessary requirement to the wafer advection; the number of flipped wafers cannot exceed the number of available wafers in the donor domain. It is nevertheless desirable that the distance the wafers are displaced is less than Δx on average, where Δx is the length of the 3DCV. A CFL number is introduced based on the latter requirement, and is given by

$$\mathrm{CFL}_{\mathrm{adv}} = \frac{3\overline{u}_{\max}\Delta t}{\Delta x}, \tag{4.30}$$

where $\overline{u}_{\max}$ is the maximum prescribed velocity component. The factor 3 is introduced due to the 3 representations of the domain volume as explained in Sec. 4.2. The condition (4.30) limits the global time step that is used to calculate the prescribed displacements in Eq. (4.11).

4.6 Time scales

The nature of turbulent combustion consists of a magnitude of time scales related to advection, molecular diffusion and chemical reactions. In the present model, these time scales are represented by a number of corresponding modeling time scales. The advective time scale is related to the mean velocity component by

$$\tau_{\mathrm{adv}} = \frac{\Delta x}{\overline{u}}, \tag{4.31}$$

and the turbulence diffusive time scale is related to the turbulence diffusivity by

$$\tau_{\mathrm{diff}} = \frac{\Delta x^2}{2D_{\mathrm{T}}}. \tag{4.32}$$

The molecular diffusive time scale τ_{M} is similarly defined by substituting the turbulence diffusivity by the molecular diffusivity D_{M} in the expression above. Turbulent stirring is in LEM3D represented by triplet map events, which will occur on a characteristic time scale of $\tau_{\mathrm{triplet}} = 1/R$, where R is the mean rate of stirring events.

The chemical processes occur on a wide range of time scales (Warnatz *et al.*, 2001). Generally, the smallest chemical time scales τ_{chem} will be resolved by time stepping on the individual LEM domains. However, the dilatation resulting from thermal expansion is currently implemented on the advective time scale. This is anyhow not exact, so as a general rule, the

$\mathrm{CFL_{adv}}$-number should be kept low to reduce the lag between reactions and dilatations.

4.7 Auxiliary coupling by random rotations

Exchange of scalars between domains occurs to some extent through the coupling introduced by the advection operations.[7] This is denoted the *advective coupling*. However, for a scalar to be spread in all directions according to the prescribed turbulence and mean velocity field, there is a need for an *auxiliary* coupling mechanism. We can easily realize the need for an auxiliary coupling in order to have a scalar spread in all possible directions in homogeneous turbulence, where the mean flow is uniform in one of the coordinate directions and zero in the two respective.

4.7.1 Implementation of 3DCV rotations

Motivated by the rotational character of turbulent eddies, the auxiliary coupling is introduced by random *rotations* of the 3DCVs (Kerstein, 2004; Sannan *et al.*, 2008). The 3DCVs are rotated clockwise or counterclockwise about one of the three coordinate axes, switching the wafers on the two intersecting domains being involved in the rotation (see Fig. 4.8). The wafers on the domain parallel to the axis of rotation remain unaffected by the rotation. This gives in total 6 different options for a rotation, which is summarized by the following relations. The clockwise rotation about the x-axis switches wafers on the y- and z-domains according to

$$\begin{aligned} Z_l &\rightarrow Y_l \quad l = 1, M, \\ Y_l &\rightarrow Z_{M+1-l} \quad l = 1, M. \end{aligned} \tag{4.33}$$

Similarly the counterclockwise rotation is given by

$$\begin{aligned} Z_l &\rightarrow Y_{M+1-l} \quad l = 1, M, \\ Y_l &\rightarrow Z_l \quad l = 1, M. \end{aligned} \tag{4.34}$$

Corresponding expressions hold true for the rotations about the y- and z-axis. Thus, for the clockwise and counterclockwise rotation about the y-axis, Z is replaced by X and Y is replaced by Z in the expressions (4.33) and (4.34). Finally, for the rotation about the z-axis, Z is replaced by Y and Y by X in the above expressions. As in Sec. 4.5.6, the rotations are also implemented by a shift of indices.

[7] Some wafers are flipped in between domains if the flow is stagnating or accelerating locally.

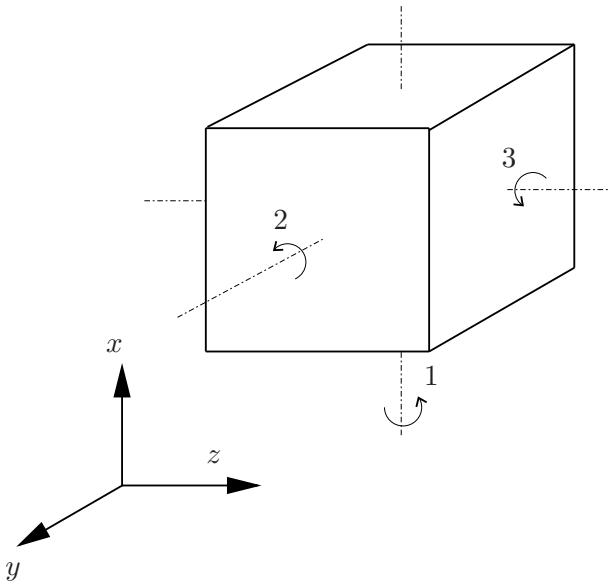

Figure 4.8: The 6 different options for rotation of a 3DCV about the x, y and z-axis. The three counterclockwise rotation directions are indicated by the arrows.

The *relative rotation frequency* ν_r is the number of rotations that on average should influence a wafer when it passes through a given 3DCV. When the advective time scales are dominant, the frequency of rotation in units of rotations per second is given by

$$\mathcal{R} = \frac{3\nu_r}{\tau_{\text{adv}}}. \tag{4.35}$$

The factor 3 is due to the factor that multiplies the prescribed velocities. The relative rotation frequency is generally a LEM3D model parameter that may be tuned. It can be shown that the probability of a rotation per time step is given by $\text{CFL}_{\text{adv}}\nu_r$, where $\text{CFL}_{\text{adv}}\nu_r \leq 1$ gives an additional restriction to CFL_{adv}.[8]

If the advective time scales are varying over the domain, it is appropriate to define a local rotation frequency calculated by

$$\mathcal{R}_{q,r,s} = \mathcal{R}_{\max}\frac{\max\left[\overline{u}_x, \overline{u}_y, \overline{u}_z\right]_{q,r,s}}{\overline{u}_{\max}}. \tag{4.36}$$

[8]Note that only 2/3 of the rotations influence the wafers in a given direction. If this is taken into account, $\text{CFL}_{\text{adv}}\nu_r \leq 2/3$ to have at least one rotation per time step on average.

Due to the random rotations, a scalar will reside on domains in a given direction only 1/3 of the time. The correct average transport rates are accommodated by multiplying the large-scale transport properties with a factor 3, as also mentioned in Sec. 4.2.

4.7.2 An estimate for additional dispersion from rotations

Kerstein *et al.* (2007) consider a rotation cycle where a wafer is transferred from a given domain by a 3DCV rotation, subjected to a number of intermediate deterministic and random processes, before it is transferred back to its original domain direction by a second rotation event. The intermediate processes might constitute mean flow advection, random triplet map stirring, and random rotations in between the two other respective domain directions. Figure 4.9 illustrates a rotation cycle, where the z-direction is omitted for simplicity.

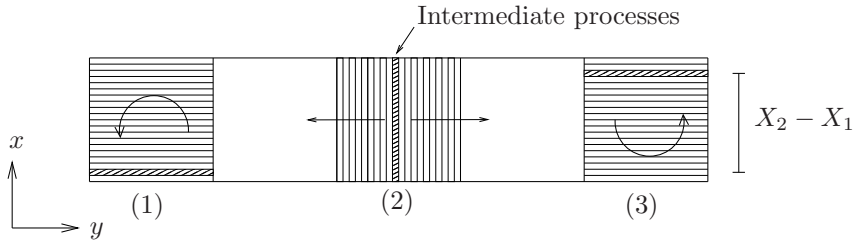

Figure 4.9: The rotation cycle consists of the following elements: (1) A random rotation influencing the wafer at X_1, (2) an arbitrary number of intermediate random and deterministic processes, and (3) a rotation back to the original domain direction to the position X_2.

To derive an expression for the diffusivity induced by such a rotation cycle we apply the following assumptions:

- We apply a continuous approach, corresponding to the limit $M \to \infty$.
- We neglect molecular diffusion during the rotation cycle.
- There is an equal probability of the wafer starting at any position, X_1, where the probability density function reads $f(X_1) = 1/\Delta x$, where Δx is the 3DCV size.
- There is also an equal probability of ending up anywhere in the original domain direction, X_2, and the probability density function reads $f(X_2) = 1/\Delta x$.

- The rotation cycle consists of random displacement processes in between two rotation events that influences the domain in the x-direction. Hence, the start position X_1 and end position X_2 are within the range of the same 3DCV, but they can be on different x-oriented LEM domains.

Let $\overline{(\Delta X)^2} = \overline{(X_1 - X_2)^2}$ be the mean square displacement of wafers in the x-direction. The analogy to random walk is evident, so the diffusivity in the x-direction induced by random rotations can be estimated following Hinze (1975) to

$$D_{\mathrm{r}} = \frac{1}{2}\mathcal{R}_x\overline{(\Delta X)^2}, \tag{4.37}$$

where $\mathcal{R}_x$ is the number of rotations per unit time that influences the x-domain. The mean square displacement is now given by the following integral

$$\begin{aligned}\overline{(\Delta X)^2} &= \int_0^{\Delta x} f(X_1)X_1 dX_1 \int_0^{\Delta x} f(X_2)(X_1 - X_2)dX_2 \\ &= \frac{1}{(\Delta x)^2}\int_0^{\Delta x}\int_0^{\Delta x} X_1(X_1 - X_2)dX_1 dX_2 = \frac{(\Delta x)^2}{12}.\end{aligned} \tag{4.38}$$

There are only 2/3 of the rotations that influence the x-direction, and since the rotation cycle consist of two such rotations, we have that $\mathcal{R}_x = \mathcal{R}/3$. This gives

$$D_{\mathrm{r}} = \frac{(\Delta x)^2}{36}\mathcal{R}. \tag{4.39}$$

Equation (4.39) is a simplified, however, useful estimate. The estimate was employed in the analysis of dispersion from a point source as presented in Chapter 6.

4.8 Implementation of boundary conditions

The boundary conditions in LEM3D are needed at two levels. First, we need to determine the conditions for LEM processes that occur on each 1D domain. Secondly, the wafer displacements, which are prescribed by the velocity components on a 3DCV level, also need boundary conditions specified. In this work, the boundaries of LEM3D are placed sufficiently far from the part of the domain that is of interest.

4.8.1 LEM processes

Every LEM domain in the three-array structure has two boundaries that must be specified. If we assume that the boundaries are closed, molecular diffusion is treated with a zero-gradient von Neumann condition, and the triplet maps that extend out of the domain are truncated. This will influence the solution inside the domain, and therefore the domain should be large enough to maintain the solution of interest unaffected by the boundaries. As an alternative the LEM domain may have cyclic boundaries. This applies both to molecular diffusion and triplet map stirring.

4.8.2 Wafer displacements

Each LEM domain is extended with a *guard zone* outside the LEM3D domain boundaries. This zone, which is more of a technical requirement, is primarily constructed to have wafers available at inlets. The wafers in the guard zone are only relevant to the advection advancement, and do not take part in molecular diffusion or triplet map stirring.

The streamwise inlet and all lateral velocity components are matched to the prescribed components by the banking, as described in Sec. 4.5.3. These components alternate between the two nearest integers to the prescribed displacements from time step to time step. The properties of the wafers in the guard zone for such inlet boundary components are fixed.

The streamwise components are estimated from continuity (4.17). Since this is performed layer by layer, the top components at the downstream domain boundary will contain residuals accumulated from all layers. Thus, the top 3DCV boundaries may sporadically behave as an inlet even though it is an outlet on average. This applies also to the lateral boundaries if the deviations are minimized by the least squares method as described in Sec. 4.5.4. Boundaries that may act both as inlets and outlets are either specified by assuming fixed properties, or by setting the values equal to the neighboring mean 3DCV filtered value. The latter method was applied to the cases in Chapter 7 and 8.

4.9 Data gathering

In LEM3D, the sampling time interval must be set so that individual samples are independent. Data are sampled after initial transients have been relaxed, so initial conditions will not influence the gathered statistics. Let $\varphi(t_j, X_p)$ be the scalar value of the wafer X_p on a x-domain in a given 3DCV

at time t_j. The mathematical expectation (the mean) of $\varphi(X_p)$ is estimated by taking the average of all the available N_s samples

$$\overline{\varphi}(X_p) = \frac{1}{N_s} \sum_{j=1}^{N_s} \varphi(X_p, t_j). \tag{4.40}$$

The second- and higher-order central moments of order r are estimated by sampling the raw moments given by

$$\mu'_r(X_p) = \frac{1}{N_s} \sum_{j=1}^{N_s} [\varphi(X_p, t_j)]^r, \tag{4.41}$$

where the first raw moment is the mean value. These raw moments are sampled in every wafer on every LEM domain of interest. By rearranging the expression (2.16), the central moments can be expressed in terms of the raw moments by

$$\begin{aligned} \mu_2 &= -{\mu'_1}^2 + \mu'_2, \\ \mu_3 &= {\mu'_1}^3 - 3\mu'_1\mu'_2 + \mu'_3, \\ \mu_4 &= \text{etc.} \end{aligned} \tag{4.42}$$

The second, third and fourth central moments are denoted the *variance*, the *skewness*, and the *kurtosis*, respectively. In the model, the central moments are post-processed from the sampled raw moments by the expressions (4.42). The highest moment considered in this work is the second.

The spatial *autocovariance* (2.18) between scalar values at X_0 and X_p can be rewritten and scaled, to get the *autocorrelation function*

$$\varrho(X_p) \equiv \frac{R(X_p)}{R(X_0)} = \frac{\overline{\varphi(X_0)\varphi(X_p)} - \overline{\varphi(X_0)}\;\overline{\varphi(X_p)}}{\overline{\varphi'(X_0)\varphi'(X_0)}}. \tag{4.43}$$

The autocorrelation for scalars along a LEM domain is estimated by sampling the first right-hand-side term in the autocovariation expression (4.43) by

$$\overline{\varphi(X_0)\varphi(X_p)} = \frac{1}{N_s} \sum_{j=1}^{N_s} \varphi(t_j, X_0)\varphi(t_j, X_p), \tag{4.44}$$

and using the estimated mean for $\varphi(X_0)$ and $\varphi(X_p)$ and the second moment for $\varphi(X_0)$ to post-process the autocorrelation.

The filtered mean value of a 3DCV which is sampled by

$$\overline{\widehat{\varphi}}_{q,r,s} = \frac{1}{N_s} \sum_{j=1}^{N_s} \left[\widehat{\varphi}^j_{q,r,s} \right], \tag{4.45}$$

is found by applying a filter to the intersecting LEM domains at the given 3DCV. The instantaneous 3DCV filtered value, $\widehat{\varphi}^j_{q,r,s}$, is determined by a box filter that is 1 inside the 3DCV and 0 elsewhere, giving

$$\widehat{\varphi}^j_{q,r,s} = \frac{1}{3M} \left(\sum_{p=p_1}^{qM} \varphi(X_{p,r,s}, t_j) + \sum_{p=p_1}^{rM} \varphi(Y_{p,s,q}, t_j) + \sum_{p=p_1}^{sM} \varphi(Z_{p,q,r}, t_j) \right). \tag{4.46}$$

For simplicity, the filtered mean value is denoted $\widehat{\varphi}$ throughout the thesis. If we perform the sums over wafers first (Eq. 4.46), and the sum over samples secondly (4.45), the data storage for the filtered mean is reduced to one value per 3DCV.

4.10 Simulation procedure

The following section describes the general simulation procedure for LEM3D including the one-way and the two-way coupling to RANS. A schematic setup of the procedure is given in Fig. 4.5. For constant density and one-way coupling, the velocity and turbulence diffusivity fields are generally supplied from measurements, analytical expressions[9] or a flow solver. In that case, the procedure starts at step (2) below.

For the two-way coupling, the initial velocity and turbulence fields can either be supplied by RANS with appropriate physical and chemical models or by an initial guessed field. In the former case the procedure starts at step (1), whereas in the latter case it starts at step (2).

(1) The Favre-averaged RANS-equations (mass, species, momentum, energy and turbulence equations) are solved by iteration to a stationary solution. This provides the initial velocity and turbulence diffusivity fields needed as input to LEM3D.

(2) For every LEM domain, initially at every LEM3D simulation, the eddy size distribution is calculated from Eq. (4.4), and the eddy frequency parameter is calculated from Eq. (4.5). The turbulence diffusivity D_T in Eq. (4.5) is taken as the spatially average turbulence diffusivity for

[9] See e.g. chapter 5 and 8 for similarity solutions in a turbulent jet.

the LEM domain. The lateral prescribed displacements are further calculated from Eq. (4.11).

(3) The following substeps are implemented for every advective time step Δt.

(a) The auxiliary coupling is ensured by randomly sampling whether a rotation should occur, and if so, which of the 6 options that should be implemented. The latter is sampled from an even distribution, and the probability of rotation is given by $\nu_r \mathrm{CFL}_{\mathrm{adv}}$.

(b) The dilatation is determined by a criterion, e.g. by calculating the pressure indicator, p^+, from the equation of state (4.7). This is the general approach, however, in the present work the discrete dilatation is sampled from a distribution (see e.g. Chapter 7) and implemented as described in Sec. (4.3.3). Note that the density ρ_0 is transported with the wafer.

(c) Inlet streamwise, and lateral discrete displacement components are given from the banking (4.12), while the top component is given from the continuity equation (4.17).

(d) Necessary corrections are performed according to Eq. (4.18).

(e) The advection and possible expansions are implemented by first performing the inlet wafer displacements, and then successively for every 3DCV:

i. Displace the wafers upstream of the 3DCV center by a shift of indices according to Eq. (4.28).

ii. Carry out the necessary flipping as described in Sec. 4.5.5.

iii. Implement the displacements downstream of the center by a shift of indices given by Eq. (4.29).

(f) The following is performed simultaneously on every LEM domain in three stacks on sub time steps from t to $t + \Delta t$:

i. The time for the next triplet map event t_{TM} is sampled from the Poisson distribution (4.6).

ii. Following an explicit method, the one-dimensional diffusion difference equation (4.1) is time marched with time step Δt_{w} until $t = t + t_{\mathrm{TM}}$. The diffusive time step is given by Eq. (4.2). For an implicit method, the equation set (4.3) is solved by the TDMA method.

iii. At $t = t + t_{\mathrm{TM}}$, a triplet map is implemented on the LEM domain with the size sampled from the cumulative distributions constructed from Eq. (4.4) and the position from a distribution representing the turbulence diffusivity variation over the domain.

iv. The steps (f)i. through (f)iii. are repeated until $t = t + \Delta t$.

(g) Data for the means (4.40), the 3DCV filtered means (4.45), the raw moments (4.41), and the covariation (4.44) are sampled at the last step in the LEM3D time step cycle. In general, the sampling is not performed at every time step, but at an interval sufficiently large to provide statistically independent samples.

(4) The steps (3)(a) through (3)(g) are repeated until statistical convergence of the data sampled in (3)(g) is reached. Finally, the statistical data are post-processed as described in Sec. 4.9.

(5) For one-way coupling the simulation is now completed. For two-way coupling, e.g. for variable density flows, the steps (1) through (4) are repeated until convergence between LEM3D and RANS. The density field in RANS is given from the updated 3DCV filtered density field in LEM3D. The solution might be relaxed for better overall convergence.

4.11 The two-dimensional Linear Eddy Model

The two-dimensional Linear Eddy Model, denoted LEM2D, has been developed to investigate the effects of random rotations in a simpler configuration. In addition, the computer memory requirement is significantly less than for a corresponding LEM3D calculation, which allows for relatively larger computational domains with finer resolution. Figure 4.10 shows the setup of the model. LEM domains resolved in the y- and z-directions are organized in a two-dimensional structure. 2DCVs are defined where the LEM domains cross. Contrary to the LEM3D, rotations of 2DCVs are only performed in between two domain directions, leaving us with in total 2 different possibilities of rotations; clockwise and counterclockwise around an axis in the inactive x-direction. This also means that both directions are influenced at every rotation event. Hence, the model corresponding to Eq. (4.39) for additional dispersion in LEM2D is given as

$$D_{\mathrm{r}} = \frac{(\Delta x)^2}{24}\mathcal{R}. \tag{4.47}$$

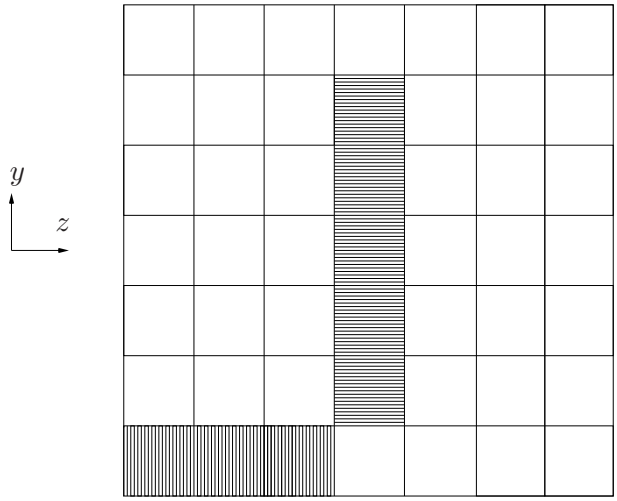

Figure 4.10: The figure displays the setup for the LEM2D. The 2DCVs are resolved by wafers in the y- and z-directions as indicated.

Due to the random rotations, a scalar will only reside 1/2 of the time on LEM domains in a given direction. This implies that the main transport property, which in this case is the turbulence diffusivity, is multiplied with a factor 2 to provide the correct scalar transport on average. The rotation frequency is accordingly given as

$$\mathcal{R} = \frac{2\nu_r}{\tau_{\text{diff}}}, \tag{4.48}$$

where τ_{diff} is given by Eq. (4.32).

The simulation principally follows the steps (2) to (4) in the procedure in Sec. 4.10, where the items related to advection and expansion, i.e., (3)(b) through (3)(e) are omitted. For item (3)(a), the probability of a random rotation is given as $\nu_r \text{CFL}_\text{T}$, where the relative rotation frequency is related to the turbulence diffusive timescale by Eq. (4.48) and (4.32). The role of the CFL_T-number is to ensure that the probability of rotation is less than one.

Simulations are typically run from the same initial condition with different random-number seeds for a given time. This is one *realization*. Data are gathered as described in (3)(g) after every realization and post-processed as given Sec. 4.9 at the simulation end.

4.12 Computational cost

The total simulation time for a numerical algorithm can be estimated by

$$T_{\mathrm{tot}} = N_{\mathrm{p}} N_{\mathrm{t}} T_{\mathrm{pt}}, \tag{4.49}$$

where N_{p} is the total number of grid nodes, N_{t} the total number of time steps needed (in order to gather enough statistics), and T_{pt} is the time spend for one time step at each node. T_{pt} is a function of the number of equations solved and the cpu time spent for each operation (Ertesvåg, 2000).

For a fair comparison of DNS and LEM3D, we consider a "reduced" DNS, where only the transport equations for the reacting scalars are solved. Hence, the same number of equations are solved in LEM3D and DNS. The assumption is made that the time for solving three copies of the 1D-equations, corresponds to solving one copy of the 3D-equations.[10] This gives

$$(N_{\mathrm{t}} T_{\mathrm{pt}})_{\mathrm{DNS}} \sim (N_{\mathrm{t}} T_{\mathrm{pt}})_{\mathrm{LEM3D}}\,. \tag{4.50}$$

LEM3D consists of stacks of one-dimensional domains in three directions, so the number of nodes resolving the domain is

$$N_{\mathrm{p,LEM3D}} = N_x M N_y N_z + N_y M N_x N_z + N_z M N_y N_x = N_x N_y N_z 3M. \tag{4.51}$$

We further assume that the space resolution is the same for DNS and LEM3D, i.e., $\Delta x_{\mathrm{DNS}} = \Delta x_{\mathrm{w}}$. Thus, the number of nodes needed in DNS expressed in terms of N_x, N_y, N_z, and M is

$$N_{\mathrm{p,DNS}} = N_x M \times N_y M \times N_z M = N_x N_y N_z M^3. \tag{4.52}$$

This gives the relation between the resolution requirement in DNS and LEM3D as

$$N_{\mathrm{p,LEM3D}} = \frac{3 N_{\mathrm{p,DNS}}}{M^2}. \tag{4.53}$$

Applying the Eqs. (4.53) and (4.50) in the expression (4.49), it follows that the simulation time in LEM3D corresponds to DNS on the order of

$$T_{\mathrm{tot,LEM3D}} \sim \frac{T_{\mathrm{tot,DNS}}}{M^2}. \tag{4.54}$$

Thus, the cost saving achieved with LEM3D in comparison to DNS is first and foremost influenced by the 1D-resolution M.

[10] The type of numerical schemes applied, and the time step differences may influence the accuracy in this assumption.

To illustrate what this means, we consider a turbulent reacting flow with an integral scale of 10^{-2} m. A typical fast chemical time scale may be on the order of $\tau_{\text{chem}} \sim 10^{-8}$ s (Warnatz *et al.*, 2001). The flame thickness can further be estimated to $\delta_r \sim (D_{\text{M}}\tau_{\text{chem}})^{1/2} \sim 10^{-6}$ m (Borghi, 1988) if D_{M} is taken as 10^{-4} m^2/s. If Δx in LEM3D is set to 1/10 of the integral scale, the 1D-resolution becomes $M = \Delta x/\Delta x_{\text{w}} = 10^{-3}/10^{-6} = 10^3$. From Eq. (4.54), the LEM3D simulation time is estimated to $T_{\text{tot,LEM3D}} \sim 10^{-6} T_{\text{tot,DNS}}$. This gives that, for this particular case, a DNS taking one month is completed in a few seconds with a corresponding LEM3D.

Chapter 5

Test cases A: Advection and random rotations

5.1 Introduction

This chapter investigates the representation of mean flow advection by discrete displacement of wafers and the auxiliary coupling by random rotations of 3DCVs. The chapter consists of two parts. The prescribed mean velocity field can generally not be represented by an integer number of wafer displacements at every instant. Hence, the representation of mean flow advection by discrete displacements will necessarily result in instantaneous deviations from the mean velocity. The magnitude of these deviations, and the sensitivity to some selected parameters, was examined, and is presented in the first part. The second part presents simulations in a simplified quasi one-dimensional setup investigating the effect of random rotations on mean and root mean square (rms) travel time of a trace wafer.

Even though the investigations revealed some artifacts related to the random rotations and discrete representation of mean flow advection, it is important to note that LEM3D, as expected, was able to represent the prescribed mean velocity on average. The mean travel time of a wafer was also well captured when the time was measured in between corresponding locations in the domain.

5.2 Case A1: Representation of the velocity field

The concept of representing the mean flow advection by discrete displacements of wafers was tested in a relatively simple flow configuration, namely

the self-similar region of a turbulent jet. The *wafer velocity* is the local instantaneous velocity of the wafer defined by the expression (4.16). Analogous to Reynolds decomposition (White, 1991), the wafer velocity is here decomposed into the mean prescribed velocity and a fluctuation

$$w_{nn} = \overline{u}_{nn} + w'_{nn}. \tag{5.1}$$

To distinguish these fluctuations from turbulent velocity fluctuations, the deviation from the prescribed mean velocity w' is in the following denoted *jitter*.

5.2.1 Jitter

Every prescribed face velocity in the domain can be expressed as a fraction of the maximum velocity component

$$\overline{u}_{nn} = f_{nn}\overline{u}_{\max}, \tag{5.2}$$

where the fraction f_{nn} is a real number between 0 and 1. Applying Eq. (4.30) for the advective CFL-number, the prescribed face velocity is expressed as

$$\overline{u}_{nn} = f_{nn}\mathrm{CFL}_{\mathrm{adv}} M \frac{\Delta x_{\mathrm{w}}}{3\Delta t}, \tag{5.3}$$

where M is the 1D-resolution.

As presented in Sec. 4.5.3, the displacements are estimated by two distinct methods:

(1) The banking, which is applied to all 3DCV components but one, is to keep track of the residuals such that the prescribed displacement on average is matched.

(2) Continuity is enforced by calculating the remaining components from Eq. (4.17).

For the banking method, the Eqs. (4.11), (4.15) and (4.16) apply, and the jitter can be written as

$$w'_{nn} = \overline{u}_{nn} - w_{nn} = (\gamma_{nn} - \delta_{nn})\frac{\Delta x_{\mathrm{w}}}{3\Delta t} = r_{nn}\frac{\Delta x_{\mathrm{w}}}{3\Delta t}, \tag{5.4}$$

where γ_{nn} is the prescribed displacement. The jitter relative to the prescribed velocity for a particular face is by combining Eq. (5.3) and Eq. (5.4) given as

$$\frac{w'_{nn}}{\overline{u}_{nn}} = \frac{r_{nn}\frac{\Delta x_{\mathrm{w}}}{3\Delta t}}{f_{nn}\mathrm{CFL}_{\mathrm{adv}} M \frac{\Delta x_{\mathrm{w}}}{3\Delta t}} = \frac{r_{nn}}{f_{nn} M \mathrm{CFL}_{\mathrm{adv}}}. \tag{5.5}$$

This implies that the magnitude of the relative jitter is in inverse ratio to the 1D-resolution as well as the $\mathrm{CFL}_{\mathrm{adv}}$-number. Further, the face velocities that are small relative to the maximum velocity will have correspondingly high relative jitter.

If we consider the wafer velocity components that are calculated by the banking and assume no correction of the displacements, the jitter is always *less* than $\Delta x_{\mathrm{w}}/\Delta t$ because r_{nn} by construction is less than one. For these components, the jitter occurs on a time scale $\Delta t/(\gamma_{nn} - \delta_{f,nn})$.[1] The picture is, however, more complex for the components that are calculated by continuity. The deviation for these components is generally greater than $\Delta x_{\mathrm{w}}/\Delta t$, not only because it contains the sum of the respective deviations for that particular 3DCV, but also since deviations accumulate downstream due to the successive layer by layer calculation of displacements. As a result of the interconnection between deviations, the jitter of these components is in practice on a time scale similar to the advective time step.

When the displacements are corrected by the method suggested in chapter 4.5.4, the jitter for *all* components occurs on the order of the advective time scale, due to that the corrections generally are adjusting the components at every time step.

5.2.2 Characterization of the prescribed flow field

The velocity field applied to prescribe the displacements in LEM3D was based on the measurement of Tong and Warhaft (1995) in the self-similar region of a turbulent jet with nozzle diameter $D_j = 30\,\mathrm{mm}$ and jet exit velocity $U_j = 9\,\mathrm{m/s}$. According to Tong and Warhaft (1995) the mean centerline velocity decays as

$$U_c(x) = \frac{CU_j}{(x - x_{\mathrm{virt}})/D_j} \tag{5.6}$$

in the self-similar region of the jet, where U_c is the streamwise mean velocity on the centerline, $C = 6.13$ is a constant, and $x_{\mathrm{virt}} = 0$ is taken as the virtual origin of the jet. The virtual origin is defined as the x-position where the straight line $U_j/U_c(x)$ intercepts the x-axis. The lateral self-similar profiles of the streamwise velocity are to a good approximation Gaussian with a form

$$u_x(x, r) = U_c(x) \exp\left[-K_u \left(\frac{r}{x}\right)^2\right], \tag{5.7}$$

[1] If for instance γ_{nn}=1.1, which means that $\delta_{f,nn}$=1, δ_{nn} will alternate between 1 and 2 with a frequency of $(\gamma_{nn} - \delta_{f,nn})/\Delta t$=0.1/$\Delta t$ which corresponds to a time scale 10Δt.

where r is the radial distance from the jet centerline, and the constant $K_u = 75.2$, reported by Panchapakesan and Lumley (1993a) for several jet experiments in the range $Re_j \sim 11000 - 95000$, was assumed to fit the Tong and Warhaft data ($Re_j = 18000$). The lateral velocity components were determined from the continuity equation[2]

$$\frac{1}{r}\frac{\partial}{\partial r}(r u_r(x,r)) + \frac{\partial u_x(x,r)}{\partial x} = 0, \tag{5.8}$$

which was integrated over r to yield

$$u_r(x,r) = -\frac{1}{r}\int_0^r r' \frac{\partial u_x(x,r')}{\partial x}\partial r'. \tag{5.9}$$

Applying the boundary conditions $u_r[x,0] = 0$ determined $u_r(x,r)$.

The velocity components normal to the surface of a 3DCV were represented by the surface averaged velocities

$$\begin{aligned}
\overline{u}_x &= \frac{1}{\Delta z \Delta y}\int_z\int_y u_x(x,y,z)dydz,\\
\overline{u}_y &= \frac{1}{\Delta x \Delta z}\int_z\int_y u_y(x,y,z)dxdz,\\
\overline{u}_z &= \frac{1}{\Delta x \Delta y}\int_y\int_x u_z(x,y,x)dydx,
\end{aligned} \tag{5.10}$$

where the Cartesian components were calculated from the coordinate transformation from cylindrical coordinates

$$\begin{aligned}
u_x(x,y,z) &= u_x(x,r),\\
u_y(x,y,z) &= \frac{r}{y}u_r(x,r),\\
u_z(x,y,z) &= \frac{r}{z}u_r(x,r),
\end{aligned} \tag{5.11}$$

where $r = \sqrt{y^2+z^2}$. The analytical and numerical tool MATHEMATICA by Wolfram (1999) was used to evaluate the integral (5.9) analytically, and perform the integration of the expressions (5.10) numerically. The continuity error related to the numerical integration was negligible.

[2]Here given in cylindrical coordinates. Components and derivatives in θ-direction were not considered due to axis symmetry.

5.2.3 Numerical setup and data collection

LEM3D was run omitting the scalar transport by molecular diffusion, triplet map stirring and rotational coupling. For constant density, these processes are completely decoupled from the wafer displacements, and hence do not influence the present results. Referring to the simulation procedure in Sec. 4.10, the following steps were performed: The initial setup relevant to the advection, (2), and at each time step; the determination (3)(c) and possible correction (3)(d) of displacements, followed by the advection advancement (3)(e). Wafer velocity data were sampled as given below.

The upwind domain boundary was placed at $x/D_j = 6.3$. The various cases in Table 5.1 were motivated by investigating the importance of 1D- and 3D-resolution as well as $\mathrm{CFL_{adv}}$-number on the wafer velocity.

Table 5.1: Input data to the LEM3D simulations

Case	M	$\mathrm{CFL_{adv}}$	Δx [mm]	3D-resolution	δ_{th}
A1a	20	0.1	4	$50 \times 45 \times 45$	1
A1b	40	0.1	4	$50 \times 45 \times 45$	1
A1c	80	0.1	4	$50 \times 45 \times 45$	1
A1d	160	0.1	4	$50 \times 45 \times 45$	1
A1e	80	0.2	4	$50 \times 45 \times 45$	1
A1f	80	0.4	4	$50 \times 45 \times 45$	2
A1g	80	0.1	8	$26 \times 23 \times 23$	2
A1h	20	0.1	2	$100 \times 91 \times 91$	1

The mean wafer velocity was estimated by sampling the displacements at the 3DCV face by the expression

$$\overline{w}_{nn} = \left[\frac{1}{N_s} \sum_{j=1}^{N_s} \delta_{nn}^{j} \right] \frac{\Delta x_{\mathrm{w}}}{3\Delta t}, \tag{5.12}$$

where δ_{nn}^{j} is the total number of wafers displaced over the 3DCV face nn at time $t = t_j$, and N_s is the number of samples. The jitter was estimated by taking the rms of the deviation between the wafer velocity and the prescribed velocity

$$w_{nn}^{'} = \sqrt{\frac{1}{N_s - 1} \sum_{j=1}^{N_s - 1} \left(\delta_{nn}^{j} - \gamma_{nn}^{j} \right)^2} \frac{\Delta x_{\mathrm{w}}}{3\Delta t}. \tag{5.13}$$

The displacements were sampled at every time step.

5.2.4 Results and discussion

The following section investigates the effect of applying corrections and examines the validity of the proposed scaling of the jitter as given by Eq. (5.5).

Representation of mean wafer velocity

The banking was developed to ensure that the lateral wafer velocity components conform to the prescribed velocity on average. The streamwise components are determined from continuity. Hence, if the prescribed velocity field satisfies continuity, the mean wafer velocity field should conform to the prescribed field at all 3DCV faces. This was verified for all cases listed in Tab. 5.1. The correction algorithm was found to have no effect on the mean wafer velocity profiles.

Reducing deviations by discrete corrections

A method for correcting the discrete displacements was suggested in Chapter 4.5.4. The method involves a threshold δ_{th} which determines how "tightly" the system is controlled. Initial tests revealed that a somewhat higher threshold was needed in some of the cases to avoid accumulation of the residual, r_{nn}. The lowest possible threshold is reported in Tab. 5.1 for each case.

The square sum of deviations for a 3DCV was defined in Eq. (4.18). The maximum (of all 3DCVs in the domain) rms of deviations is further given by

$$d_{\max} = \max \sum_{nn}^{N_{\text{face}}} \sqrt{(r_{nn} + \Delta_{nn})^2}, \tag{5.14}$$

where Δ_{nn} is the integer correction for face nn.

In Fig. 5.1, $d_{\max}$ normalized by M is plotted as a function of time for two different simulations of A1d. Corrections were applied in subfigure (b), but omitted in subfigure (a). For subfigure (b), the maximum rms of deviations was sampled right before and immediately after the correction at every time step. The figure is further read as follows: After every new determination of displacements (step (3)(c) in the simulation procedure), $d_{\max}/M$ was at a level in between 0.2 and 0.4. Then after every correction (step (3)(d)), $d_{\max}$ dropped down to about 0.04. The maximum rms was generally reduced by a factor 5-10 by the corrections for this case. The amplitude of the *variation* in $d_{\max}$ was also reduced compared to subfigure (a) where corrections were omitted. The reason for the variation of $d_{\max}$ (before correction) with time seen in Fig. 5.1(b) was not further investigated.

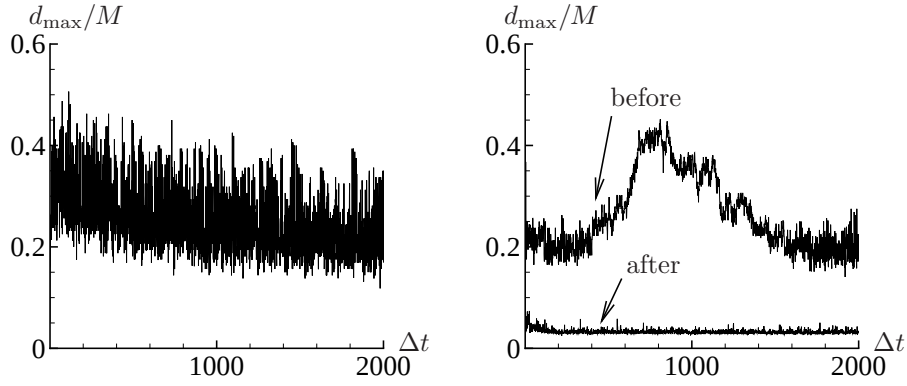

(a) No correction of displacements (b) Correction of displacements

Figure 5.1: The maximum rms of deviations normalized by the 3DCV resolution as a function of the first 2000 time steps. In (b) the deviation is plotted before and after corrections have been applied. M is 160 in both cases.

In Fig. 5.2, the jitter of the axial and radial displacement components are plotted for case A1d. The mean wafer velocity is also shown for reference. When the displacements were implemented without corrections, the jitter of the axial centerline velocity increased asymptotically downstream. With corrections, the jitter was significantly reduced to a level that apparently was independent of distance from the jet origin. The radial jitter component, however, was less affected by the corrections. This is due to that the axial displacement components, which were calculated by continuity (4.17), contained the deviations from the respective 3DCV face components. The potential for reduction was therefore larger for the axial components. Relative to the mean velocity component, the lateral jitter was on the order of 200%, whereas the streamwise component was approximately 5 to 10% after correction. This was due to the dependence of f_{nn} in Eq. (5.5). With a low f_{nn} there are fewer wafers available for adjustment to the prescribed velocity, which leads to a higher jitter relative to the local prescribed velocity.

Jitter sensitivity

From the expression (5.5) it follows that the jitter decreases with increasing 1D-resolution, $\mathrm{CFL}_{\mathrm{adv}}$-number and velocity factor f_{nn}. To assess the validity of this relationship, the present results were scaled by the factor

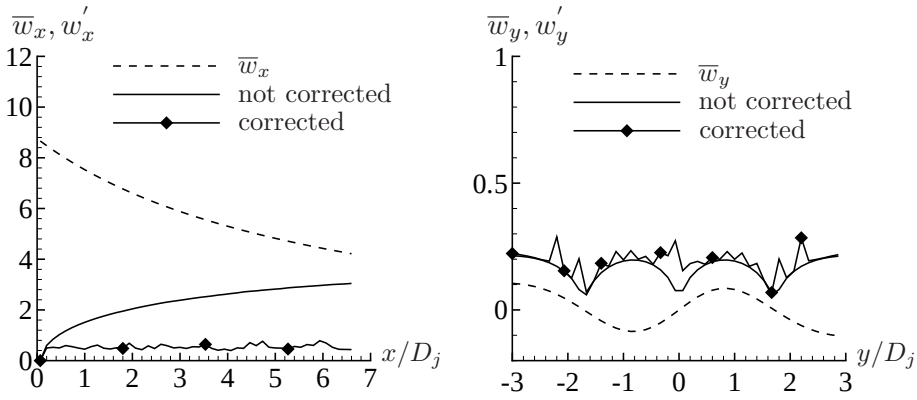

(a) (b)

Figure 5.2: (a): Jitter of the axial velocity component along the centerline, and (b): of the radial velocity component through the center of the jet at $x/D_j \sim 13$. Comparison of the jitter when displacement corrections are included or omitted for case A1d. The mean velocity is shown with a dashed line for reference.

$M\mathrm{CFL}_{\mathrm{adv}} f_{nn}$. Thus, the normalized jitter is defined as

$$w^*_{nn} \equiv w' M\mathrm{CFL}_{\mathrm{adv}} f_{nn}. \tag{5.15}$$

The scaled axial jitter profile along the centerline and the radial (y-directed) profile through the domain center at $x/D_j \sim 13$ are shown in Fig. 5.3. For all 1D-resolutions considered, the profiles overlapped to a good approximation.[3] This means that the jitter was reduced with increasing 1D-resolution as expected.

The presented scaling also seemed to agree well when the $\mathrm{CFL}_{\mathrm{adv}}$-number was varied as shown in Fig. 5.4(a). The somewhat higher level for $\mathrm{CFL}_{\mathrm{adv}} = 0.4$ was probably due to that the correction threshold was increased to $\delta_{\mathrm{th}} = 2$ in this case to avoid unbounded accumulated residuals.

In Fig. 5.4(b), the axial profile is plotted for various 3D-resolutions. The wafer thickness, Δx_{w}, was kept constant meaning that $M = 20$ for the domain with the finest 3D-resolution and $M = 80$ for the domain with the coarsest resolution. The profile shapes were approximately on the same level. This implies, since the jitter was scaled by M, that a refinement in 3D-resolution increased the jitter if not accompanied by a corresponding reduction in Δx_{w}.

[3]The deviations between the profiles in Fig. 5.3 and Fig. 5.4 were not further investigated.

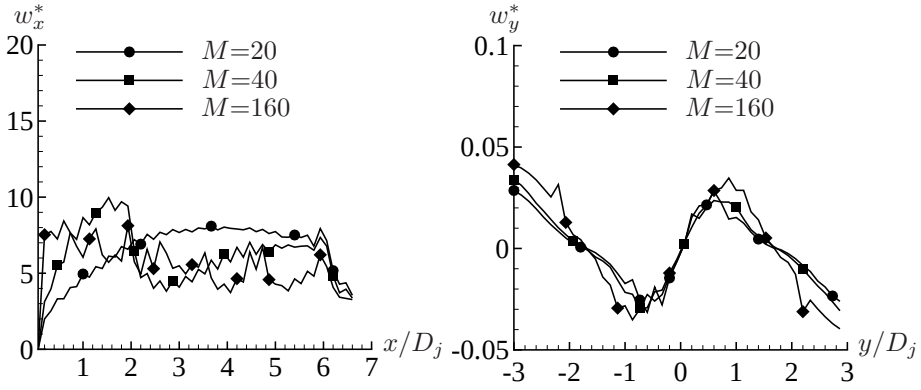

(a) Axial component along the jet centerline (b) Lateral profile through centerline at domain end

Figure 5.3: Normalized jitter of (a) the axial velocity component along the centerline and (b) the radial component in the lateral direction through the centerline at $x/D_j \sim 13$. Sensitivity to 1D-resolution.

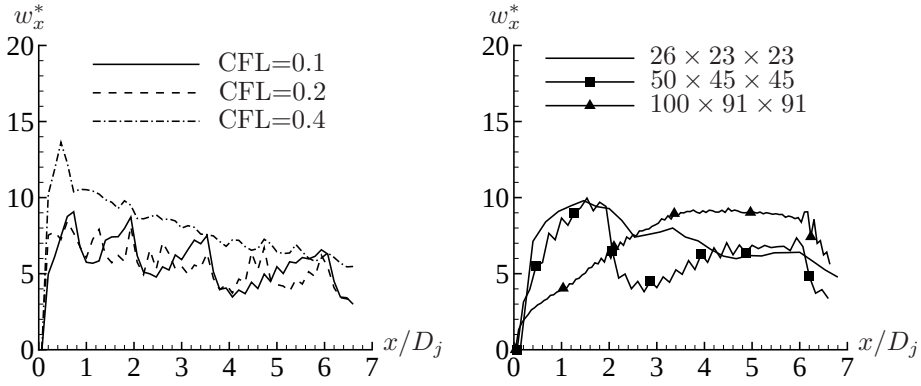

(a) Sensitivity to CFL-number (b) Sensitivity to 3D-resolution

Figure 5.4: Normalized jitter of the axial velocity component along the centerline. The sensitivity to CFL-number (a) and 3D-resolution (b). In (a), $M = 80$ for all cases, whereas in (b), $M = 20$, 40 or 80 depending on the 3D-resolution such that Δx_{w} was equal.

5.2.5 Summary

The results in this section are summarized as follows:

- In all cases considered, the wafer velocity equaled the prescribed mean velocity field on average.
- The jitter decreased with increasing 1D-resolution. This is due to that higher resolution provides more flexibility in representing the mean velocity by discrete displacements. For the current test cases, the decrease scaled close to linearly with M.
- Increasing the CFL-number also decreased the jitter. The reason is that the number of wafers (relative to the number of prescribed displacement) needed to adjust to the prescribed displacement is higher for larger $\mathrm{CFL}_{\mathrm{adv}}$-numbers.
- The jitter relative to the prescribed mean displacement was larger when the prescribed displacement was a small fraction of the maximum velocity, i.e., when f_{nn} was small.
- A coarse 3D-resolution with fine 1D-resolution has less jitter than a fine 3D-resolution with correspondingly coarser 1D-resolution.

5.3 Case A2: Displacement and travel time

5.3.1 Motivation and numerical setup

The isolated effect of random rotations on mean and rms travel time of a trace wafer through the domain was investigated by considering a single quasi 1D LEM domain. Contrary to a standalone 1D LEM domain, this one was also resolved by wafers on domains perpendicular to the main flow direction as shown in Fig 5.5, however, no transport processes occurred on these short domains. Triplet map stirring and molecular diffusion were omitted on all domains. The 3D-resolution was $M = 20$ and the $\mathrm{CFL}_{\mathrm{adv}}$-number 0.1 for all cases. The prescribed velocity field was uniform; hence the displacements were constant without any jitter.

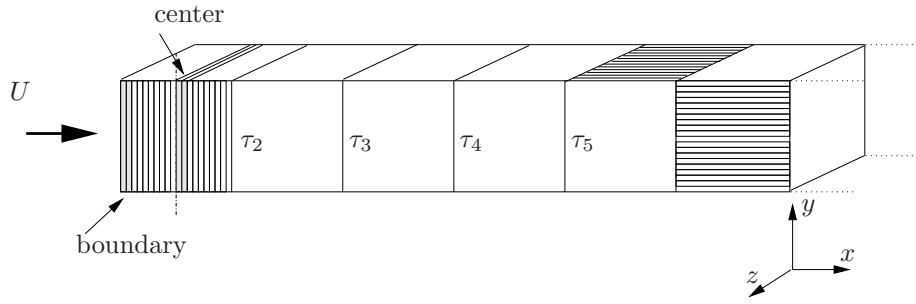

Figure 5.5: The setup for the quasi 1D LEM domain. The first, second last and last 3DCVs indicate that every 3DCV is resolved by wafers in the x-, y- and z-directions.

The present cases were primarily intended to serve as numerical tests. LEM3D is constructed as a turbulent mixing model, so one could argue that the present numerical test cases, omitting the triplet map stirring and molecular mixing, are somewhat out of scope. However, in situations where the triplet maps are infrequent relative to the random rotations, e.g. for relatively large integral scales, we may approach the ideal cases considered here. Besides this, the cases isolated the joint effect of random rotation and mean flow advection, enabling more transparent analyses.

5.3.2 Wafer paths through the domain

A random rotation sequence of a 3DCV will in this case first transfer a wafer located at X_l to one of the two transverse and inactive domains. Finally, when the wafer is rotated back to the active domain, it is either rotated in the same direction resulting in a net displacement of $|X_l - X_{(M+1-l)}|$,

or rotated in the opposite direction, putting it back at the position at X_l where it originally was located.

For infinite time, there are an infinite number of possible paths for a wafer through the computational domain. Let τ denote the travel time for a wafer through a 3DCV for a given realization. The wafer spends on average 1/3 of the time in each of the domain direction. Due to the random rotations, the travel time experienced by a trace wafer is sometimes greater and sometimes less than the prescribed travel time τ_{adv} defined in Eq. (4.31). The minimum travel time is defined as

$$\tau^{\min} \equiv \frac{\Delta x}{3U}, \tag{5.16}$$

which corresponds to streamwise travel without rotations to the lateral directions.

The various paths for a wafer through the 3DCV can in general be classified by three scenarios sorted by travel time:

(1) $\tau < \tau^{\min}$: The wafer is rotated through a random rotation sequence to the opposite side of the 3DCV to where it entered. This scenario, which is illustrated in Fig. 5.6(a), facilitates a *shortcut* through the domain. A location close to the boundary is necessary for taking such a shortcut.

(2) $\tau = \tau^{\min}$: If the wafer is displaced through the 3DCV without being subject to any rotations, the travel time will be 1/3 of the prescribed travel time.

(3) $\tau > \tau^{\min}$: Travel times above $\tau^{\min}$ is, for the present cases, mainly caused by the waiting time on the inactive domains. The travel time is, however, also increased when the wafer through numerous rotations and displacements is tossed back and forth in the 3DCV as shown in Fig. 5.6(b). The wafer will eventually escape this *trap*. It is intuitively evident that the probability of being trapped in this manner is higher when the wafer is located close to the center, than when it is located close to the boundaries. These two effects may cause travel times larger than the average prescribed travel time τ_{adv}.

The following sections investigate if the combined effects listed above gives $\tau = \tau_{\text{adv}}$ on average for the selected cases. The rms and probability distribution function (pdf) of travel times is also reported.

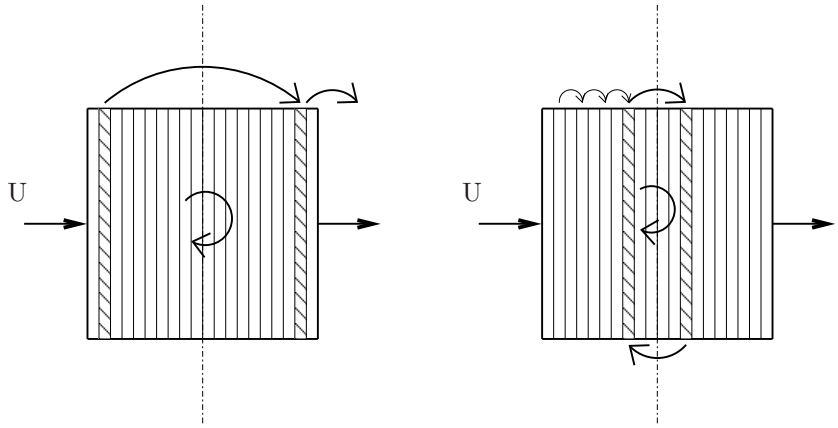

(a) Example of a shortcut, where $\tau < \tau^{\min}$

(b) Example of a trap, which may result in $\tau > \tau_{\text{adv}}$

Figure 5.6: Illustration of two different paths where (a) the travel time of a trace wafer is less than the minimum travel time, and (b) greater than the prescribed travel time.

5.3.3 Results of distribution in computational space

In this case the trace wafer was inserted in the center of the first 3DCV by randomly selecting one of the three domain directions with equal probability. Further, the simulations were evolved for a total time of $3\tau_{\text{adv}}$ corresponding to a displacement of $3\Delta x$. The average distance traveled was measured by letting a wafer that ended up in the second 3DCV be associated with a distance Δx, the third with a distance $2\Delta x$, the fourth with $3\Delta x$, and so forth.

The average distance traveled normalized the expected distance is given as a function of rotation frequency in Fig. 5.7(a). The average distance was correctly represented for relative rotation frequencies[4] up to about $\nu_r \sim 1$. For more frequent rotations, the average distance traveled was reduced. Since the wafer initially was located in the center of the 3DCV, it needed more time to escape as explained in Fig. 5.6(b). This resulted in reduced distance traveled.

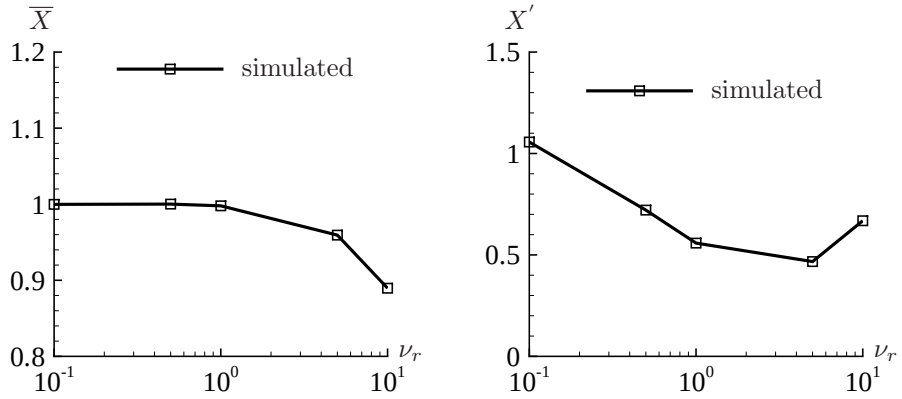

(a) Mean position (b) Rms position

Figure 5.7: Mean and rms of tracer wafer position as a function of the relative rotation frequency after $t = 3\tau_{\text{adv}}$.

The rms of the distance traveled normalized by its average is denoted X'. As shown in Fig. 5.7(b) the rms decreased for increasing rotation frequency, but increased again when the rotation frequency exceeded a frequency of about ∼3. This behavior is best explained by considering the pdf of travel distance given in Fig. 5.8. For low rotation frequencies, the wafer had a high probability of ending up on the domain where it initially was inserted,

[4]See Eq. (4.35) for the definition of relative rotation frequency.

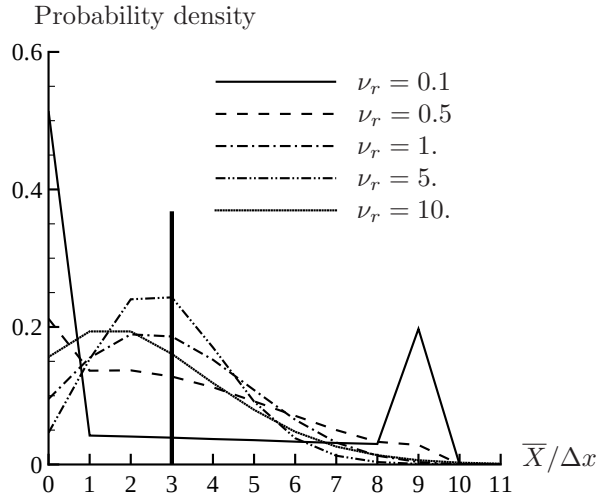

Figure 5.8: Distribution in computational space of the trace wafer after a simulation time of $3\tau_{\text{adv}}$. The pdf is given for a number of relative rotation frequencies from $\nu_r = 0.1$ to $\nu_r = 10$. The mean distance corresponding to the prescribed displacement is given by the thick line.

i.e., either at $\overline{X}/\Delta x = 0$ in one of the two inactive domains, or at $\overline{X}/\Delta x = 9$, which is three times the expected distance. With increasing rotation frequency, the double peak pdf approached a single peak. For even higher rotation frequencies, a left shift of the peak was observed, which was related to the reduction in mean travel distance as previously explained.

A relative rotation frequency on the order of one seemed to be the compromise that provided the correct average displacement without too much scattering. However, even though the wafer displacements were implemented deterministically, the pdf of the distance a wafer traveled was still rather wide. This is a direct consequence of the random rotations.

5.3.4 Travel time distribution results

The numerical experiment described in the present section is slightly different from the previous. The travel times were taken when the wafers crossed a 3DCV boundary in the streamwise direction. The travel time from when the wafer was inserted to when it crossed the upstream boundary of the second 3DCV is denoted τ_2, the third τ_3, and so forth (see Fig. 5.5). In the first set of experiments, the wafer was inserted at the upstream inlet of the first 3DCV, whereas the second set put the wafers in the 3DCV center

on the streamwise domain. Hence, the travel time from 3DCV boundary to boundary and from center to boundary was measured. The normalized mean travel time difference was given by

$$\tau_k^* = \frac{\overline{\tau}_k - k\tau_{\mathrm{adv}}}{\overline{\tau}_2}, \tag{5.17}$$

where $\overline{\tau}_k$ is the computed mean travel time at the upstream boundary of 3DCV number k. By the expression above, the travel time equals the expected when $\tau_k^* = 0$. The rms of the travel time normalized by the mean was estimated by

$$\tau_k^{'} = \frac{\sqrt{\overline{(\tau_k - k\tau_{\mathrm{adv}})^2}}}{\overline{\tau}_k}. \tag{5.18}$$

Travel time between 3DCV boundaries

In Fig. 5.9(a), τ_k^* is plotted for various travel times as a function of the rotation frequency. The figure shows that the expected travel time was achieved independent of rotation frequency. The normalized rms of the travel time as a function of rotation frequency is given in Fig. 5.9(b). For all travel times considered, the rms reached a minimum around $\nu_r \sim 3$.

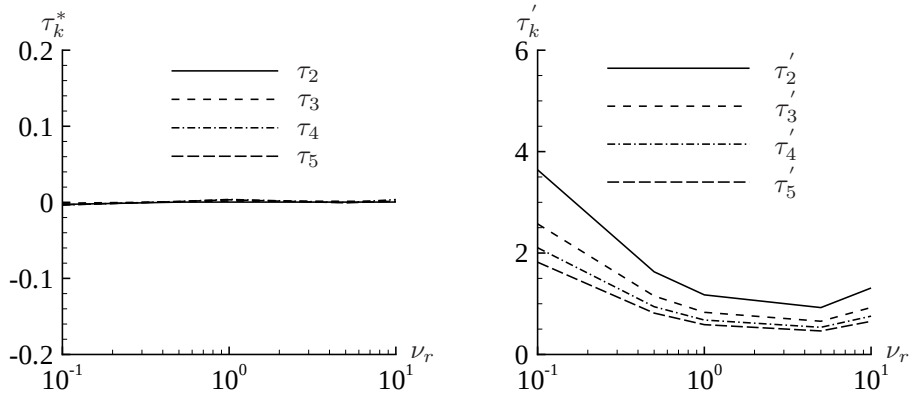

(a) Normalized mean travel time (b) Normalized rms travel time

Figure 5.9: Travel times for wafers that initially were inserted on the upstream boundary of the first 3DCV. The travel time was measured at the upstream 3DCV boundary for the second to the fifth 3DCV.

The pdf of travel times for various rotation frequencies is displayed in Fig. 5.10, where the vertical solid line indicates the travel time τ_{adv} corre-

sponding to the expected displacement and the vertical dashed line represents the minimum travel time, $\tau^{\min}$. Subfigure (a) shows the pdf of travel time to the upstream boundary of the second 3DCV, and subfigure (b) to the fifth 3DCV. For rotation frequencies on the order of one and less, there was a peak in the distribution at $\tau^{\min}$. The peak was due to that many wafers traveled through the domain without being subject to any rotations.[5] The peak in the pdf decreased for higher rotation frequencies and for increasing distances traveled as shown in Fig. 5.10. The probability of shortcuts, $\tau < \tau^{\min}$, increased with increasing rotation frequency.

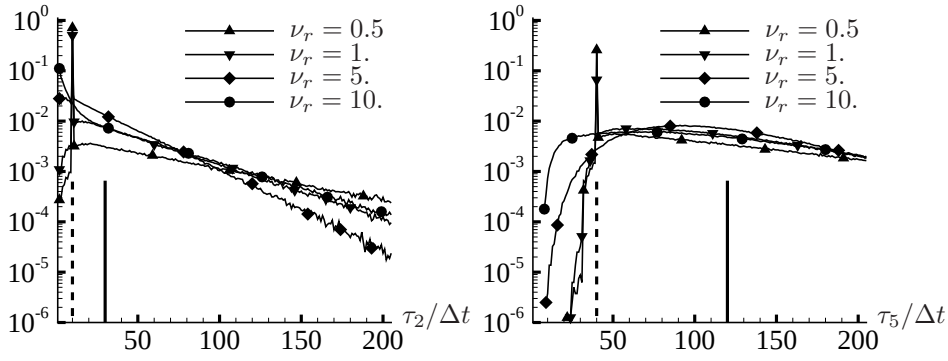

(a) Travel time to the fifth 3DCV (b) Travel time to the fifth 3DCV

Figure 5.10: Distribution of travel times for wafers that initially were inserted on the upstream boundary of first 3DCV. The vertical solid lines indicate the prescribed travel time τ_{adv} and the vertical dashed lines the minimum travel time $\tau^{\min}$.

[5]Note that all wafers were inserted in the first 3DCV in the *streamwise* oriented LEM domain.

Travel time between 3DCV center and boundary

In the set of numerical experiments described here, the wafers were inserted in the *center* of the first 3DCV in the streamwise direction (see Fig. 5.5). The deviation from the expected travel time increased exponentially with increasing rotation frequency as shown in Fig. 5.11(a). When the trace wafer was inserted in the center of the first 3DCV, it lacked the possibility of taking the shortcut through the 3DCV, and the possibility of being trapped was higher. Thus, the computed average travel time was significantly longer than the expected, and the travel time increased with increasing rotation frequency. Note that τ_k^* was almost the same for all k. This was because the deviation predominantly was due to the additional travel time in the first 3DCV.

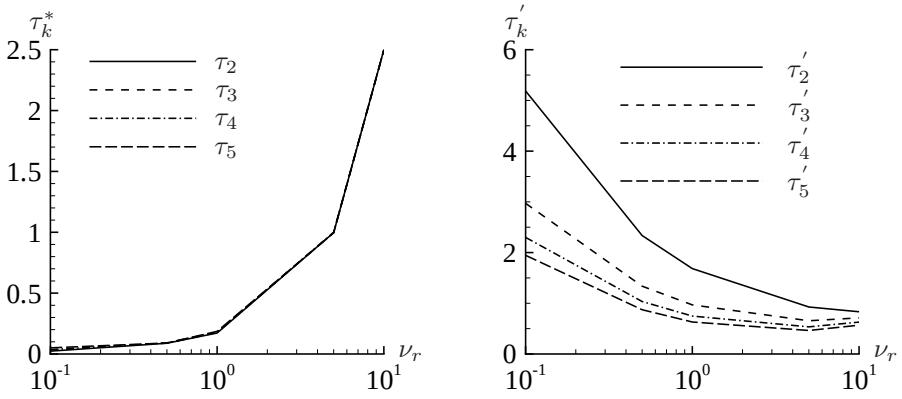

(a) Normalized mean travel time

(b) Normalized rms travel time

Figure 5.11: Travel times for wafers that initially were inserted in the center of the first 3DCV. The travel time was measured at the upstream 3DCV boundary for the second to the fifth 3DCV. The difference between expected, $\tau_k^* = 0$, and the simulated travel time increased with increasing rotation frequency.

The rms of the travel time scaled by the average travel time was reduced with increasing rotation frequency as shown in Fig. 5.11(b). This trend was opposite of the normalized mean travel time, which points out that the choice of rotation frequency in this case was a trade-off between matching the prescribed travel time or reducing the scattering in predicted travel time. The pdfs in Fig. 5.12 show similar behavior as Fig. 5.10 except for the fact that the probability of shortcuts through the first 3DCV (left of the dashed line) was zero, and hence also significantly less at the upstream boundary of the fifth 3DCV.

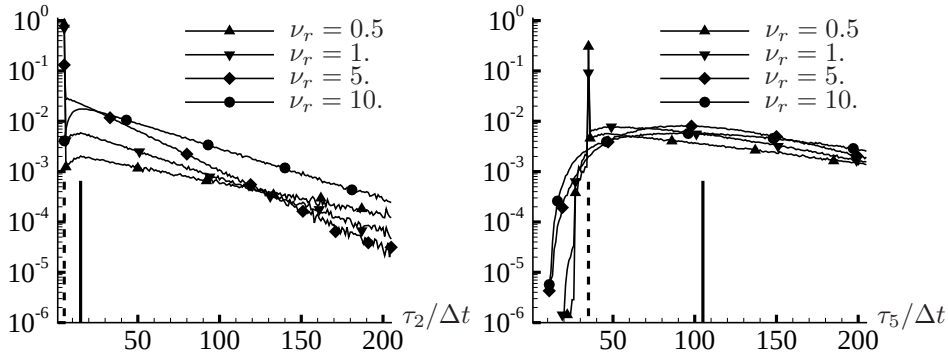

(a) Travel time to the second 3DCV (b) Travel time to the fifth 3DCV

Figure 5.12: Distribution of travel times for wafers that initially were inserted in the center of the first 3DCV. The vertical solid lines indicate the prescribed travel time τ_{adv} and the vertical dashed lines the minimum travel time $\tau^{\min}$.

5.3.5 Summary

In the first set of numerical experiments the displacements were measured at a 3DCV level. This means that we for instance did not distinguish between wafers that were located in the center and the wafers closer to the boundary. On this level of accuracy, the average travel distance was in accordance with the expected, as long as the rotation frequency was on the order of one or less. Higher rotation frequencies resulted in an increasing amount of wafers being trapped in the first 3DCV, whereas the rms of the travel distance increased for lower rotation frequencies.

The travel time predictions were performed by measuring the time exactly when the wafers were crossing the 3DCV boundaries. Hence, the local position of the wafer in the 3DCV was taken into account. The results revealed that the initial local position affects the travel time. Wafers located in the center of the 3DCV have a higher probability of being trapped, which gives a higher average travel time when we measure from center to the boundary. This effect increases with increasing rotation frequency. When we measured the travel time from boundary to boundary, we matched the average travel time for all rotation frequencies considered. However, the rms was relatively high, and the pdf had a clear peak around $\tau = \tau^{\min}$ for rotation frequencies $\nu_r \sim 1$.

We realize that the mean flow advection of wafers, as it is implemented in LEM3D, has random character due to the random rotations.

5.4 Brief discussion of implications for LEM3D

The overall conclusion is that the average travel time matches the prescribed time if we measure from boundary to boundary of the 3DCV or on a 3DCV basis. In Chapter 8 the wafer containing the passive scalar source, is located close to the 3DCV boundary, which should give the best representation of the mean scalar advection in the proximity of the source. However, as the results in this chapter show, the travel time distribution may still be rather broad. To what extent this affects the scalar statistics in LEM3D is uncertain and has not been further investigated. The "trapping" of the wafers in the 3DCV may affect the time for molecular mixing and chemical reaction to occur.

The implication of jitter of the wafer velocity components on the LEM3D results has not been thoroughly investigated. However, the results in Chapter 8 indicate that the effect of applying corrections, which affects the jitter as observed in Sec. 5.2.4, is negligible for the scalar mean and rms.

Chapter 6

Test cases B: Scalar mixing in isotropic turbulence

6.1 Introduction

In isotropic turbulence with uniform streamwise mean flow, no advective coupling by flipping of wafers is present in LEM3D. Hence, the only mechanism that exchanges scalars in between parallel and orthogonally oriented LEM domains is the auxiliary coupling by random rotation of 3DCVs. This chapter presents simulations that examined what the magnitude of the rotation frequency should be in order to provide sufficient directional coupling. The additional effects and artifacts introduced by the random rotations were also investigated. A rotation frequency on the order of one rotation per residence time seemed to provide sufficient coupling in most cases. However, this was dependent on the distance from the source. The results also indicate that the random rotations generally induce an additional dispersion and affect the variance and multi-point statistics.

The test cases were motivated by the need for examining the auxiliary coupling mechanism in a simplified setup. Hence, LEM2D, which only constitutes molecular mixing, triplet map stirring and random rotations, was utilized for the simulations.[1] Two cases were considered; the dispersion of a point source in non-decaying isotropic turbulence and the dispersion from a line source in grid turbulence. Except for the source configuration, the two cases differed mainly by the turbulence Reynolds number, which was about 6 times larger in the point source case. Results from simulations with LEM2D were compared to the standalone 1D LEM (denoted LEM1D), the

[1] The model is presented in Sec. 4.11.

analytical solution to the diffusion equation, and the model transport equations for scalar mean (3.8) and variance (3.10) solved by a finite volume method. The performance of the estimate for additional dispersion from random rotations, presented in Sec. 4.7.2, was also tested. For the line source case, the simulations with LEM1D and LEM2D were compared to measurements by Warhaft (1984).

6.2 Test case B1: Point source in isotropic turbulence

The present numerical experiment B1 was set up without a direct coupling to experiments per se. We considered an idealization of the grid turbulence case (Pope, 2000), where the velocity fluctuations downstream of the turbulence generating grid were maintained at a constant level by artificial forcing. The turbulence diffusivity field was uniform in time and space and given by $D_\mathrm{T} = 5.0 \times 10^{-3}\,\mathrm{m^2/s}$. The molecular diffusivity was $D_\mathrm{M} = 2.0 \times 10^{-5}\,\mathrm{m^2/s}$ giving a Peclet number of $Pe \equiv D_\mathrm{T}/D_\mathrm{M} = 250$.

6.2.1 Analytical solution to the scalar mean transport

The results from the numerical simulations were compared to the analytical solution to the linear one-dimensional partial differential diffusion equation principally given in Eq. (3.14). Given an initial point source of magnitude φ_0 at $y = 0$ on an infinite domain, it can be shown by basic calculus (Kreyszig, 1993) that the evolution of the scalar field is given by

$$\varphi(y,t) = C' \exp\left(\frac{-y^2}{2\sigma^2}\right), \tag{6.1}$$

where the prefactor C' reads

$$C' = \frac{\int \varphi_0 dy}{\sqrt{2\sigma\pi}}, \tag{6.2}$$

and $\sigma = \sigma(t)$ is the expected spreading. By applying the scaling in the turbulent diffusive regime given by Eq. (2.33), the equivalent analytical solution to spreading from a point source at $r = 0$ in two dimensions is

$$\varphi(r,t) = C \exp\left(-\frac{r^2}{4D_\mathrm{T}t}\right), \tag{6.3}$$

where the prefactor reads

$$C = \frac{\int \varphi_0 dA}{2\pi\sqrt{2D_{\mathrm{T}}t}}. \tag{6.4}$$

Due to the relatively high Peclet number, the molecular diffusivity was neglected in the expressions above. The mean scalar profiles from simulations with LEM1D and LEM2D were normalized by the factors $C^{'}$ and C, respectively, and in this manner compared to the correspondingly normalized analytical solutions denoted $\mathcal{A}^{'}$ for 1D and $\mathcal{A}$ for 2D.

6.2.2 Additional dispersion from random rotations

The estimate for additional dispersion from random rotations, presented in Sec. 4.7.2, was evaluated by comparing results from LEM2D with the analytical expression (6.3) and applying the adjusted prefactor given by

$$C_r = \frac{\int \varphi_0 dA}{2\pi\sqrt{2(D_{\mathrm{T}} + D_{\mathrm{r}})t}}, \tag{6.5}$$

where D_{r} is the additional diffusivity from rotations given in Eq. (4.39). The estimate is referred to in the figures by the symbol $\mathcal{A}_r$.

6.2.3 The finite volume method

The scalar variance results using LEM2D were also compared to the numerical solution to the transport equations of scalar mean (3.8) and variance (3.10). These equations were solved applying a finite volume method, in the following referred to as FV.

The convection-diffusion part of the equations were discretized by the power law scheme (Versteeg and Malalasekera, 1995). The two latter terms in the scalar variance equation (3.10), which respectively constitute the production and the dissipation of scalar variance, were implemented by adding them to the source term. The discretized equation system was solved sequentially by forward Gauss elimination and backward substitution, commonly denoted the Tridiagonal Matrix Algorithm (Ferziger and Peric, 2002).

The two transport equations were solved in *three dimensions* on a domain resolved by a uniform Cartesian mesh of $100 \times 25 \times 25$ control volumes (CVs) in the streamwise and lateral directions, respectively. For computational cost saving, the symmetry in the setup was utilized by resolving only one quadrant of the domain. Control volumes with side faces of 4 mm resolved the domain of $0.4\,\mathrm{m} \times 0.1\,\mathrm{m} \times 0.1\,\mathrm{m}$, which was sufficiently large to

provide negligible gradients on the boundaries. The point source was placed on the upstream corner of the grid boundary and was resolved by one control volume. Symmetry boundary conditions were applied on all lateral domains. The upstream boundary was a regular inflow boundary, where constant values for scalar mean and variance were specified, while the outflow boundary was treated as purely convective flux with zero streamwise gradients.

The numerical accuracy both in terms of approximating the point source and reducing numerical diffusion was assessed by doubling the number of control volumes on a domain of similar size. The discrepancies between the default and the finest grid were negligible.

The input values relevant to the FV computation are reported in Tab. 6.1. The turbulence energy k and its dissipation rate ε needed as input to the scalar dissipation term in Eq. (3.11) were given by the Eqs. (3.6) and (3.12) assuming a constant turbulence integral scale of 5.36 mm. The uniform distribution of k and ε corresponded to the LEM2D, which currently is limited to a single model integral scale. Assuming a uniform velocity field of $\overline{u} = 5\,\mathrm{m/s}$, the turbulence intensity was estimated to $I \equiv u^{'}/\overline{u} \sim 19.5\%$ by applying the definition of k.

Table 6.1: Input data to the FV computations.

Case	Resolution	Δx [mm]	l_t [mm]	k [$\mathrm{m^2/s^2}$]	ε [$\mathrm{m^2/s^2}$]	I
F1	100×25×25	4	5.36	1.42	51.9	19.5%

6.2.4 Numerical setup in LEM2D

The LEM2D domain, shown in Fig. 6.1, was oriented perpendicular to the streamwise direction and moved downstream with the mean flow from where the scalar was released. The elapsed time in the model corresponded to downstream position from the scalar release translated by $t = x/\overline{u}$. Input data and turbulence characteristics for the LEM2D simulations are given in Tab. 6.2. The domain was 0.18 m×0.18 m and 0.36 m×0.36 m for simulation times of 7 and 31 eddy turnover times, respectively. The 1D- and 2D-resolutions[2] are given in the table for the various cases.

In the standalone 1D LEM simulations of the line source experiment in Kerstein (1992b), the ratio L/l_t was set to match second order moments with data. It is neither expected that the same constant can be applied to the present point source case, nor that LEM2D should inherit the same

[2]The expression *2D-resolution* in LEM2D corresponds to 3D-resolution in LEM3D.

Table 6.2: Input data to the LEM2D simulations. Lengths are given in [mm] and time scales in [s].

Case	Res.	Δx	M	L	L_K	$\frac{L_\mathrm{K}^*}{L_\mathrm{K}}$	T_L	τ_t	t_end
B1a	45×45	4	20	30	0.23	10	0.18	0.0057	$7\tau_t$
B1b	91×91	4	20	30	0.23	10	0.18	0.0057	$31\tau_t$
B1c	45×45	4	20	10	0.077	31	0.02	0.00064	$63\tau_t$
B1d	45×45	4	20	60	0.46	5.2	0.72	0.023	$1.7\tau_t$
B1e	45×45	4	100	30	0.23	2.1	0.18	0.0057	$7\tau_t$

constant as LEM1D in comparison between the two models. Nevertheless, the constant was in the present case not adjusted, bearing in mind that a better match could have been achieved by calibration. Applying the ratio $L/l_t = 5.6$ and the integral scale $l_t = 5.36\,\mathrm{mm}$, the model integral scale was set to $L \approx 30\,\mathrm{mm}$. Simulations with larger (B1d) and smaller (B1e) factors were also performed with LEM2D.

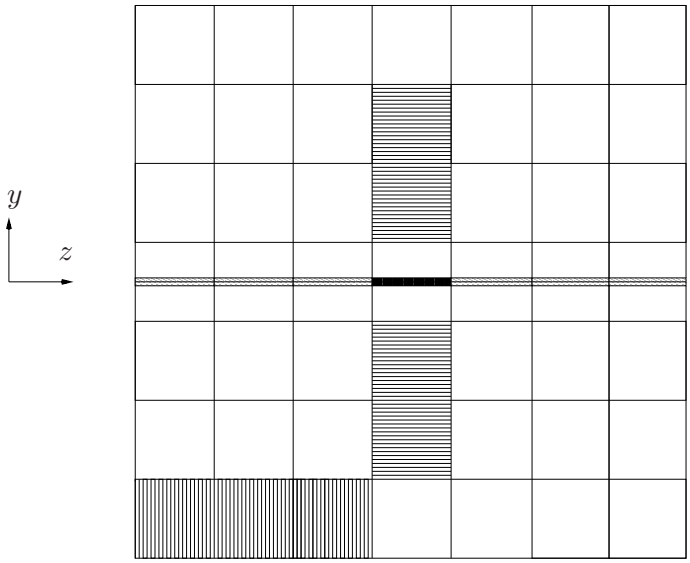

Figure 6.1: A schematic setup of the LEM2D domain, here exemplified by a 2D-resolution of 7×7 domain. The 1D-resolution in the y- and z-direction is indicated in some of the 2DCVs. In the point source case the two black y-oriented wafers in the center were initialized to φ_0 at $t = 0$. The shaded row of y-oriented wafers in the z-direction indicate the line source.

The eddy turnover time was estimated from $\tau_t = l_t^2/D_\mathrm{T}$, and the model

eddy turnover time by $T_L = L^2/D_{\mathrm{T}}$. The 2DCV size was set to 4 mm. The smallest possible triplet map was limited to 12 wafers ($k_{\min} = 4$). The model Reynolds number was $Re_S = 654$ by the relations and parameters given in Sec. 3.2.

The cases B1a and B1b under resolved the turbulence spectrum by a factor 10 (see Tab. 6.2). For the B1e case, the 1D-resolution was set to $M = 100$, which implied that the smallest implemented triplet map L^*_{K} was on the order of the model Kolmogorov scale. Some initial calculations were run in LEM1D to ensure that the 1D-resolution was adequate to represent mean scalar profiles for B1a-B1d. It was found that $M = 20$ was sufficient to capture the mean scalar values. In Figure 6.2, the mean scalar profile is compared to the expected spreading in the turbulent diffusive range for simulations from $t = 0$ to $t = 7\tau_t$ with LEM1D. The mean scalar profile from simulations with LEM1D was slightly less spread, which indicate that the mean profile was somewhat affected by the initial scaling (turbulent convective range) at this point.[3] For longer simulation times, corresponding to a position farther downstream, the mean scalar profile converged toward the Gaussian shape.

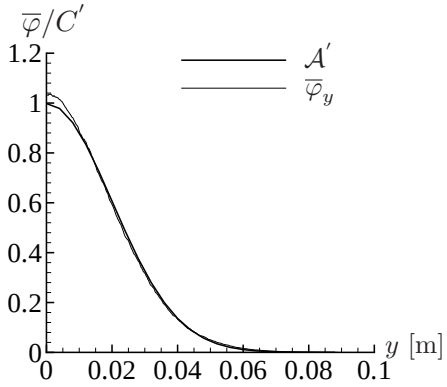

Figure 6.2: The mean scalar profiles from simulation with LEM1D from $t = 0$ to $t = 7\tau_t$. The simulation is compared with a Gaussian profile following the scaling in the turbulent diffusive range.

The LEM2D source configuration is given in Fig. 6.1. At time $t = 0$ a source of magnitude φ_0 was inserted in the two center wafers in the center 2DCV, as indicated by the black filled wafers in the figure. The source was inserted only in one of the two directions to fully assess if directional coupling was achieved.

[3]See Sec. 6.3 for more details on the scaling with LEM1D.

Data was taken after $t_{\text{end}} = 0.04\,\text{s}$ and $t_{\text{end}} = 0.18\,\text{s}$, which correspond to approximately $7\tau_t$ and $31\tau_t$, or $0.22T_L$ and T_L, respectively. Statistics were gathered as described in Sec. 4.9 by running 1000 realizations with different random number seeds. The number of realizations was adequate for achieving statistical convergence for the mean value and stabilizing the rms at a level with sufficient accuracy.

For the cases B1a, B1b and B1e the relative rotation frequency of the 2DCVs, ν_r, was varied to investigate the effect on the scalar mean and its variance and multipoint statistics. The relative rotation frequency was related to the turbulent diffusive time scale as defined by Eq. (4.48). The influence of integral scale on the mean scalar profiles was also investigated by comparison with LEM1D for the cases B1c and B1d.

6.2.5 Effect of random rotations on mean dispersion

The figures 6.3 and 6.4 show the 2DCV filtered[4] mean scalar profile through the center of the domain in the y-direction $\widehat{\varphi}_y$ and the radial profile $\widehat{\varphi}_r$ along a line 45° to the y- and z-direction. The data were sampled from the cases B1a and B1b. In the subfigures (a) to (d), the relative rotation frequency was varied from 0.1 to 2.0. The point source dispersion case is a symmetric case, hence coinciding $\widehat{\varphi}_y$- and $\widehat{\varphi}_r$-profiles signify sufficient directional coupling. It was shown that $\nu_r \geq 0.5$ provided adequate auxiliary coupling between the domains for this particular case, however, a higher rotation frequency was apparently needed closer to the source (Fig. 6.3) than further downstream (Fig. 6.4).

The additional dispersion from rotations increased with increasing rotation frequency. This trend is built into the estimate for additional dispersion from rotations, which is denoted $\mathcal{A}_r$ in the figures. The estimated additional dispersion was, however, somewhat larger at higher rotation frequencies than predicted by LEM2D. The results with LEM2D also indicated that the additional dispersion from rotations increased with increasing time from when the source was released. This time dependence is currently not embedded in the estimate.

In Fig. 6.5 the 1D-resolved mean scalar values along the LEM domains in the y- and z-direction, denoted by $\overline{\varphi}_y$ and $\overline{\varphi}_z$ respectively, are presented for case B1a. Increasingly wavy behavior was observed with increasing rotation frequency. This is explained by the following reasoning. In a non-uniform scalar field, the rotations introduce a sharp gradient on the boundary be-

[4] 2DCV filtered mean was sampled by Eqs. (4.45) and (4.46), where the x-direction was omitted in the latter expression.

tween 2DCVs. This sharp gradient is smoothed out by triplet map stirring and molecular diffusion. If the frequency of the triplet map stirring and molecular diffusivity is low relative to the rotation frequency, the mean scalar profiles will be imprinted by the sharp gradients.

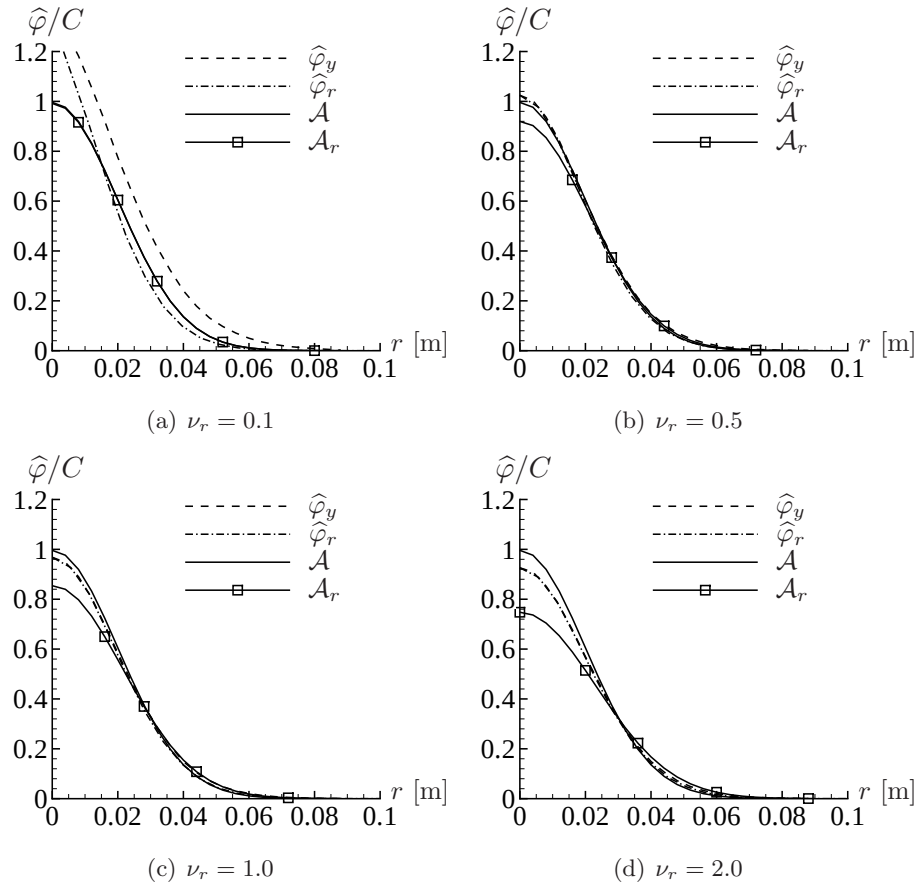

(a) $\nu_r = 0.1$

(b) $\nu_r = 0.5$

(c) $\nu_r = 1.0$

(d) $\nu_r = 2.0$

Figure 6.3: Comparison of mean 2DCV filtered scalar profiles along radial lines through the center for relative rotation frequencies ranging from 0.1 to 2. The results from simulations with LEM2D for the case B1a ($t_{\text{end}} = 7\tau_t$) are compared to the analytical solution, $\mathcal{A}$, and the analytical solution where the estimate for diffusivity from rotations is subtracted, $\mathcal{A}_r$.

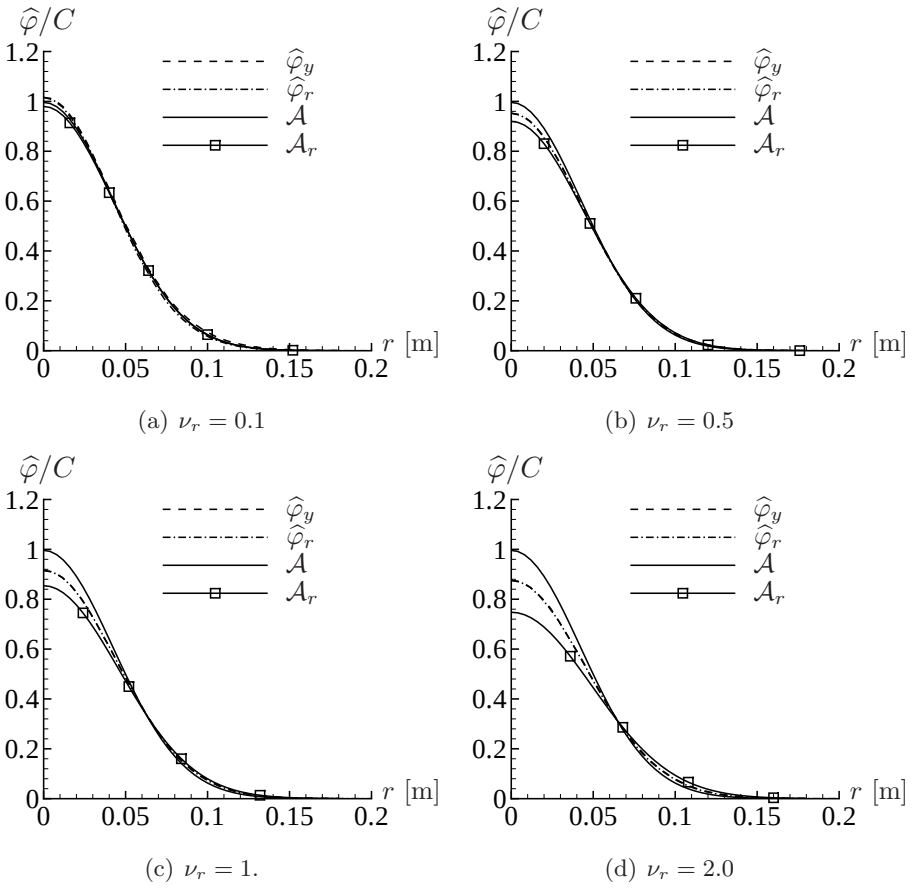

(a) $\nu_r = 0.1$

(b) $\nu_r = 0.5$

(c) $\nu_r = 1.$

(d) $\nu_r = 2.0$

Figure 6.4: Comparison of mean 2DCV filtered scalar profiles along radial lines through the center for relative rotation frequencies ranging from 0.1 to 2. The results from simulations with LEM2D for the case B1b ($t_{\text{end}} = 31\tau_t$) are compared to the analytical solution, $\mathcal{A}$, and the analytical solution where the estimate for diffusivity from rotations is subtracted, $\mathcal{A}_r$.

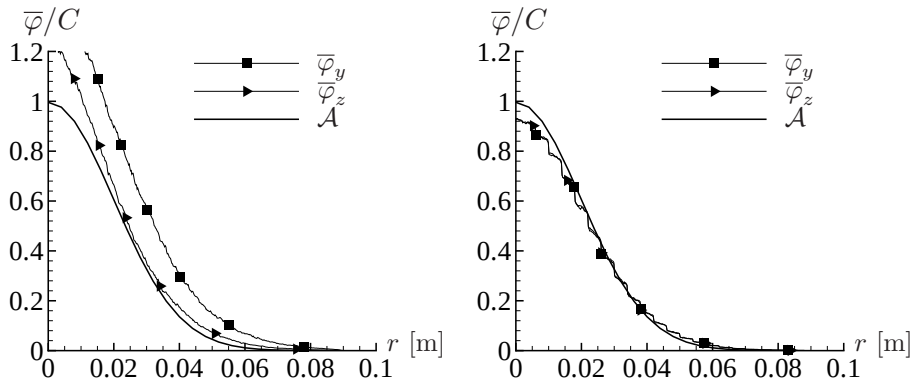

(a) $\nu_r = 0.1$ (b) $\nu_r = 2.0$

Figure 6.5: Comparison of mean 1D-resolved scalar profiles along center domains in the y- and z-direction for relative rotation frequencies of 0.1 and 2. The results from simulations with LEM2D for the case B1a are compared to the analytical solution, $\mathcal{A}$.

6.2.6 Effect of model integral scale on mean dispersion

Uniform spreading of a scalar is jointly dependent on the characteristics of the processes on the individual LEM domains and the auxiliary coupling by random rotations. For instance, the random rotations are unable to spread the scalar diagonally unless they operate in conjunction with the LEM processes, where the random triplet map events dominate in this respect. The relative rotation frequency was set to $\nu_r = 0.5$ for the simulations presented in this section.

It can be shown from the expression (4.5), that the event frequency increases by a factor $\sim$5 when the integral scale is reduced from $L = 30\,\mathrm{mm}$ to $L = 10\,\mathrm{mm}$. Correspondingly, increasing the integral scale from $L = 30\,\mathrm{mm}$ to $L = 60\,\mathrm{mm}$ decreases the event frequency by a factor $\sim$2.6. The effect of the model integral scale variations on the LEM2D-simulations is in Figure 6.6 compared to corresponding simulations with LEM1D. All simulations consisted of 1000 realizations to $t = 0.04\,\mathrm{s}$. The scalar in LEM1D was less spread for $L = 60\,\mathrm{mm}$ than the "expected" turbulent diffusive scaling. This can be explained by insufficient coupling and the initial scaling of LEM (see Sec. 6.3 for more details on LEM1D scaling). Increasing the integral scale in LEM2D resulted in larger discrepancies between the $\widehat{\varphi}_x$- and $\widehat{\varphi}_r$-profiles which indicated poorer coupling between the domains. This confirmed that the LEM processes play an important role in the coupling of the domains.

As the model integral scale was reduced, the LEM1D approached the Gaussian profile and the scaling in the turbulent diffusive regime. For LEM2D the profiles were more spread due to the additional dispersion from the random 2DCV rotations. Comparing Figs. 6.3(b) and 6.6, the results with $L = 10\,\mathrm{mm}$ gave the closest agreement with the estimated additional dispersion.

By scaling the time by the eddy turnover time, as given in Tab. 6.2, we may combine the effect of the integral scale variation and the time from when the source was released. I.e., the degree of coupling and the additional dispersion from rotations are dependent on the time, normalized by the eddy turnover time, from when the source is released. This aspect is, at present, not represented in the estimate for additional dispersion from the rotations presented in Sec. 4.7.2.

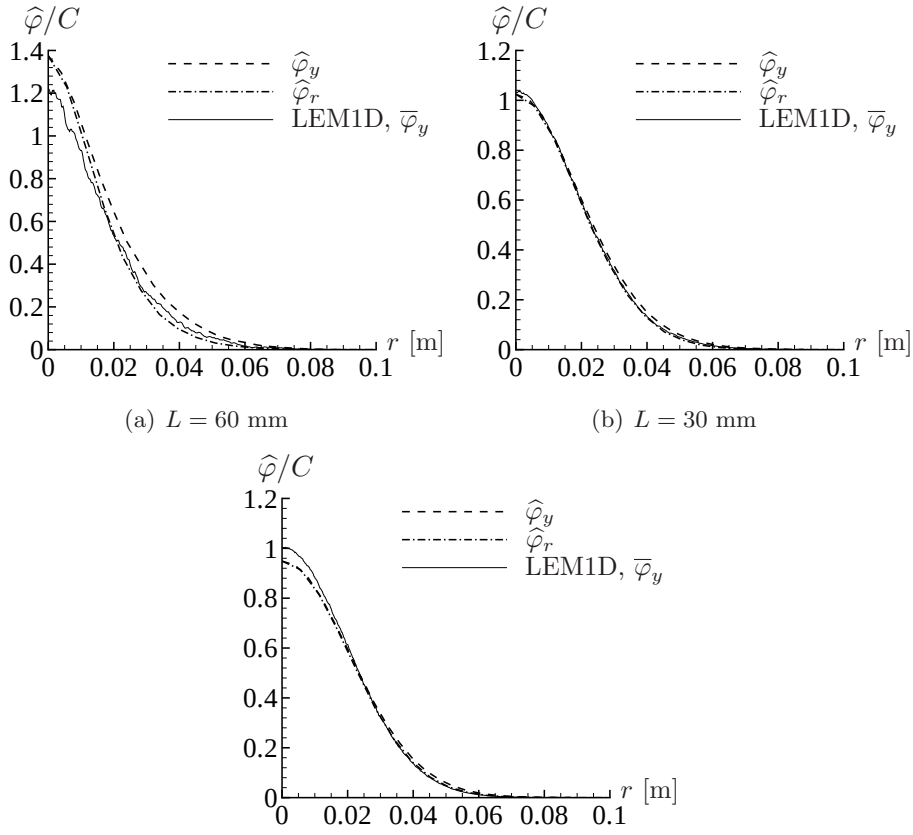

(a) $L = 60$ mm

(b) $L = 30$ mm

(c) $L = 10$ mm

Figure 6.6: Mean 2DCV filtered scalar profiles along radial lines through the center for simulations with different model integral scales (B1a, B1c and B1d). The results are also compared to simulations with LEM1D. For all LEM2D cases the relative rotation frequency was $\nu_r = 0.5$.

6.2.7 Effect of rotations on variance and autocorrelation

The 2DCV rotations will bring wafers on the interfaces between 2DCVs that originally were separated in proximity to each other. This may enhance the mixing and influence the scalar statistics. The effect of random rotations on the variance and the autocorrelation was investigated by running case B1e with different rotation frequencies. All simulations consisted of 1000 realizations to $t = 7\tau_t$. The simulations in Sec 6.2.5 showed that a relative frequency of rotations of $\nu_r = 0.5$ was necessary to ensure coupling between the domains. Hence, the present variation in rotation frequency excluded frequencies below 0.5.

In Figure 6.7, the scalar rms scaled by the centerline mean and a common reference is plotted as a function of radial distance in units of 2DCVs. The levels of the rms profiles were reduced, compared to LEM1D, by factors of approximately 1.4 to 1.8 for relative rotation frequencies of $\nu_r = 0.5$ to $\nu_r = 2$. If the rms results were scaled by a common reference value instead of the centerline mean, the reduction was somewhat larger as shown in Fig. 6.7(b). These results indicate that the random rotations of 2DCVs reduce the scalar variance.

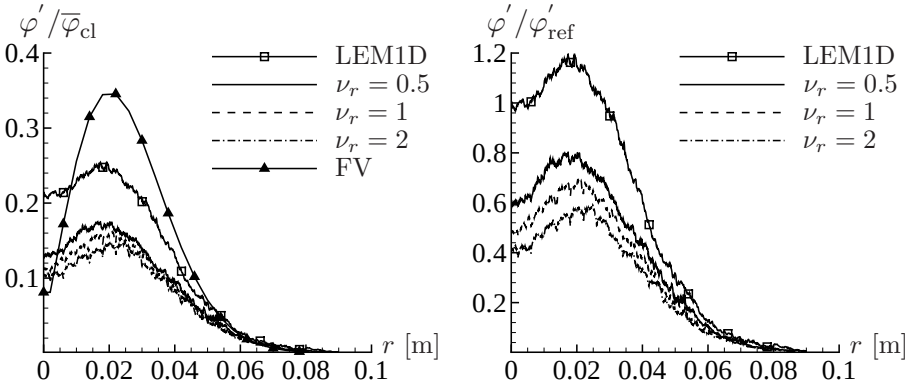

(a) Rms scaled by the center mean (b) Rms scaled by a common reference

Figure 6.7: Results from simulations with LEM2D and LEM1D at a downstream position corresponding to $t = 7\tau_t$. Radial profiles through the center for (a) rms scaled by the corresponding mean centerline value and (b) rms scaled by a common reference. In (a) the simulations are also compared to computations of scalar variance with FV.

The off-axis peak in the scalar rms profile from the FV computation was somewhat higher than the LEM simulations. The scalar rms computed by the FV is directly proportional to the integral scale in the model. Hence,

better match could have been achieved by tuning the factor between the integral scale applied in FV and the model integral scale in LEM2D and LEM1D. However, the shape of the profile differed and the FV rms declined more rapidly toward the centerline compared to the LEM simulations.

The autocorrelation given by Eq. (4.43) is the correlation between the scalar process at two different locations. Positive correlation represents realizations where the scalar deviation from the mean value is positive at the two positions, whereas negative autocorrelation represents realizations when the deviations have opposite signs. In Fig. 6.8 the autocorrelations between the scalar value for the center wafer at $y = 0$ and the respective wafers along the same LEM-domain are given at $t = 7\tau_t$. A triplet map can completely displace a scalar a distance from the center where it originally was located. This instance results in negative autocorrelation. The standalone LEM1D gave a negative autocorrelation in the range $r \approx 0.015\,\mathrm{m}$ to $0.06\,\mathrm{m}$, which is about 0.5 to $2L$. For LEM2D the negative autocorrelation was reduced in value as well as in range. A plausible explanation is that the initially negative autocorrelation provided by the triplet map was reduced by the additional dispersion caused by the random rotation. Contrary to the rms results, the autocorrelation appeared to be close to independent of the rotation frequencies considered.

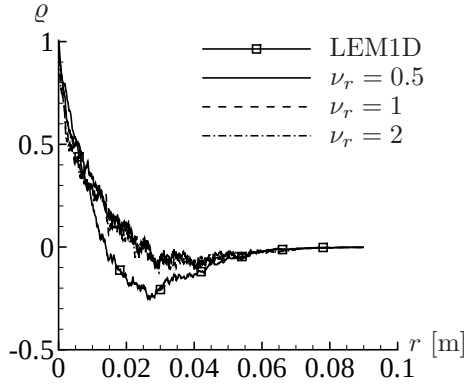

Figure 6.8: Autocorrelation between scalar value at $r = 0$ and r computed with LEM2D for various rotation frequencies compared with LEM1D for reference. Data was sampled after $t = 7\tau_t$.

6.3 Test case B2: The line source experiment

One of the simplest experiments for studying turbulent dispersion is the thermal wake behind a heated wire in isotropic grid turbulence (Pope, 2000). The three plume growth regimes briefly presented in Sec. 2.5.2 are observed for instance in the experimental work of Warhaft (1984). A short review of the analytical, modeling and experimental work is given in Viswanathan and Pope (2008). They use a PDF method with the IECM[5] mixing model to calculate the line source experiment. Kerstein (1992b) shows that the standalone 1D LEM is able to capture the trend of the three regimes. However, the transition points differ from the experiment, and the scaling exponent in the turbulent convective range is 1.5 times larger. The latter is due to the instantaneous nature of the triplet maps.

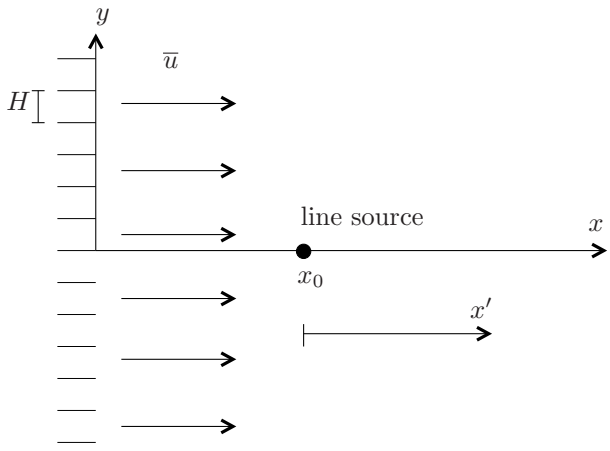

Figure 6.9: The schematic experimental setup of Warhaft (1984). The line source is located a distance x_0 from the turbulence generating grid. The figure is not to scale.

6.3.1 Experimental configuration

The schematic setup of Warhaft (1984) is illustrated in Fig. 6.9. The turbulence generating grid with width $H = 25\,\text{mm}$ is placed in a wind tunnel, which is $170\,H$ long and $16\,H \times 16\,H$ in cross section. The line sources are heated wires of diameter 0.127 mm and 0.207 mm for the near field and the far field experiments, respectively. The line source is placed a distance

[5]Interaction by Exchange with the Conditional Mean. The scalar mean is conditioned on velocity.

$x_0 = 52\,H$ from the turbulence generating grid.[6] The temperature of the wire is slightly higher than the ambient air, so the effect of buoyancy can be neglected and temperature can be considered a passive scalar. The turbulence diffusivity is $D_{\mathrm{T}} = 8.89 \times 10^{-4}\,\mathrm{m^2/s}$ and the molecular diffusivity $D_{\mathrm{M}} = 2.0 \times 10^{-5}\,\mathrm{m^2/s}$ giving a Peclet number of $Pe = 44.5$. The integral scale is reported to be $l_t = 1.35\,H$. To a good approximation, these properties are constant within the distance to the source considered here (Kerstein, 1992b).

6.3.2 Numerical setup in LEM2D

The LEM2D domain displayed in Fig. 6.1 was oriented perpendicular to the x-axis in Figure 6.9 and moved downstream with the mean flow velocity of $\overline{u} = 7\,\mathrm{m/s}$. Time in the model was translated to distance from the line source by $x' = \overline{u}t$, where $x' = x - x_0$. The domain of size $0.425\,\mathrm{m} \times 0.425\,\mathrm{m}$ was resolved as given in Tab. 6.3, where also input data and the derived turbulence characteristics are listed. The size of the 2DCVs was set equal to the spacing H between the turbulence generating grid in the experiment. The 1D-resolution provided a viscous cutoff on the order of the model Kolmogorov scale.

Table 6.3: Input data to the LEM2D simulations. Length scales are given in [mm] and time scales in [s]. See the text for further explanation.

Case	Res.	Δx	M	L	Re_S	L_{K}	$L^*_{\mathrm{K}}/L_{\mathrm{K}}$	T_L	τ_t
B2a	17×17	25	80	75.6	116	2.1	1.8	6.4	0.21

The line source was set by initializing the center y-oriented wafers in adjacent 2DCVs along the center z-direction to φ^0 at $t = 0$, as shown in Fig. 6.1. In this way, the extent of the line source in the y-direction was initially $\Delta x_{\mathrm{w}} = 0.31\,\mathrm{mm}$. However, a rotation of a 2DCV occurring early in the time evolution transfered the continuous line source to an intermittent pattern with an extent in the y-direction of Δx.

Cyclic boundary conditions were applied for the z-oriented domains. The simulations where run to $t = 0.52\tau_t$ and $t = 1.74\tau_t$, which corresponded to downstream positions at $x'/H = 30$ and $x'/H = 100$, respectively. 40000 realizations were needed to reduce statistical inaccuracies. Data were collected closer to the source in terms of eddy turnover time compared to the point source case in the previous section, and a somewhat higher relative

[6] A number of different distances are considered in the experiments.

rotation frequency, $\nu_r = 2$, was needed for sufficient directional coupling in this case.

6.3.3 Results

The results for mean scalar spreading are summarized in Table 6.4. The half-width is the distance y from the centerline at which the mean scalar value is half its centerline value. The LEM1D results were somewhat less spread than the experimental data, especially at $x'/H = 30$.[7] The agreement between LEM2D and the experimental data was better, which most likely was due to the additional spreading introduced by the random rotations. Hence, the good agreement between LEM2D and experimental data at $x'/H = 30$ and 100 must be considered fairly fortuitous. The lateral mean profiles from LEM2D simulations are shown in Fig. 6.10. The wavy behavior observed in the mean profiles at $x'/H = 100$ is believed to be a result of the random rotations and the rather coarse 2D-resolution (see the discussion in Sec. 6.2.5).

Table 6.4: Data for half-widths of the transverse mean scalar profile. The values are given in units of grid length, H.

Data at	Warhaft (1984)	LEM1D	LEM2D
x'/H=30	0.54	0.15	0.49
x'/H=100	1.1	0.91	1.1-1.2

The scalar rms results normalized by the centerline mean value is compared to experimental data at $x'/H = 30$ and $x'/H = 100$ in Fig. 6.11. The LEM2D simulations exhibited better match with experimental data at $x'/H = 30$, but this was mainly due to the better match with the mean value, by which the rms was scaled. The differences between the simulations with LEM1D and LEM2D were less apparent further downstream. When considering the rms scaled by a common reference, the level of fluctuations was slightly reduced from LEM1D to LEM2D. As shown, especially in Fig. 6.11(d), the rms was reduced with increasing rotation frequency. The same trend was also observed for the point source case in Sec. 6.2.7.

Fig. 6.12 displays the autocorrelation along the center y-oriented LEM domain at $x'/H = 30$ and $x'/H = 100$. The negative autocorrelation was significantly reduced from LEM1D to LEM2D. This is most likely due to the random rotations that smear out the negative correlation instances caused

[7] The results from simulations with LEM1D were in accordance with results presented in Kerstein (1992b).

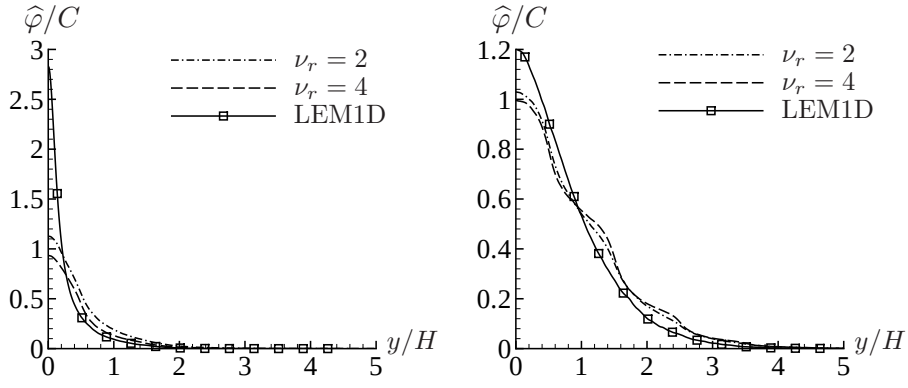

(a) $x^{'}/H = 30$ (b) $x^{'}/H = 100$

Figure 6.10: Comparison of center radial mean scalar profiles scaled by the prefactor, C, defined in Eq. (6.4) from simulations with the standard LEM and LEM2D with two different rotation frequencies. The values plotted are the ensemble averaged 3DCV filtered scalar values.

by the triplet map stirring. Similar behavior was observed in Sec. 6.2.7. The autocorrelation sensitivity to rotation frequency was insignificant in the cases considered.

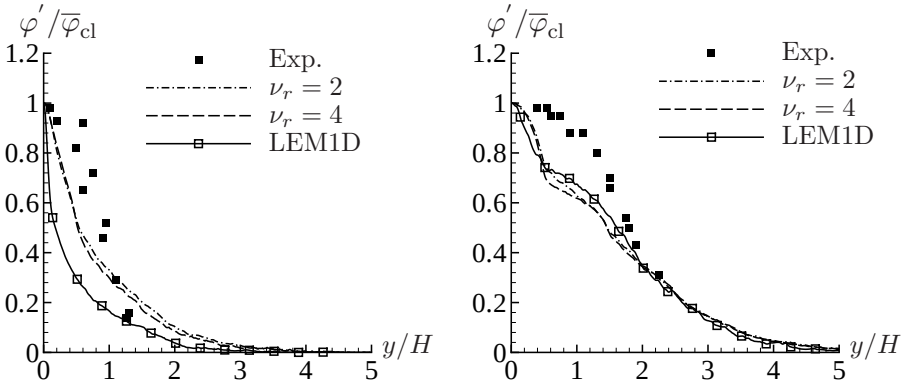

(a) $x'/H = 30$, Rms scaled by the center mean

(b) $x'/H = 100$, Rms scaled by the center mean

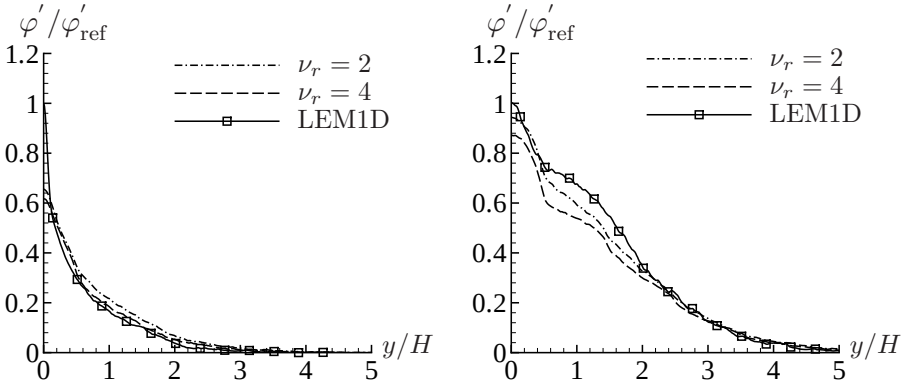

(c) $x'/H = 30$, Rms scaled by a common reference

(d) $x'/H = 100$, Rms scaled by a common reference

Figure 6.11: Rms results from simulations with LEM1D and LEM2D with two different rotation frequencies. Radial profiles along the center y-oriented LEM domain for (a,b) rms scaled by the corresponding mean centerline value and (c,d) rms scaled by a common reference.

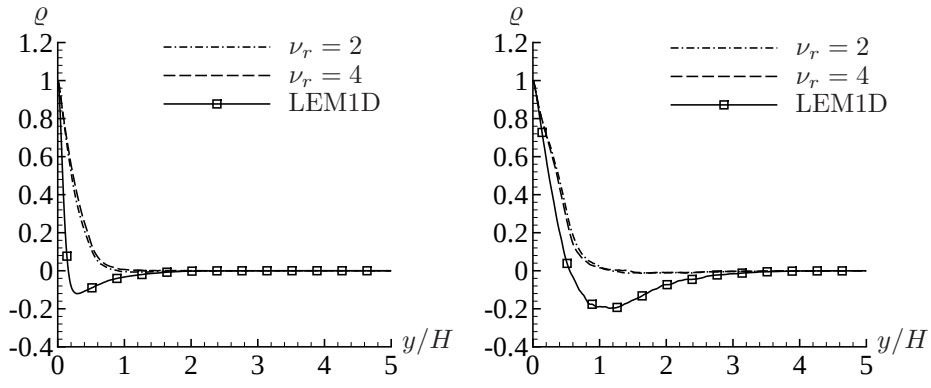

(a) $x^{'}/H = 30$ (b) $x^{'}/H = 100$

Figure 6.12: Autocorrelation results from simulations with LEM1D and LEM2D with two different rotation frequencies. Radial profiles along the center y-oriented LEM domain.

6.4 Discussion and summary

The auxiliary coupling by random rotations of 2DCVs with a relative frequency on the order of $\nu_r \sim 1$ seemed to provide sufficient directional coupling between LEM domains. A higher frequency was needed closer to the source than farther downstream. The preliminary conclusion from the present results is that it appears to be a window of operation for the relative rotation frequency which yields reasonable results. Infrequent rotations result in poor coupling of LEM domains, whereas too frequent rotations results in significant additional dispersion and mixing.

The results show that the auxiliary coupling by random rotations increase the mean dispersion of scalars. The proposed estimate for the additional dispersion provides an adequate representation. A strategy suggested by Kerstein *et al.* (2007) is to subtract the estimated diffusivity from rotations from the physical turbulence diffusivity. Further work is, however, needed in order to establish a function that better matches the additional dispersion from rotations and include the dependencies of time, normalized by the eddy turnover time, from the scalar source.

The scalar rms and negative autocorrelation were generally less in results from LEM2D compared to LEM1D with corresponding input. The main difference between LEM1D and LEM2D was the random rotations, and we believe that they were the main cause of the discrepancies between the models. This may be due to enhanced mixing of wafers that are brought in proximity to each other by the rotations. The reduction in rms can be moderated by increasing the factor between the physical and model integral scale. This kind of tuning has previously been applied to LEM1D.

Chapter 7

Test case C: Thermal expansion

7.1 Introduction

This chapter presents a numerical test case of the reacting LEM3D. The reacting LEM3D includes discrete dilatations from heat release and coupling to a flow solver as presented in Sections 4.3.3 and 4.5. Results from a test case with an imposed expansion rate are given. The suggested expansion algorithm is the first attempt to include dilatations from heat release in LEM3D. It is revealed that this early version has some artifacts that must be altered for consistent representation of the mass fluxes. A few alternative strategies are briefly presented and discussed.

7.2 Numerical setup

7.2.1 The coupled RANS-LEM3D model

A reduced version of LEM3D, omitting turbulent stirring and molecular mixing, was applied in the present study. Density was the only property transported with the wafers. Expansion events were determined by randomly sampling the wafers to be expanded from a distribution. The statistically stationary density field from the LEM3D simulation was further fed to RANS. Furthermore, the mass, momentum and turbulence model transport equations in RANS were solved with density input from LEM3D. The RANS computation provided the updated velocity field for the LEM3D simulations, as principally explained in Fig. 4.5.

A one-to-one correspondence between the control volumes in RANS and

the 3DCVs in LEM3D was assumed. Hence, we refer to 3DCVs and 3D-resolution also for RANS in the following. The RANS-LEM3D model was run with two-way coupling between the models (see Sec. 4.4).

The test case was run with two different 3D-resolutions as given in Tab. 7.1. For LEM3D, the 1D-resolution was correspondingly reduced with refinement in 3D-resolution to maintain a constant wafer thickness for both cases.

The expansion events were randomly implemented by sampling from a distribution. We applied a distribution, such that the probability of expansion was given as a uniform prescribed expansion rate in the expansion zone, while it was zero elsewhere. The expansion zone was defined by a *cube* as indicated in Fig. 7.1 on page 117. During grid refinement, the domain size and the expansion zone size were kept constant, so they were resolved by a triple amount of 3DCVs to maintain the symmetry in the setup.

Table 7.1: Input data to the simulations. "Exp. res." is the number of 3DCVs that resolved the cube which defined the expansion zone.

Case	3D-resolution	Exp. res.	Δx [mm]	M
C1	$10 \times 7 \times 7$	1	0.03	30
C2	$30 \times 21 \times 21$	$3^3 = 27$	0.01	10

The expansion algorithm followed principally the steps described in Sec. 4.3.3. If the wafer after sampling was determined to expand, two copies of the wafer were created (i.e., $\Phi = 1$). The original wafer was replaced by the two new copies, which in sum had the same mass but half the density of the original.

The coupled model was run until convergence between LEM3D and RANS by the following procedure:

(1) A plug flow velocity profile was assumed for the initial LEM3D simulation. For the first global iteration the lateral prescribed displacements were zero. For the succeeding global iteration steps, the lateral prescribed displacement components were given by the updated RANS velocities given by Eq. (4.11).

(2) The following four steps were implemented on the advective time scale Δt:

   (a) The auxiliary coupling by random rotations were implemented as given in Sec. 4.7.1.

(b) The volume expansion part was determined by randomly sampling the wafers to be expanded from the given distribution. The lateral displacement components were estimated by the banking (Eq. (4.12)), while the streamwise components were given from the continuity equation (4.17).

(c) The advection including the possible dilatation were implemented as given by step (3)(e) in the procedure in Sec. 4.10.

(d) Data for the mean density (4.40) and the 3DCV filtered mean density (4.45) were sampled at the last step in the LEM3D cycle. After an initial time lag, the velocity, mass flux and density data were sampled every time step.

(3) Item (2)(a) through (2)(d) were repeated until statistical convergence of the data sampled in (2)(d).

(4) The 3DCV filtered density solution from LEM3D was provided to the RANS solver. The Favre-averaged RANS-equations were further solved by iteration to a stationary solution.

(5) For the two-way coupling, step (1) through (4) were repeated until convergence between LEM3D and RANS was achieved.

The inlet plug flow velocity was set to $1\,\mathrm{m/s}$, and the density of the wafers entering the domain was $1\,\mathrm{kg/m^3}$. The $\mathrm{CFL_{adv}}$-number was kept at 0.1, and the rotation frequency was set to $\nu_r = 1.5$. RANS applied a slip condition on the side-wall (lateral) boundaries. The k-ε model equations were solved to provide the turbulence viscosity to the momentum equation, but since triplet maps stirring was omitted, the turbulence field had no direct influence on the LEM3D evolution. A turbulence intensity of 10 % and a turbulence length scale of 0.1 m was applied on the inlet boundary.

7.2.2 Data collection and definitions

For LEM3D, the mean mass flow rate was determined by sampling the displaced mass across the 3DCV boundary nn by

$$\overline{\rho w}_{nn} = \left[\frac{1}{N_s} \sum_{j=1}^{N_s} \left(\sum_{i=1}^{\delta_{nn}^j} \rho^{j,i} \right) \right] \frac{\Delta x_\mathrm{w}}{3\Delta t}, \tag{7.1}$$

where δ_{nn}^j is the number of displacements for the sampling j over the 3DCV face nn and $\rho^{j,i}$ is the density of the ith displaced wafer. The mean wafer

velocity across a 3DCV face was sampled by Eq. (5.12), while the mean 3DCV filtered density $\widehat{\rho}$ was sampled as described in Eq. (4.45).

Control volume center densities in RANS were given from LEM3D by the mean 3DCV filtered densities $\widehat{\rho}$. The RANS boundary velocity was the Rhie-Chow interpolated value. The RANS boundary mass flow, $\widetilde{F}_{nn}$, was further given by multiplying the boundary velocity with the arithmetic mean density of the two adjacent center nodes. The solution algorithm used in RANS conserved mass on a control volume and domain basis.

7.2.3 Deviations in mass flows and the streamwise bias

The lateral velocities in LEM3D were matched to the prescribed components from RANS by the banking method (see Sec. 4.5.3). The prescribed displacements were given by

$$\gamma_{nn} = \frac{3\widetilde{F}_{nn}\Delta t}{\widetilde{\rho}_{nn}\Delta x_{\mathrm{w}}}. \tag{7.2}$$

Prior to wafer advancement, we do not know the average density $\overline{\rho}_{nn}$ of the wafers crossing the 3DCV boundaries in LEM3D. The best guess that is applied in Eq. 7.2 is the RANS arithmetic mean density $\widetilde{\rho}_{nn}$. Thus, we can not exactly prescribe the number of wafers needed to represent the mean mass flow. Hence, differences between average lateral mass flow components in LEM3D and RANS are expected to occur.

Mass conservation was in LEM3D ensured through Eq. (4.17), hence determining the streamwise component. This method has inevitably an inherent bias to the streamwise direction. The correction algorithm presented in Sec. 4.5.4 was developed for solenoidal velocity fields, i.e., $\nabla \cdot \mathbf{u} = 0$, and thus was not feasible for the present simulations. This means that any deviation from the expected volume expansion was embodied in the streamwise component. For instance, if the average expansion rate corresponded to one wafer per 3DCV per time step, and at an instant two wafers were expanded, the *streamwise* displacement component was increased by one wafer independent of whether the expansion occurred on the streamwise or on the lateral oriented LEM-domains. The lateral dilation was first taken into account by the updated velocity field from RANS at the next global iteration step. The effect of the streamwise biased dilatation method on the final solution was not further investigated, but is briefly discussed in Sec. 7.4.3.

7.3 Test case results

The expansion zone was defined by the cube $0.12 \leq \mathrm{x} \leq 0.15$, $0.09 \leq \mathrm{y} \leq 0.012$, and $0.09 \leq \mathrm{z} \leq 0.12$ as indicated by the grey square in Fig. 7.1. For case C1, the cube consisted of one single 3DCV at $q = 5, r = 4, s = 4$, while for C2 it was resolved by 27 3DCVs in the range $13 \leq q \leq 15$, $10 \leq r \leq 12$, $10 \leq s \leq 12$.[1] The expansions created lateral density gradients which necessitated velocity feedback from RANS in order to represent the lateral dilatation.

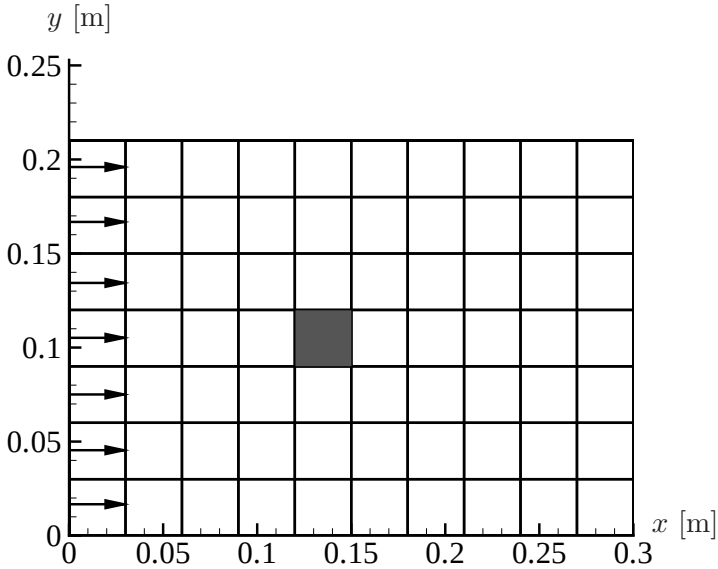

Figure 7.1: The axial center plane of the expansion test case. The inlet boundary is to the left, while the outlet is the right boundary. The expansion zone is indicated by the grey 3DCV. The grid for case C2 is not shown, but is a refinement of the grid by a factor 3.

7.3.1 Iteration procedure and overall convergence

The coupled model was run as described in Sec. 7.2. Figure 7.2 shows the time evolution of the mean 3DCV filtered density in LEM3D for the 3DCV at $q = 8$ ($0.21 \leq \mathrm{x} \leq 0.24$) in the center of the domain for case C1. The global iteration steps mark the instants where interaction with RANS

[1] See Sec. 4.5.1 for indexing of LEM3D

occurred. The small disturbance in the density at these points stemmed from that the LEM3D statistics were gathered from scratch at every LEM3D run. After the second iteration with RANS, the density was stabilized on a level that was more or less constant. For higher accuracy, each LEM3D simulation should have been run longer to gather more statistics in between the interactions with RANS.

The LEM3D simulations were run with updated velocities from RANS which provided a new density field to RANS, and so forth. We let the discrepancies in the lateral velocity profiles from the two last RANS runs indicate the level of convergence. By this criteria an approximate converged state was established already after the second global iteration for the present case. The simulation was run for 10 global iterations.

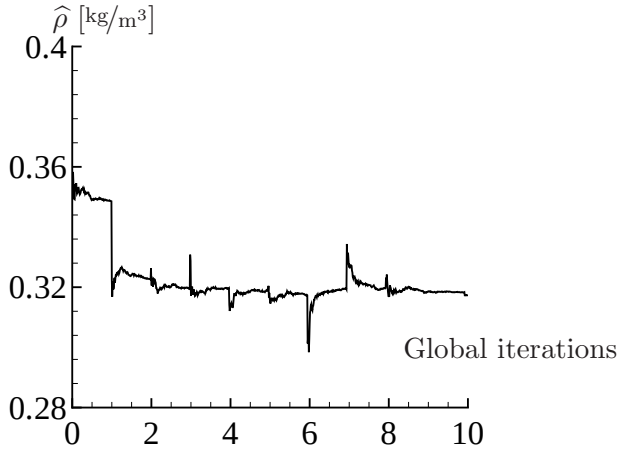

Figure 7.2: The evolution of the mean 3DCV filtered density in the center 3DCV at $q = 8$ for case C1. The global iteration steps are the instants where interaction with RANS occurred. The final LEM3D run was from 8-10.

7.3.2 Comparison of velocity and mass flux profiles

The velocity and mass flux component profiles for test case C1 are shown in Fig. 7.3. In Fig. 7.3(a), the lateral variations of the average lateral wafer velocity component for LEM3D (solid line) and the mean velocity component for RANS (dashed line) through the center of the layer of 3DCVs at $q = 6$ are shown. As expected, the banking method using the prescribed displacements in Eq. (7.2) provided an average wafer velocity overlapping the RANS velocity input. However, considering the mass flux profiles at the same location in Fig. 7.3(b), there is clear deviation. The deviation is

due to that the average density of the wafers crossing the 3DCV boundary was different from the interpolated density that set the RANS mass flux. LEM3D conserved mass at every 3DCV and time step by calculating the streamwise displacement component from Eq. (4.17). This resulted in a deviation between the streamwise average wafer velocity in LEM3D and the mean RANS velocity, Fig. 7.3(c), and mass flux, Fig. 7.3(d), which was accumulated downstream as seen.

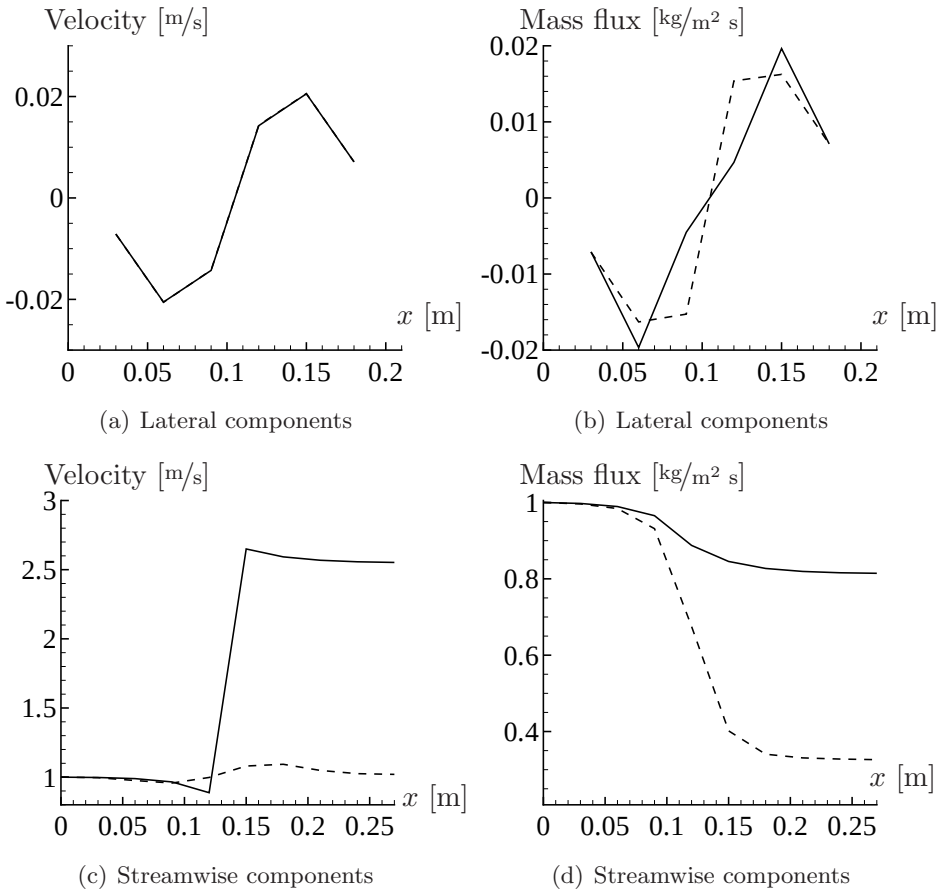

(a) Lateral components

(b) Lateral components

(c) Streamwise components

(d) Streamwise components

Figure 7.3: Converged results with the coupled model of LEM3D (solid line) and RANS (dashed line) for test case C1. Comparison of velocity and mass flux component profiles in the different models. The components on the "wall" nodes are not shown for the lateral profiles.

For test case C2 the grid was refined with a factor 3 as described in Sec. 7.2.1. The results are shown in Fig. 7.4. Even though the deviation

between the lateral mass flux profiles in Fig. 7.4(b) was reduced compared to case C1 in Fig. 7.3(b), the deviations for the streamwise components were still significant. In the Figs. 7.4(c) and 7.4(d) the streamwise velocity component is shown for the center x-profiles ($r = 11$ and $s = 11$) and the x-profiles at $r = 10$ and $s = 10$. The deviation was somewhat, but not significantly reduced with the grid refinement. One explanation is that increasing the number of 3DCVs increased the number of 3DCV faces where lateral mass flow deviations were accumulated.

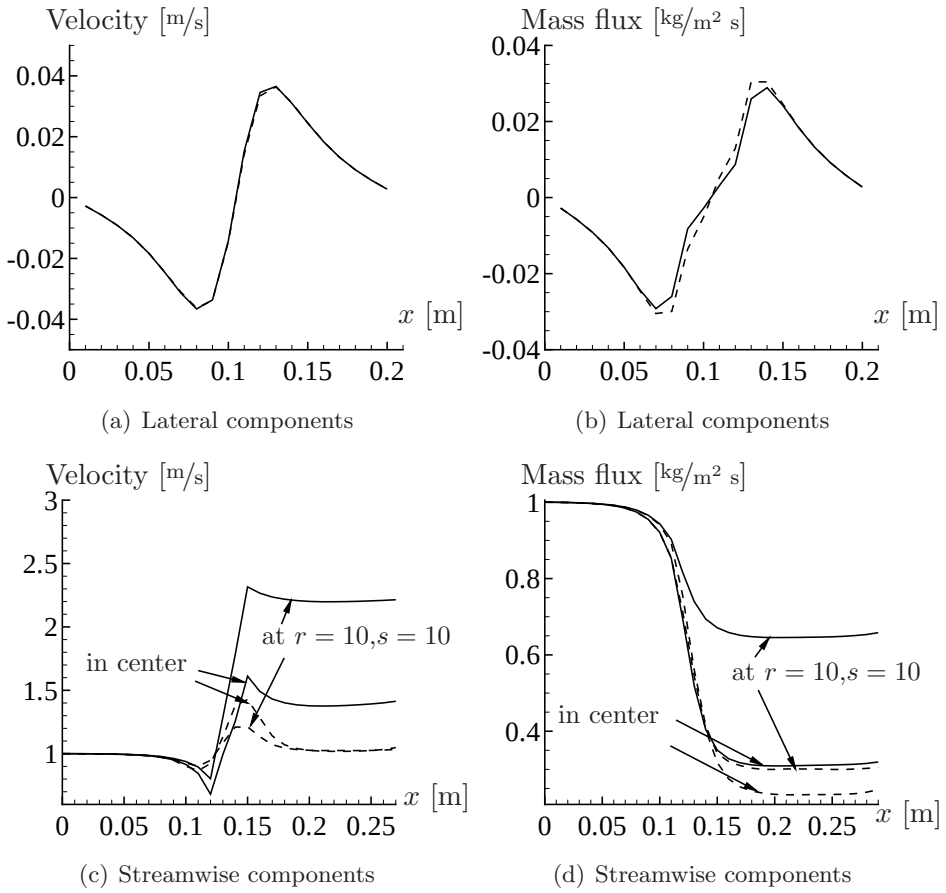

(a) Lateral components

(b) Lateral components

(c) Streamwise components

(d) Streamwise components

Figure 7.4: Converged results with the coupled model of LEM3D (solid line) and RANS (dashed line) for test case C2. Comparison of velocity and mass flux profiles in the different models.

7.4 Suggestions for alternative strategies

The previous section showed that the combination of the banking method, which is non-conservative in density varying flows, and the continuity equation (4.11) led to deviations that accumulated in the streamwise direction. Based on this a few development strategies for displacement handling are proposed. The basic iteration procedure between RANS and LEM3D that has been established also needs further development and refinement in terms of relaxation and adaptivity.

7.4.1 Matching the lateral mass flows

Contrary to the velocity, the mass flow is a *conservative* property in density varying flows. Hence, it is appealing to match the lateral mass flows instead of the lateral velocities in LEM3D and RANS. However, the banking described in Sec. 4.5.3 can not be directly applied to the mass flow, since the density of the wafers crossing the boundary is varying randomly. Thus, a non-trivial control mechanism is needed. The control mechanism can be developed to match the mass flow on the large time scale, or by including an internal loop, where we try to reduce the mass flow deviations as much as possible at every time step. If this control mechanism is proven successful, the lateral mass flow in RANS and LEM3D will match on average. Mass conservation is ensured by Eq. (4.17), and since the respective lateral mass flow components match, the streamwise mass flow will also do. Local deviations in velocity will only occur due to the interpolation of the densities to the boundaries.

7.4.2 Extending from one-to-one grid correspondence

The current implementation assumes a one-to-one correspondence between the RANS and LEM3D grid. If instead a general RANS grid can be adopted, the possible RANS discretization errors may be reduced. An algorithm for interpolating the velocity and diffusivity field from RANS to LEM3D and the density field from LEM3D to RANS is thus required.

7.4.3 Avoiding the streamwise bias

The present algorithm applies the banking in the lateral direction and ensures local continuity in the streamwise direction by Eq. (4.17). The advection advancement is performed by processing the 3DCVs layer by layer, starting from the upstream layer. The inherent streamwise bias in this

method can be reduced by alternating the direction in which the displacements are calculated. That is, the layer by layer calculation can be performed starting for instance at the *west* end, which implies solving Eq. (4.10) with respect to δ_e. Similarly we can start at the east, south, north and possibly bottom directions.[2] The alternation between directions can be implemented by random selection from a uniform distribution.

Another alternative may be to let the expansions influence the displacements in the direction in which they occur. However, this necessitates that the expansions are performed only for the 3DCVs belonging to a checkerboard subset of the domain. The checkerboard subset is alternated from time step to time step similar to the error minimization procedure proposed in Sec. 4.5.4.

7.5 Concluding remarks

The one-way and two-way coupled RANS-LEM3D model was tested in a simplified setup. Successful runs to a statistically steady state solution were performed on two different grids. The lateral mass flow deviations between RANS and LEM3D were accumulated in the streamwise direction. The deviations were not significantly reduced by increasing the 3D-resolution.

The streamwise displacements are calculated from the lateral components plus the possible excess expansion. Hence, the method is inherently directionally biased. In further development of the reacting RANS-LEM3D, the following should be employed: First, a method that match corresponding conservative properties, e.g. the mass flow, should be developed. Secondly, the streamwise bias should be avoided, possibly by the method proposed in Sec. 7.4.3.

The present test cases were simplified compared to the full featured LEM3D model. Introducing triplet map stirring further complicates the mass conservation. If the turbulence diffusivity is uniform and the density profile is non-uniform, there will on average be a net mass transfer in or out of the 3DCV due to triplet map wafer rearrangements. Certainly, the turbulence diffusivity profile will be based on RANS computations, which are influenced by the LEM3D density field. However, it is not given that the turbulence diffusivity profile will govern the triplet maps such that it provides on average zero net mass transfer in the case of a non-uniform density field.

[2]Note that the direction in which the layer by layer calculation is performed, must currently terminate in a free outlet boundary.

Chapter 8

Passive scalar mixing in a turbulent jet

8.1 Introduction

The turbulent jet is a well-documented flow which is relevant to a number of practical and industrial applications. Hence, it has been subject to numerous experimental and analytical studies (Tennekes and Lumley, 1972; Wygnanski and Fiedler, 1969; Hussein *et al.*, 1994; Pope, 2000). Scalar mixing in turbulent jets is a challenge in experimental as well as modeling and computational work (Dimotakis, 2005). The most commonly performed turbulent scalar mixing jet case is the one where a jet of fluid 1 emerges into fluid 2. Fluid 1 and fluid 2 can contain different species or they can have different temperatures. Such setups are for instance reported in Dowling and Dimotakis (1990) and Panchapakesan and Lumley (1993b). The approach in Tong and Warhaft (1995) differs from these studies, since the scalar is introduced on a length scale much smaller than the flow scales and localized in the self-similar region of the turbulent jet.

In this chapter, the full-featured non-reacting LEM3D is assessed by comparison with the measurements by Tong and Warhaft (1995) of scalar dispersion in a turbulent jet. The numerical solutions (FV) to the model transport equation for the scalar mean and variance are also employed for comparison.

8.2 Experimental setup

In the experiments by Tong and Warhaft (1995), the dispersion and mixing of scalar fluctuations were studied by measuring temperature fluctuations from one and two heated rings placed concentrically in the self-similar region of a turbulent jet. Previously, Warhaft (1984) measured the scalar mixing from line sources in grid turbulence. Contrary to the homogeneous grid turbulence, the turbulent jet has shear, which enhances mixing and allows measurements of clear asymptotic values. A 2 mm diameter ring source, made of a 0.254 mm diameter wire, is used to approximate a point source. A source this small is only applicable for measurements in the proximity of the source due to the limited power through the wire. Larger rings, which enable more power, will have somewhat faster dispersion because they are placed in the shear layer of the jet. Sufficiently far from the source, the normalized scalar fluctuations from the rings approach the same asymptotic value. Several different ring diameters are investigated in Tong and Warhaft (1995), and their results indicate that the centerline normalized rms decreases with increasing ring diameter in the region before the scaled rms approach a common self-similar solution. Hence, there are reasons to assume that the rms for the 10 mm ring source which is used as comparison with LEM3D rms data is somewhat lower than for a 2 mm ring source. Experimental rms results for the 2 mm source was not reported by Tong and Warhaft (1995). For the present work, the measured mean results from a single 2 mm and a 10 mm ring source and the scalar rms from a 10 mm and a 40 mm ring source were utilized for comparison to point source simulations with LEM3D.

A sketch of the setup is given in Fig. 8.1. The ring sources are placed at a distance $x_0 = 9D_j$ downstream the nozzle, where $D_j = 30\,\text{mm}$ is the jet nozzle diameter. Details about the velocity measurements are found in Panchapakesan and Lumley (1993a), who used the same jet facility to measure velocity statistics. Negligible measurable effects were observed on the flow field from the heated rings placed in the self-similar region.

A few different jet configurations are reported in Tong and Warhaft (1995). The experimental characteristics relevant to the present model simulations are given in Tab. 8.1. The jet Reynolds number Re_j is based on the cold jet outlet conditions. The integral scale l_t is taken as the measured jet half-width $r^0_{1/2}$ at the position where the sources are placed and the turbulence Reynolds number is calculated from the integral scale and the measured velocity fluctuation. The Kolmogorov scale is estimated from the relation (2.28). The distance relative to the source is defined as $x' \equiv x - x_0$,

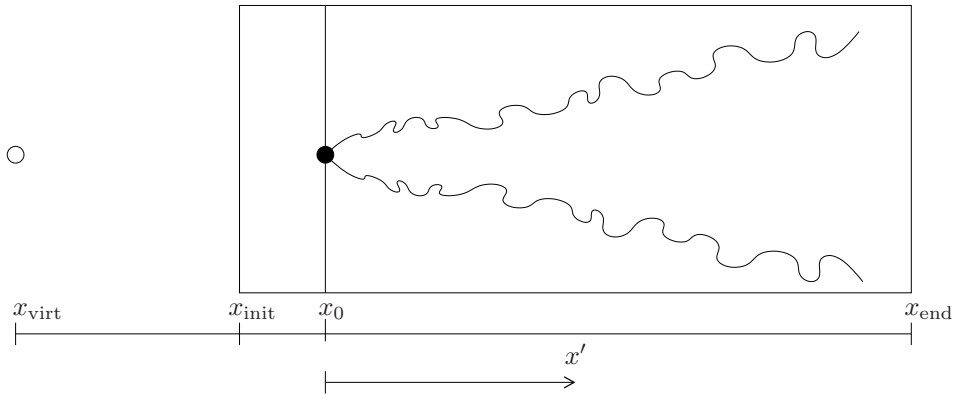

Figure 8.1: Schematic setup of the scalar mixing experiment. The virtual origin of the jet is at $x_{\text{virt}} = 0$. The upstream boundary of the computational domains were placed at $x_{\text{init}} = 7.4D_j$ and $x_0 = 9D_j$ for the LEM3D domain and the FV domain, respectively. The figure is not to scale.

and the approximate streamwise distance from the source corresponding to one eddy turnover time x'_{T_L}/D_j is given as reported by Tong and Warhaft (1995).

Table 8.1: Characterization of the turbulent jet as reported by Tong and Warhaft (1995).

Jet nozzle, D_j	30 mm
Jet nozzle velocity, U_j	9 m/s
Jet Reynolds number, Re_j	18000
Integral scale at x_0 (taken as $r^0_{1/2}$)	28 mm
Turbulence Reynolds number, Re_t	2300
Kolmogorov scale, $\eta = l_t Re_t^{-3/4}$	0.08 mm
Distance for one eddy turnover, x'_{T_L}/D_j	~ 5

8.3 Numerical setup

8.3.1 Characterization of the turbulent jet

The self-similar mean jet velocity field needed as input to LEM3D was given as described in chapter 5.2.2.

The work of Panchapakesan and Lumley (1993a) is based on measurements of a turbulent round jet ($Re_j \sim 11000$) emerging into quiescent cold air. Comparisons are made with work in similar configurations with jet Reynolds number in the range from 80000 to 95000. Even though there are some distinctions between the works, general trends such as the Gaussian shaped axial mean velocity profile and the normalized Reynolds stress variation across the jet are reported to be in reasonable agreement between all experiments.

The normalized Reynolds stress variation across the jet was here approximated by a curve fit to the function

$$\frac{\overline{u_x' u_r'}}{U_c^2} = \frac{1}{2}\frac{r}{x}\exp\left[-K_{\nu_t}\left(\frac{r}{x}\right)^2\right], \tag{8.1}$$

where $K_{\nu_t} = 120$ provided the best fit to the data reported by Panchapakesan and Lumley (1993a). For the current calculation we assumed the boundary layer approximation, i.e., the radial variation of the mean axial velocity component is much larger than the axial variation of the radial component.[1] This reduces the model for the following Reynolds stress component to

$$-\overline{u_x' u_r'} = \nu_t \left(\frac{\partial \overline{u}_x}{\partial r}\right). \tag{8.2}$$

The left hand side is given from Eq. (8.1) multiplied with the square of the mean centerline velocity which is given in Eq. (5.6). The right hand side of Eq. (8.2) is calculated by partial derivation of Eq. (5.7). Assuming a constant turbulence Schmidt number of $\sigma_t = 0.7$ the turbulence diffusivity field can be estimated from

$$D_{\mathrm{T}} = \frac{\nu_t}{\sigma_t} = \frac{\overline{u_x' u_r'}}{\frac{\partial \overline{u}_x}{\partial r}\sigma_t}. \tag{8.3}$$

We used the analytical and numerical tool MATHEMATICA by Wolfram (1999) to evaluate the expressions above and to obtain the turbulence diffusivity field needed as input to the LEM3D simulations.

[1] This implies that the second term in the model for the Reynolds stress components, as it is written in Eq. (B.4) in the Appendix, was neglected.

8.3.2 The finite volume method

The numerical solution to the transport equations of the scalar mean (3.8) and variance (3.10) by the finite volume method is also here referred to as FV. The numerical method is outlined in Sec. 6.2.3. Note that the velocity and turbulence diffusivity fields were provided from the Eqs. (5.10) and (8.3), respectively. Thus, the discretized partial differential momentum and turbulence model equations were not solved. This procedure was motivated by achieving the closest comparison to the LEM3D simulations by removing uncertainties related to turbulence modeling.

The $0.4\,\mathrm{m} \times 0.328\,\mathrm{m} \times 0.328\,\mathrm{m}$ domain was resolved by a uniform Cartesian mesh of $50 \times 41 \times 41$ control volumes. The upstream boundary was located at x_0 and the downstream boundary at x_{end} as shown in Fig. 8.1. The point source was placed on the upstream boundary of the grid and was resolved by 3×3 control volumes. The source diameter was hence significantly larger in this setup (corresponding to $\sim$27 mm) than in the experiment (2 mm). Numerical accuracy was assessed by doubling the number of control volumes to $100 \times 81 \times 81$ on a domain of similar size. For the mesh with double resolution, the source diameter was correspondingly reduced by a factor 2. In addition, we computed a case where the source was represented by a single control volume, providing a source diameter of $\sim$4.5 mm. Figure 8.2 compares the lateral scalar mean and the root mean square (rms) from computations with the fine and coarser mesh. Both calculations used a one control volume source. Results with a 3×3-control volume source are not shown, but exhibited negligible discrepancies to the reported results. At the downstream locations of interest, the scaled mean and the scalar rms were close to independent of the domain and the source resolution for the meshes considered.

The upstream boundary was a regular inflow boundary with constant values for the mean and the variance, and the outflow boundary was treated as purely convective flux with zero streamwise gradients. The side face boundaries were taken as symmetry boundaries, where normal gradients were set to zero. Generally, the domain was large enough so that gradients toward the boundaries were small.

The turbulence energy k and its dissipation rate ε needed as input to the scalar dissipation term in Eq. (3.11) were determined by using the expression for turbulence viscosity (3.6) and the dissipation rate (3.12). In the latter expression, an integral scale must be chosen to close the equation set. The integral scale was set so that the turbulence intensity, defined by $I \equiv u'/\overline{u}$,

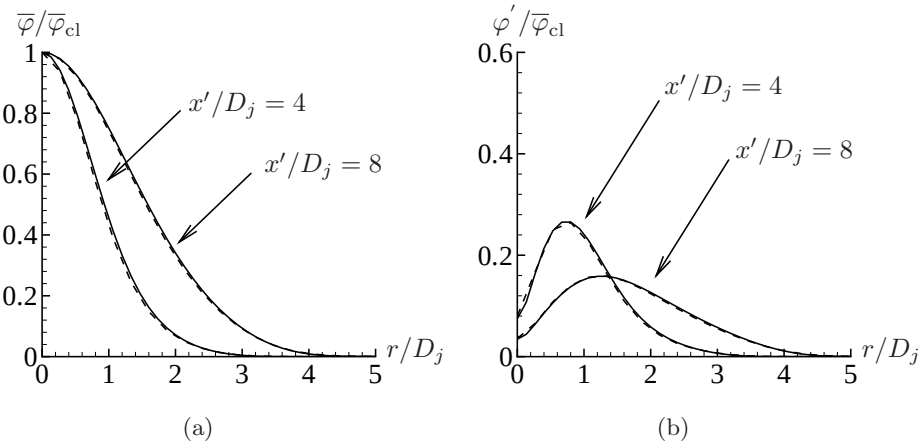

Figure 8.2: Grid sensitivity results from the finite volume method with grid resolution of 50×41×41 (dashed) and 100×81×81 (solid) control volumes. Center lateral profiles at two selected downstream positions for normalized (a) mean scalar and (b) scalar rms.

was close to ∼20% in the center at x_0.[2] A turbulence intensity of 20% was justified by considering the velocity fluctuation to the mean velocity across the jet in the self-similar region for various experiments compiled in Panchapakesan and Lumley (1993a) (See Fig. 9-11 in that paper). This gave a turbulence integral scale of $l_t = 5\,\text{mm}$. The k- and ε-fields were estimated from the expressions as mentioned, where the turbulence diffusivity field was given from the self-similar solutions given in Sec. 8.3.1. The turbulence length scale was constant and spatially uniform, corresponding to the setup of LEM3D.

8.3.3 The LEM3D setup

The full-featured non-reacting LEM3D, as given by steps (2) through (4) in the simulation procedure in Sec. 4.10, was used for the present simulations. The input data to the LEM3D is given in Tab. 8.2. The cases R1-R4 were chosen in order to investigate the effect of variation in model integral scale, whereas R5 and R6 examined the sensitivity to the 1D-resolution. The 3D-resolution was varied between R6 and R7. R8 extended the domain in the R1 case to follow the results farther downstream. In addition, the effect of variation in rotation frequency was considered for case R1.

[2] u' was estimated by the definition of k.

Table 8.2: Input data to the LEM3D simulations. Length scales are given in [mm] and time scales in [s]. The four right columns are estimated from the input. See the text for further explanation.

Case	Resolution	Δx	M	L	L_K	$L^*_\mathrm{K}/L_\mathrm{K}$	T_L	x'_{T_L}/D_j
R1	50×41×41	8	40	56	0.31	7.9	0.070	9.3
R2	50×41×41	8	160	14	0.076	7.9	0.014	2.3
R3	50×41×41	8	80	28	0.15	7.9	0.030	4.7
R4	50×41×41	8	40	112	0.61	3.9	0.18	19.
R5	50×41×41	8	20	56	0.31	16.	0.070	9.3
R6	50×41×41	8	80	56	0.31	3.9	0.070	9.3
R7	100×81×81	4	40	56	0.31	3.9	0.070	9.3
R8	80×51×51	8	40	56	0.31	7.9	0.070	9.3

A grid of $50 \times 41 \times 41$ 3DCVs resolved the domain in the base case. The 1D-resolution was generally kept at $M = 40$, but was also varied to investigate the sensitivity. The source was fed before every triplet map event to the wafer located in the streamwise center domain immediately upstream of $x = x_0$, i.e., the wafer at X_{q,r_c,s_c}, where $q = 6M$, $r_c = 21$, and $s_c = 21$ for all cases except R7.[3] The upstream end of the LEM3D domain was placed at $x_\mathrm{init} = 7.4D_j$ (see Fig. 8.1). By placing the inlet boundary upstream of the source, we avoided that the scalar statistics were affected by the boundary truncation of triplet maps on streamwise LEM domains.

The lateral extension of the source, which was limited downwards by the 3DCV size, was wider (8 mm) than the 2 mm ring source in the experiment. The effect of refining the grid was investigated, and is presented in the Sec. 8.4.3. The thickness of the source, which was limited by the wafer thickness, varied between 0.05 mm in case R2, to 0.4 mm in case R5.

Data was sampled as described in Sec. 4.9 after an initial simulation time of 5000 time steps. This lag was introduced to have a statistically stationary condition before sampling the data. The data sampling rate was one sampling every 100 time step. We assumed that the individual samplings were statistically independent. To assess the validity of this presumption, a case with one sampling every 200 time step was run. It was verified that the effect of sampling rate on the presented statistics was minimal. A total of 450 samples yielded sufficient accuracy to the present results, however, 2000 samples were collected in order to have somewhat smoother scalar variance profiles.

[3]For R7, $q = 12M$, $r_c = 41$, and $s_c = 41$.

The relative rotation frequency was set to $\nu_r = 1$ for all cases, except when the rotation frequency was varied. The rotation frequency field followed the velocity field as given by Eq. (4.36). For all cases, the $\mathrm{CFL}_{\mathrm{adv}}$-number was kept at 0.2.

By the derivation described in Sec. 8.3.1, the center turbulence diffusivity along the axial centerline was $\sim 0.008\,\mathrm{m}^2/\mathrm{s}$. The molecular diffusivity was set to the constant value of $2\times10^{-5}\,\mathrm{m}^2/\mathrm{s}$. Hence, on the centerline, the Peclet number was estimated to $Pe \sim 400$ and the turbulence Reynolds number was $Re_S \sim 1100$ applying the relations given in Sec. 3.2.3. The model Kolmogorov scale, estimated from the relation (3.18), is given in Tab. 8.2. Due to limitations primarily in computer memory and secondly in requirements of cpu-hours, the turbulence spectrum was only partially resolved. The ratio of the model Kolmogorov scale to the smallest implemented eddy is also given in Tab. 8.2, indicating that the turbulence spectrum was underresolved by a factor in the range ∼4–16 on the centerline. Note that this factor was somewhat smaller off the centerline, where the turbulence diffusivity was lower. A triplet map consists of a multiple of 3 wafers where the smallest possible triplet map is $L^*_{\mathrm{K}} = 3\times2$. In the present work, $L^*_{\mathrm{K}} = 3\times4$ wafers were used to represent the smallest possible triplet map (see the discussion in Sec. 4.3.2).

The approximate distance corresponding to one eddy turnover time from the source position was estimated by $x'_{T_L} = U_c T_L$, where U_c was the average mean center velocity in the range $[x_0, x'_{T_L}]$, the model eddy turnover time was $T_L = L/u'$, and the velocity fluctuation was calculated by assuming a turbulence intensity of $I \equiv u'/U_c = 20\%$. The data is reported in Tab. 8.2.

8.4 Results

In the following sections, we compare the LEM3D simulations with experimental data and FV computations. The sensitivity to 1D- and 3D-resolution, the frequency of random rotations, and the model integral scale were investigated. Mean values were sampled either as the 3DCV filtered mean (4.40) with 3D-resolution, or along selected LEM-domains with 1D-resolution as given by Eq. (4.45). Scalar variance was also sampled along selected domains with 1D-resolution. See Chapter 4.9 for further details on the data gathering.

8.4.1 Influence of displacement corrections, wafer flipping and jitter

The displacement correction procedure described in Sec 4.5.4 was applied to all LEM3D simulations with a threshold $\delta_{\text{th}} = 1$. One simulation for the R1 case was run without corrections and compared to the corresponding simulation with corrections. The difference between the scalar mean and rms results for these two cases were found to be negligible. The effect related to the corrections was also discussed in Sec. 5.2.1.

The flipping due to shear flow (see Sec. 4.5.5) will bring dissimilar wafers in contact, which further will enhance molecular diffusion and reduce the rms. This effect was investigated by monitoring the number of flipping events for one simulation with corrections and one without corrections. It was found that the corrections increased the number of flipping events by approximately a factor 3. This was caused by the corrections, which adjust the lateral components more often resulting in more flipping events. Since the rms results were not significantly affected by the corrections for this case, we can conclude that the rms reduction from flipping was negligible.

The same conclusion applies to the jitter of the wafer velocity components. The jitter was investigated in Sec. 5.2 and it was shown that the corrections decreased the magnitude of the jitter. Hence, the present result also indicate that the jitter had negligible effect on the mean and rms values. However, a broader investigation is needed in order to fully verify this preliminary conclusion.

8.4.2 Effect of random rotations

The purpose of the random 3DCV rotations, presented in Sec. 4.7, is to ensure sufficient coupling between all LEM-domains in LEM3D. This property and the effect on the scalar rms was investigated for case R1 by comparing results from simulations with the default rotation frequency (i.e., $\nu_r = 1$) with two simulations where the frequency was increased to $\nu_r = 4$ and reduced to $\nu_r = 1/4$, respectively.

The mean spreading of a point source in a turbulent jet is an axisymmetric case. Thus, profiles in the lateral Cartesian coordinate directions should coincide with profiles diagonally to those coordinate directions. Here, we considered the 3DCV filtered scalar mean profiles normal to the lateral coordinate direction, $\widehat{\varphi}_y$, and along the diagonal $\widehat{\varphi}_r$.

The half-width is the radial distance from the centerline at which the mean scalar value is half its centerline value. The results for the half-with of the $\widehat{\varphi}_y$ and $\widehat{\varphi}_r$-profiles are shown in Fig. 8.3. The half-width was scaled

by the reported experimental value at $x = x_0$. The figure shows that none of these cases exhibited perfect symmetry. Disregarding the zone closest to the source, the deviation between the $\widehat{\varphi}_y$- and $\widehat{\varphi}_r$-profiles decreased as expected with increasing rotation frequency, i.e., higher frequency provided better directional coupling. The non-symmetric behavior was also slightly decreasing with downstream distance from the scalar source.

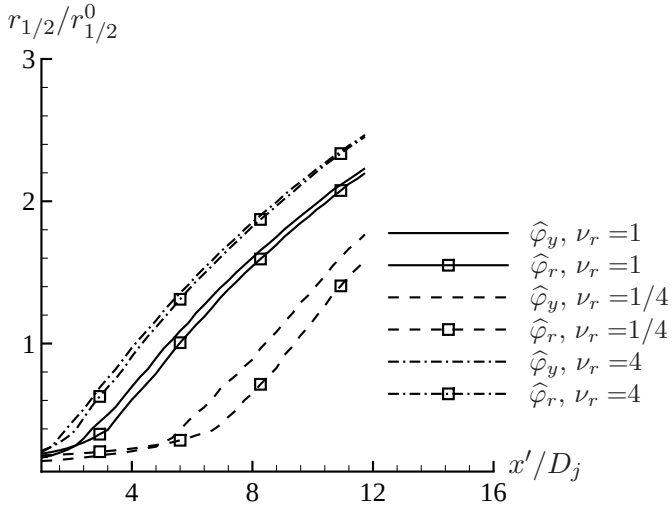

Figure 8.3: Half-width of the mean scalar profile normalized by the half-width $r^0_{1/2}$ measured at $x = x_0$ as a function of downstream position from the point source. Comparison of results from LEM3D simulations with different rotation frequencies, where the half-width was estimated for scalar mean filtered profiles normal to the lateral coordinate direction $\widehat{\varphi}_y$ and along a diagonal to the two lateral coordinate directions $\widehat{\varphi}_r$.

For $\nu_r = 1/4$, the scalar was considerably less spread in the diagonal than the normal direction. Thus, a relative random rotation frequency of $\nu_r = 1/4$ provided insufficient coupling. The half-width increased with increasing rotation frequency, due to the additional dispersion caused by the random rotations. Similar behavior was observed for the point source case in Sec. 6.2.5.

In Fig. 8.4 the effect of rotation frequency on the scalar rms normalized by the centerline mean is shown along the centerline and for center lateral profiles at $x'/D_j = 8$. The axial normalized scalar rms profiles are also compared to experimental data of the dispersion from a 10 mm source. Increasing the rotation frequency from $\nu_r = 1$ to $\nu_r = 4$ decreased the rms, especially in the range $x'/D_j = 2$–10. Note that the discrepancy be-

tween the LEM3D simulations with $\nu_r = 1$ and $\nu_r = 4$ actually was larger than shown on the centerline due to normalization by the centerline mean value. According to the results in Fig. 8.4(a), the LEM3D rms declined more steeply than the measured rms, resulting in underestimated values downstream $x'/D_j = 2$. The reduction in rms is believed to mainly stem from the random rotations. This effect was elaborated in Sec. 6.4 and is also further discussed in Sec. 8.4.5. For $r/D_j > 3$ at $x'/D_j = 8$, the scalar rms for the $\nu_r = 4$ case was larger than for $\nu_r = 1$. This was due to the additional dispersion by rotations that distributed more scalar to those positions, and hence, gave higher rms values.

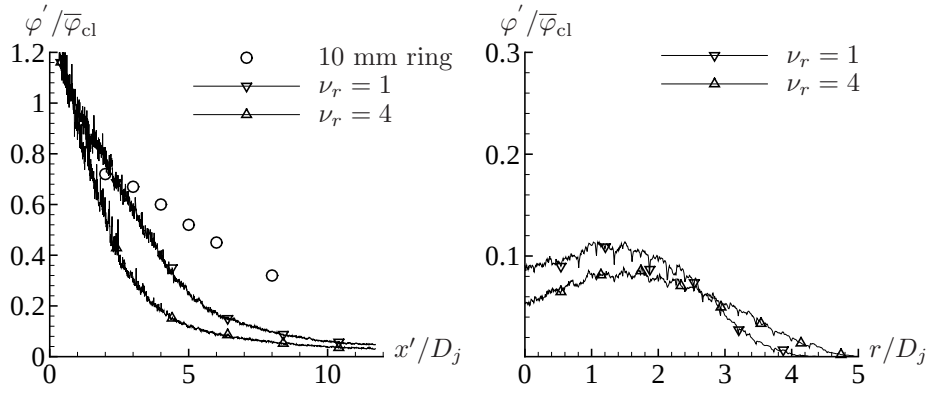

(a) Along the centerline

(b) At $x'/D_j = 8$

Figure 8.4: (a) Axial and (b) lateral profiles of scalar rms normalized by the centerline mean. Comparison of LEM3D simulations with two different rotation frequencies. The axial profiles are in addition compared to measurements of dispersion from a 10 mm ring.

8.4.3 Effect of 3D-resolution

The effect of increasing the number of 3DCVs in LEM3D is generally not analogous to increasing the numerical accuracy. The velocity and diffusivity field, which are provided as inputs will be somewhat better represented by a finer than a coarser grid. But these fields are not solved in LEM3D.

The coarse and fine resolutions were 50×41×41 and 100×81×81 for case R6 and R7, respectively. The wafer thickness Δx_{w} was kept constant to achieve the same resolution of molecular diffusion and the turbulence spectrum as given in Tab. 8.2. The advective residence time is proportional to the size of the 3DCV by Eq. (4.31). Hence, since the rotation frequency is related to the residence time according to Eq. (4.35), the number of rotations per second is doubled when the 3DCV size is halved. Here, the same relative rotation frequency ν_r was applied for R6 and R7, which means that the absolute rotation frequency $\mathcal{R}$ was twice as high for R7 compared to R6.

Figure 8.5 shows the normalized mean 3DCV filtered scalar profiles along center lateral lines at two selected axial positions. The lateral coordinate is normalized by the half-width of the corresponding mean profile. Simulations with LEM3D applying a fine and a coarse 3D-resolution were compared to FV computations. A Gaussian curve fit to experimental mean scalar data for a 2 mm point source in the axial range $x'/D_j = 1$–5 is also given. The effect of varying 3D-resolution on the mean lateral profiles was rather modest at both axial locations, and the simulations exhibited mean profiles close to the experimental data at $x'/D_j = 8$. The discrepancies to the experiments at $x'/D_j = 4$ will be further discussed in Sec. 8.4.5.

In Fig. 8.6(a) the normalized scalar rms along the axial centerline for the fine and coarse grid is compared to experimental data for a ring source of 10 mm. Except for discrepancies upstream $x'/D_j \sim 2$, the rms was less for the finer R7-grid than the coarser R6-grid. One possible explanation to this is that the number of 3DCV interfaces, where wafers are brought in proximity to each other by the rotations, is increased on a finer grid. This enhanced the mixing and reduced the rms. Second, the rotation frequency was higher for R7 than R6 which most likely further increased this effect. Some of the difference was also due to scaling by the centerline mean, which was slightly higher for case R7.

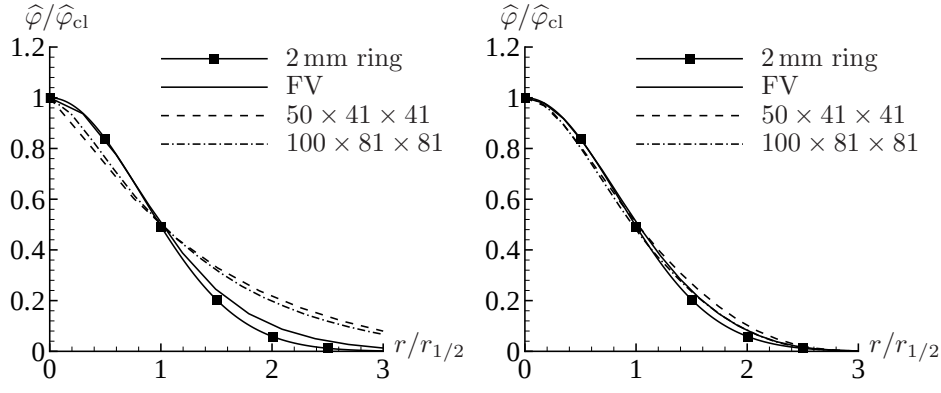

(a) At $x'/D_j = 4$ (b) At $x'/D_j = 8$

Figure 8.5: Comparison of results obtained with the FV and LEM3D with two different 3D-resolutions, $50 \times 41 \times 41$ (R6) and $100 \times 81 \times 81$ (R7). The lateral profiles of mean 3DCV filtered scalar normalized by the centerline value are given at two selected downstream positions.

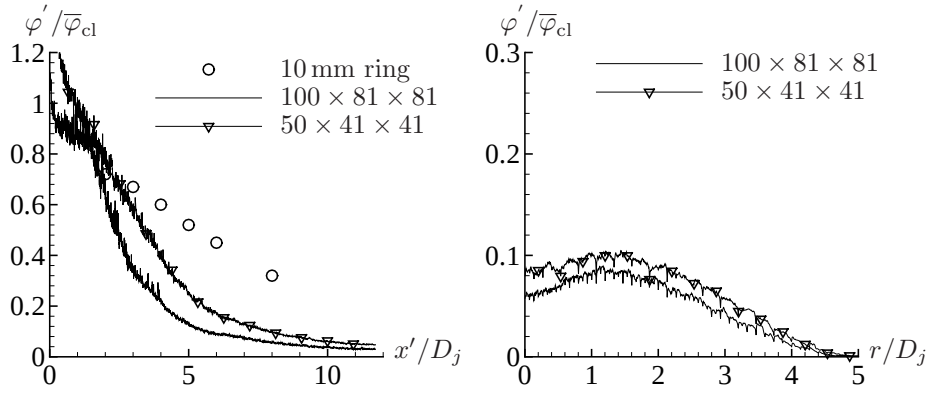

(a) Along the centerline (b) At $x'/D_j = 8$

Figure 8.6: (a) Axial and (b) lateral profiles of the scalar rms normalized by the centerline mean. Comparison of LEM3D simulations with two different 3D-resolutions. The axial profiles are in addition compared to measurements of dispersion from a 10 mm ring.

8.4.4 Effect of 1D-resolution

The mean 3DCV filtered scalar profiles were found to be insensitive to the range of 1D-resolution considered here. The sensitivity of normalized scalar rms to the 1D-resolution is shown in Fig. 8.7. Increasing the 1D-resolution resulted in reduced rms along the centerline of the jet as well as along the lateral profile at $x'/D_j = 8$. According to previous work of Kerstein (1992b), the adequacy of resolution should be ensured by running simulations with increasingly finer resolution until the statistics converge. Hence, the 1D-resolution is generally not a parameter subject to tuning.

For the present predictions, it was shown that a resolution of $M = 40$, which gave a smallest eddy on the order of $\sim 10L_{\mathrm{K}}$, provided sufficient accuracy downstream $x'/D_j \sim 3$ for $L = 56\,\mathrm{mm}$. Reducing the model integral scale causes a reduction in the model Kolmogorov scale according to Eq. (3.18). Hence, to achieve the same resolution of the turbulence spectrum for $L = 28$ and $14\,\mathrm{mm}$, the resolutions in these cases were set to $M = 80$ and 160, respectively. This gave a ratio of the smallest resolved eddy to the model Kolmogorov scale of about $L^*_{\mathrm{K}}/L_{\mathrm{K}} \sim 8$ as reported in Tab. 8.2.

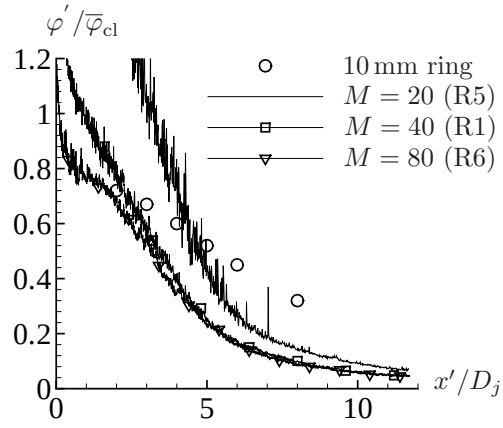

Figure 8.7: Axial profiles of scalar rms normalized by the centerline mean. Comparison of LEM3D simulations with various 1D-resolutions. The data are also compared to measurements of dispersion from a 10 mm ring.

8.4.5 Effect of the model integral scale

The model integral scale was varied between $L = 14\,\text{mm}$ and $L = 112\,\text{mm}$ in the LEM3D simulations R1–R4. In Fig. 8.8, the normalized mean 3DCV filtered scalar profiles along a lateral coordinate scaled by their respective half-widths are shown. As in Fig. 8.5 the results were also compared to a Gaussian curve fit to experimental data in the range $x'/D_j = 1$–5 and to FV computations. At $x'/D_j = 4$, the agreement with the FV method and the experimental results was evidently better for $L = 14\,\text{mm}$ and $28\,\text{mm}$ than for larger model integral scales. Farther downstream at $x'/D_j = 8$, the simulations, except for $L = 112\,\text{mm}$, followed the self-similar behavior exhibited by the experiments. In isotropic turbulence, the turbulent convective regime is extended with increasing integral scale. As discussed in Sec. 6.3, the 1D standalone LEM partly represents this scaling.[4] Reduced model integral scale in LEM causes a shift in the eddy size distribution toward smaller triplet maps with higher frequency which induces faster mixing and in effect gives a faster alignment with Gaussian shape. This is assumed to be the first main reason for the discrepancies between the R1–R4 cases.

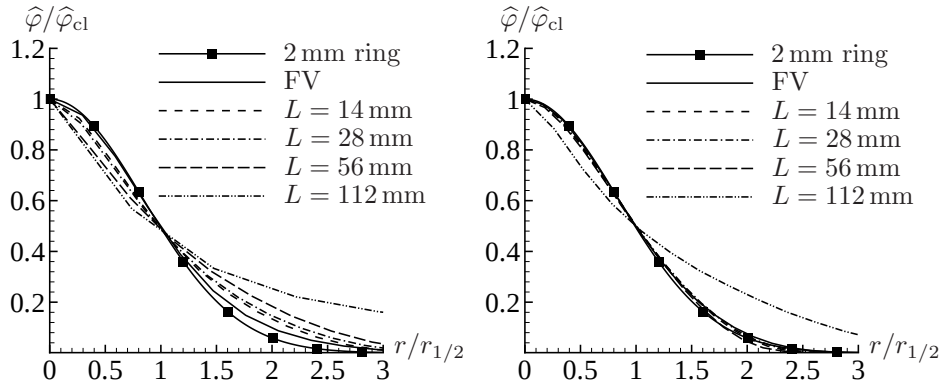

(a) At $x'/D_j = 4$ (b) At $x'/D_j = 8$

Figure 8.8: Comparison of results from LEM3D simulations with various integral scales (case R1-R4), calculation with the finite volume method (FV) and measurements of dispersion from a 2 mm ring. Lateral profiles of scalar mean normalized by the centerline value at two selected downstream positions.

But the alignment with self-similar profiles is also related to the random rotations and the degree of directional coupling. The scalar was initially

[4]Note that the instantaneous triplet mapping introduces artifacts close to the source (Kerstein, 1992b).

introduced only in the streamwise oriented domain. In Chapter 6.2.6, it was found that the degree of directional coupling was a function of the rotation frequency and the normalized time (by the eddy turnover time) from when the source was released. The distance corresponding to one eddy turnover time was estimated to $x'/D_j \sim 19$ for $L = 112\,\text{mm}$ and $x'/D_j \sim 2.3$ for $L = 14\,\text{mm}$ as given in Tab. 8.2. Thus, a given downstream position can be interpreted as being "closer" to the source for $L = 112\,\text{mm}$ than for $L = 14\,\text{mm}$, —in terms of distance scaled by the distance it takes for one eddy turnover. The degree of coupling was found to decrease with increasing model integral scale also for the present simulations. This is believed to be the second main reason for the discrepancies between mean scalar results for different model integral scales shown in Fig. 8.8.

In Fig. 8.9 the downstream evolution of the half-widths of the mean scalar profiles are compared to measurements of a 2 and a 10 mm source. Tong and Warhaft (1995) report a transition in the scaling of the half-width at about $x'/D_j \sim 5$. The thick line gives the linear scaling. The data from Tong and Warhaft (1995) suggest power-law scaling of x' with exponent ~ 0.5 beyond the transition point. However, if we consider the 4 most downstream data points, linear regression gives a 0.65-power scaling of x'.

Beyond the transition point the gradient for $L = 14$ and 28 mm approached a $\sim$0.8-power scaling with x'. Roughly the same gradient was achieved for $L = 56\,\text{mm}$ downstream $x'/D_j \sim 9$, while $L = 112\,\text{mm}$ did not reach the point of transition within the domain considered. The results from the FV computations also approached a $\sim$0.8-power scaling.

A few general comments are made about the scaling of the scalar in the turbulent jet: First, the scalar reaches its self-similar solution at a downstream location of $x'/D_j \sim 11$ at the earliest, hence it is difficult to draw any general conclusions on the scaling from the experiments. Second, strict similarity requires that the virtual origins of the scalar and the velocity are the same (Gouldin *et al.*, 1986). Third, all results with FV and LEM3D seemed to approach a 1-power scaling of x ($x = x' + x_0$). The scaling of the mean scalar evolution in a jet is also briefly discussed in Sec. 2.5.3.

The results with LEM3D for $L = 28\,\text{mm}$ agreed quite well with the near field experimental data, and the transition reported for the experiments. The point of transition between the near field and far field scaling was also in good agreement with the estimated point reported in Tab. 8.2. For larger model integral scales, the transition point was shifted downstream. The agreement with the experimental data in the near field was closest for the simulations with $L = 14$ and $L = 28\,\text{mm}$. For the $L = 112\,\text{mm}$ and $L = 56\,\text{mm}$ cases, the initial scaling appeared to follow a less steep gradient.

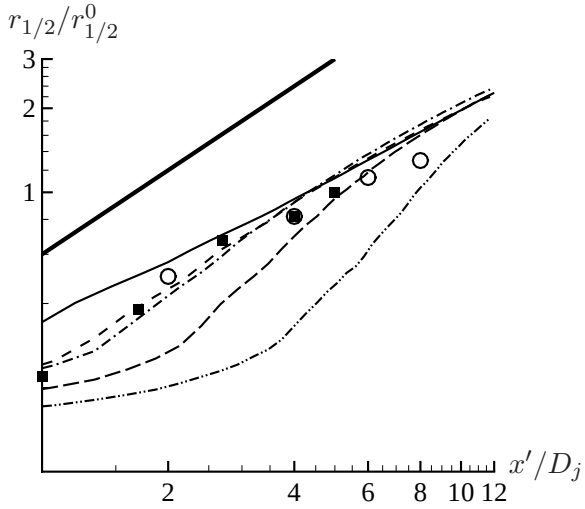

Figure 8.9: Half-width of the mean scalar profile normalized by the measured half-width at x_0 as a function of downstream position from the point source. Comparison of results from LEM3D simulations with various integral scales, FV computations and measurements of dispersion from a 2 mm (squares) and a 10 mm (open circles) ring source. See Fig. 8.8 for figure legend. The thick solid line gives the linear scaling.

As discussed in the preceding paragraphs, the discrepancies are expected to be related to the initial scaling of LEM and the degree of domain coupling by the random rotations.

Fig. 8.10 shows the effect of varying integral scale on the normalized scalar rms. The level of rms from simulations with LEM3D decreased with decreasing model integral scales. This was mainly because a reduction in integral scale increases stirring frequency, which in turn enhances small scale mixing and reduces scalar variance. The centerline normalized scalar rms plotted in Fig. 8.10 was lower than the experimental data for the LEM3D simulations for $x'/D_j >\sim 2$. In Kerstein (1992b), the model integral scale was tuned to match the scalar rms results. Tuning to match the scalar rms would in this case result in larger discrepancies with the scalar mean.

Tong and Warhaft (1995) report that an asymptotic value of about 0.2 for the normalized centerline scalar rms is approached at approximately $x'/D_j \sim 11$. This value is also observed in several heated jet experiments, which are referred in their paper. For case R8 (see Tab. 8.2) the R1-domain was extended by 60% in the streamwise direction and 25% in the lateral direction. The FV-domain was also extended to investigate the asymp-

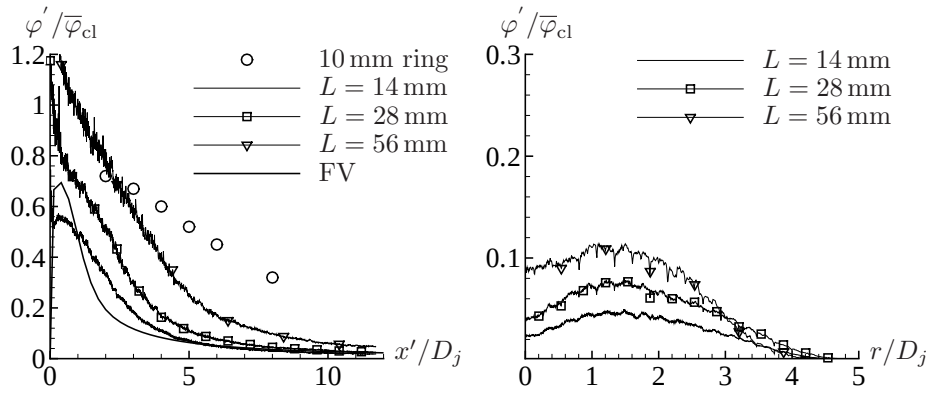

(a) Along the centerline

(b) At $x'/D_j = 8$

Figure 8.10: (a) Axial and (b) lateral profiles of normalized scalar rms. Comparison of LEM3D simulations with different choices of model integral scale. The axial profiles are in addition compared to measurements of dispersion from a 10 mm ring source and FV computations.

totic trend. The normalized centerline rms was about ∼0.02 and ∼0.01 at $x'/D_j \sim 19$ for LEM3D and FV, respectively. Neither FV, nor LEM3D did reach a constant asymptotic centerline rms value on the domains considered. The continuous decrease in asymptotic value might partly be due to that the LEM3D simulations and the FV computations were run with a single constant integral scale, wheras the integral scale in reality grows with streamwise distance from the nozzle. For LEM3D the auxiliary coupling by random rotations did most likely also play an important role in reducing the scalar rms as discussed in Sec. 6.2.7 and 8.4.2.

Figure 8.11 illustrates the rms sensitivity to the integral scale at a few more downstream positions. In these figures, the lateral coordinate was scaled by the axial position. Lateral measurement data for a 40 mm ring source and centerline values for a 10 mm ring source are compared to the computations. According to the experiments, the rms tends to decrease with ring size as discussed in Sec. 8.4.2. As shown in Fig. 8.11, the normalized rms was generally under predicted by LEM3D at all downstream locations considered.

The scalar dissipation rate model applied for FV is in inverse ratio to the integral scale (see Eq. (3.13)), hence the level of scalar rms is directly proportional[5] to l_t. On the contrary, the normalized scalar rms results

[5]That is, doubling the integral scale exactly doubles the level of rms.

from LEM3D were reduced by roughly 25% from $L = 56$ to 28 mm. The normalized scalar rms level was somewhat better captured with the FV method than with LEM3D, however, the rms close to the centerline was better predicted with LEM3D case R1.

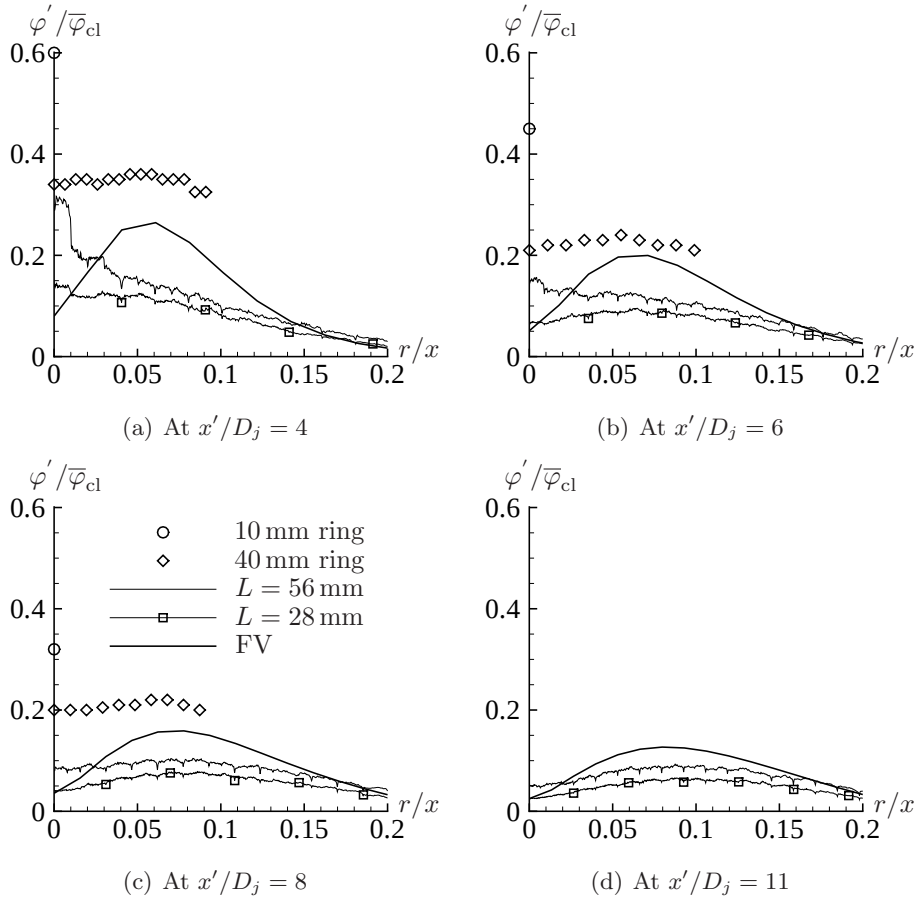

(a) At $x'/D_j = 4$

(b) At $x'/D_j = 6$

(c) At $x'/D_j = 8$

(d) At $x'/D_j = 11$

Figure 8.11: Lateral profiles of normalized scalar variance at selected axial positions. The radial coordinate is scaled by the axial position. Comparison of LEM3D simulations and FV computations with two sets of integral scales. In addition the results from measurements of dispersion from a 10 mm and a 40 mm ring are included.

8.5 Summary

The results in this chapter are summarized as follows.

- A model integral scale of $L = 28\,\text{mm}$ provided the best fit to the scalar mean evolution. A better match may possibly be achieved by implementing a spatial variation of the integral scale. For $L = 28\,\text{mm}$, the transition between the near and the far field scaling was in good agreement with the experiments. A relative rotation frequency of $\nu_r = 1$ provided adequate directional coupling, even though a larger frequency could have been applied close to the source and for the larger model integral scales.

- The scalar rms values predicted by LEM3D were significantly lower than the experimental data, and the rms was found to decline with increasing rotation frequency. These results indicate that the random rotations are an important factor in reducing the rms. One possible explanation to this behavior is that wafers with dissimilar content are brought in proximity of each other by the rotation events. This enhances the mixing of scalars and reduces the rms.

- The scalar rms was reduced with increasing 1D-resolution, because more of the small scale turbulence was resolved. Generally, the 1D-resolution that provides a grid independent solution should be chosen when possible.

- The model integral scale that gave the best match with the experimental mean scalar, gave poorer match with the scalar rms. Hence, the present jet case did not have the same flexibility as the line source case (Kerstein, 1992b) for tuning of the model integral scale.

- The 3D-resolution should generally be coarse for computational efficiency. Reducing the 3D-resolution reduced the size of the point source as well as the advective time scale. The latter further affects the rotation frequency by Eq. (4.35) if we do not compensate by increasing the relative rotation frequency correspondingly. Hence, the rotation frequency may also be subject to case dependent tuning.

Chapter 9

Summary and conclusions

9.1 Concluding remarks

This work presents a novel approach to high-fidelity simulations of non-reacting and reacting flows. The modeling concept is based on the linear eddy model (LEM) of Kerstein (1991b), which provides a fully resolved description of the turbulent mixing in one dimension. The model is denoted LEM3D and is constructed by organizing one-dimensional LEM domains in a three-array structure in the three Cartesian coordinate directions. The coupling to momentum and turbulence transport is generally provided through a separate flow solver.

LEM3D represents one among a handful of other strategies which extend the range of application for LEM to more general flows. The current work describes a coupling to RANS. However, the model is essentially also customized to coupling to unsteady large eddy simulations (LES). LEM3D is based on a strict distinction between advective and diffusive processes. This means that, instead of advecting fractional cells followed by regridding, the scalar transport by the mean flow advection and the dilatation from thermal heat release is implemented by a discrete method.

An auxiliary coupling by random rotations of 3DCVs is necessary in order to appropriately represent the physical processes in all directions in a consistent manner.

The standalone LEM3D and the coupled RANS-LEM3D require extensive computer resources. Nevertheless, the steadily growing computer capabilities in recent years have rendered the model within computational reach. The three-array structure is particularly suited for parallelization, which will become a necessity when a detailed description of chemical reactions and molecular mixing is incorporated.

9.2 Main findings

The main findings from the present work can be summarized as follows:

- The results from simulations with LEM2D and LEM3D were in reasonable overall agreement with experimental data for the line-source in homogenous turbulence and the point source in a turbulent jet. The level of agreement is regarded as promising considering the rather early stage of development of the concept.

- The joint action of processes on the individual LEM domains and the random rotations is necessary to achieve scalar spreading in all directions, including the diagonal direction. This implies that it takes some time or distance downstream from a source in order for the domains to be sufficiently coupled. It was found that the degree of directional coupling was, to a certain limit, increasing with increasing frequency of 3DCV rotations and with the time from the source scaled by the eddy turnover time.

- The random rotations of 3DCVs cause additional mean dispersion. The effect increases, to a certain limit, with increasing rotation frequency and time or distance from the source scaled by the eddy turnover time. The model suggested by Kerstein *et al.* (2007) gives an adequate estimate of the additional dispersion from rotations; however, it must be further developed for a better quantitative representation.

- The scalar rms was less with LEM2D than in a corresponding LEM1D for a point source in isotropic turbulence. The LEM3D simulations of the turbulent jet case also gave lower rms values than what is observed experimentally. The reduction is assumed to mainly stem from enhanced mixing between wafers close to 3DCV/2DCV boundaries that are brought in proximity of each other by the rotation events. Multi-point statistics such as autocorrelations were also presumably influenced by the rotations.

- Due to the random rotations, the distribution of the travel times of wafers through the computational domain is fairly broad. In other words, the random rotations add randomness to the mean translation. To some extent, the travel time is dependent of the initial position within the 3DCV. Wafers that at initially were located in the center of a 3DCV had a greater probability of travel times above the average for

the simple test case studied in Chapter 5. Vice versa, the probability of travel times less than the average was larger for wafers initially close to the 3DCV boundary.

- The discrete treatment of scalar mean flow advection represents the prescribed mean transport on average. Nonetheless, the implemented method leads to instantaneous deviations from the prescribed flow. The root mean square (rms) of these deviations, which is denoted the jitter, is significant for velocity components that are poorly resolved in terms of number of wafers. It is found that increasing the 1D-resolution M reduces the jitter. The proposed correction method is generally able to ensure a tighter control of the discrete advection and also reduces the jitter accordingly.

- The first version of the reacting LEM3D constitutes a method for thermal expansion performed as discrete dilatations. Flow solver coupling is established through the feeding of densities from LEM3D to RANS, and by supporting LEM3D with the velocity components and the turbulence diffusivity from RANS. The matching of the *non-conservative* velocities combined with the continuity equation solved in a preferential direction in LEM3D appear to introduce streamwise biased artifacts in terms of mass flow and velocity deviations between LEM3D and the flow solver.

9.3 Suggestions for further work

Although relevant comparisons to experimental results have been presented, direct numerical simulations (DNS) will accommodate the ultimate standard of verification for LEM3D. Comparison on the same basis is rendered possible by applying corresponding boundary conditions, assigning equal properties to both DNS and LEM3D, and supplying LEM3D with the mean flow advection and the turbulence diffusivities estimated from DNS. This enables comparison of higher statistical moments, multipoint statistics and scalar spectra, which will provide a valuable validation of LEM3D.

Further investigations of the effects of the random rotations should be performed. This may be pursued by considering different test cases and by analyzing the effect of the rotations on higher order moments and the scalar power spectrum. In the opinion of this author, it is too early to conclude whether if the auxiliary coupling strategy provides a sufficiently adequate representation of the physical processes. Thus, it may be worth considering

completely different strategies for coupling in the future, as for example finite difference based methods.

On the reacting LEM3D, matching the mass flux components in LEM3D and RANS may turn out to be a better option than the banking method, which matches the volume flow. The details of this approach need to be worked out in sufficient detail in future work. The streamwise bias may partly be mitigated by alternating the direction in which the continuity equation (4.17) is calculated or by performing the expansions in the direction in which they occur and adopting a checkerboard implementation.

A wide range of interesting and promising enhancement options are available for LEM3D. One is to introduce unsteadiness in the interactions between LEM3D and an unsteady RANS (URANS). Another is coupling to LES. It is also possible to embed sub-models in the wafers (Kerstein, 2004; Schmidt *et al.*, 2008) in order to reduce the number of wafers needed to resolve the domain. Another option for improvement is the adaptation of LEM3D to general RANS or LES grids.

Bibliography

Bilger, R. The structure of Diffusion Flames. *Combustion Science and Technology*, volume 13: pages 155–170, 1976.

Bird, B. R., Stewart, W. E. and Lightfoot, E. N. *Transport phenomena (re-print)*. John Wiley and Sons, New York, 1960.

Borghi, R. Turbulent combustion modeling. *Progress in Energy and Combustion Science*, volume 14, no. 4: pages 245–292, 1988.

Bradshaw, J. O. *An Introduction to Turbulence and its Measurement*. Pergamon Press, London, 1971.

Burke, S. and Schumann, T. Diffusion flames. *Industrial and Engineering Chemistry*, volume 20: pages 998–1004, 1928.

Calhoon, W., Menon, S. and Goldin, G. Comparison of reduced and full chemical mechanisms for nonpremixed turbulent H-2-air jet flames. *Combustion Science and Technology*, volume 104, no. 1-3: pages 115–141, 1995.

Cao, S. and Echekki, T. A low-dimensional stochastic closure model for combustion large-eddy simulation. *Journal of turbulence*, volume 9, no. 2: pages 1–35, 2008.

Chakravarthy, V. and Menon, S. Large-Eddy Simulation of turbulent premixed flames in the flamelet regime. *Combustion Science and Technology*, volume 162: pages 175+, 2001.

Chen, J. Y. and Chang, W. C. Modeling differential diffusion effects in turbulent nonreacting/reacting jets with stochastic mixing models. *Combustion Science and Technology*, volume 133, no. 4-6: pages 343–375, 1998.

Correa, S. M. Turbulence-chemistry interactions in the intermediate regime of premixed combustion. *Combustion and Flame*, volume 93, no. 1-2: pages 41–60, 1993.

Corrsin, S. Heat transfer in isotropic turbulence. *Journal of Applied Physics*, volume 23: pages 113–118, 1952.

Desjardin, P. E. and Frankel, S. H. Assessment of turbulent combustion submodels using the linear eddy model. *Combustion and Flame*, volume 104, no. 3: pages 343–357, 1996.

Desjardin, P. E. and Frankel, S. H. Linear-eddy modeling of nonequilibrium turbulent reacting flows with nonpremixed reactants. *Combustion and Flame*, volume 109, no. 3: pages 471–487, 1997.

Dimotakis, P. Turbulent mixing. *Annual review of fluid mechanics*, volume 37: pages 329–356, 2005.

Dopazo, C. Probability density function approach for a turbulent axisymmetric heated jet - Centerline evolution. *Physics of Fluids*, volume 18: pages 397–404, April 1975.

Dowling, D. and Dimotakis, P. Similarity of the concentration field of gas-phase turbulent jets. *Journal of fluid mechanics*, volume 218: pages 109–141, Sep 1990.

Echekki, T. Stochastic modeling of autoignition in turbulent non-homogeneous hydrogen-air mixtures. *International Journal of Hydrogen Energy*, volume 33, no. 10: pages 2596 – 2603, 2008.

Echekki, T., Kerstein, A. R., Dreeben, T. D. and Chen, J. Y. One-dimensional turbulence simulation of turbulent jet diffusion flames: Model formulation and illustrative applications. *Combustion and Flame*, volume 125, no. 3: pages 1083–1105, 2001.

Ertesvåg, I. S. *Utvikling av turbulensmodell for låge reynoldstal med likning for reynoldsspenningane og likning for karakteristisk frekvens. (In Norwegian).* Ph.D. thesis, University of Trondheim, Division of Mechanics, Thermo- and Fluiddynamics, 1991.

Ertesvåg, I. S. *Turbulent strøyming og forbrenning (In Norwegian).* Tapir akademisk forlag, Trondheim, 2000. ISBN 82-519-1568-6.

Ertesvåg, I. S. and Magnussen, B. F. The eddy dissipation turbulence energy cascade model. *Combustion Science and Technology*, volume 159: pages 213–235, 2000.

Ferziger, J. and Peric, M. *Computational methods for fluid dynamics*. Springer-Verlag, Berlin, Heidelberg New York, 2002. ISBN 3-540-42074-6.

Fox, R. O. *Computational Models for Turbulent Reacting Flows*. Cambridge University Press, Cambridge, UK, 2003. ISBN 0-521-65907-8.

Frankel, S. H., McMurtry, P. A. and Givi, P. Linear eddy modeling of reactant conversion and selectivity in turbulent flows. *Aiche Journal*, volume 41, no. 2: pages 258–266, 1995.

Goldin, G. and Menon, S. A comparison of scalar PDF turbulent combustion models. *Combustion and Flame*, volume 113, no. 3: pages 442–453, May 1998.

Goldin, G. M. A priori investigation of the constructed pdf model. *Proceedings of the Combustion Institute*, volume 30: pages 785–792, 2005. Part 1.

Goldin, G. M. and Menon, S. A scalar pdf construction model for turbulent non-premixed combustion. *Combustion Science and Technology*, volume 125, no. 1-6: pages 47–72, 1997.

Goldin, G. M., Menon, S. and Calhoon, W. H. A linear eddy mixing model fros steady non-premixed turbulent combustion. *AIAA 95-0379 33th Aerospace Sciences Meeting and Exhibit*, 1995.

Gouldin, F., Schefer, R., Johnson, S. and Kollmann, W. Nonreacting turbulent mixing flows. *Progress in Energy and combustion Science*, volume 12, no. 4: pages 257–303, 1986.

Gran, I. R. *Mathematical modeling and numerical simulation of chemical kinetics in turbulent combustion*. Ph.D. thesis, University of Trondheim, Division of Mechanics, Thermo- and Fluiddynamics, 1994.

Hewson, J. C. and Kerstein, A. R. Stochastic simulation of transport and chemical kinetics in turbulent CO/H-2/N-2 flames. *Combustion Theory and Modelling*, volume 5, no. 4: pages 669–697, 2001.

Hinze, J. O. *Turbulence, 2nd. Ed.* McGraw-Hill, New York, 1975.

Hussein, H., Capp, S. and George, W. Velocity-measurements in a high-reynolds-number, momentum-conserving, axisymmetrical, turbulent jet. *Journal of Fluid Mechanics*, volume 258: pages 31–75, Jan 1994.

Irgens, F. *Kontinuumsmekanikk (in Norwegian)*. Institutt for konstruksjonsteknikk, NTNU, Trondheim, 2004.

Kerstein, A. R. A linear-eddy model of turbulent scalar transport and mixing. *Combustion Science and Technology*, volume 60, no. 4-6: pages 391–421, 1988.

Kerstein, A. R. Linear-eddy modeling of turbulent transport. Part 2. Application to shear-layer mixing. *Combustion and Flame*, volume 75, no. 3-4: pages 397–413, 1989.

Kerstein, A. R. Linear-eddy modeling of turbulent transport. Part 3. Mixing and differential molecular-diffusion in round jets. *Journal of Fluid Mechanics*, volume 216: pages 411–435, 1990.

Kerstein, A. R. Linear-eddy modeling of turbulent transport. Part 5. Geometry of scalar interfaces. *Physics of Fluids a-Fluid Dynamics*, volume 3, no. 5: pages 1110–1114, 1991a.

Kerstein, A. R. Linear-eddy modeling of turbulent transport. Part 6. Microstructure of diffusive scalar mixing fields. *Journal of Fluid Mechanics*, volume 231: pages 361–394, 1991b.

Kerstein, A. R. Linear-eddy modeling of turbulent transport. Part 4. Structure of diffusion flames. *Combustion Science and Technology*, volume 81, no. 1-3: pages 75–96, 1992a.

Kerstein, A. R. Linear-eddy modeling of turbulent transport. Part 7. Finite-Rate chemistry and multistream mixing. *Journal of Fluid Mechanics*, volume 240: pages 289–313, 1992b.

Kerstein, A. R. One-dimensional turbulence: model formulation and application to homogeneous turbulence, sheer flows, and buoyant stratified flows. *Journal of Fluid Mechanics*, volume 392: pages 277–334, 1999.

Kerstein, A. R. One-dimensional turbulence: A new approach to high-fidelity subgrid closure of turbulent flow simulations. *Computer Physics Communications*, volume 148, no. 1: pages 1–16, 2002.

Kerstein, A. R. Development of RANS Flow Simulations Containing 1D Unsteady Sub-structure, Nov. 2004. Unpublished memo.

Kerstein, A. R. One-dimensional turbulence stochastic simulation of multiscale dynamics. In: *Lecture Notes in Physics*, volume 756, pages 291–333. Springer-Verlag, Berlin Heidelberg, 2009.

Kerstein, A. R., Cremer, M. A. and McMurtry, P. A. Scaling properties of differential molecular-diffusion effects in turbulence. *Physics of Fluids*, volume 7, no. 8: pages 1999–2007, 1995.

Kerstein, A. R., Sannan, S. and Weydahl, T. 2005-2006. Colloquium.

Kerstein, A. R., Sannan, S. and Weydahl, T. 2007. Colloquium.

Kerstein, A. R., Schmidt, R. C., Wunsch, S., Nilsen, V. and Dreeben, T. D. High-resolution modeling of multiscale transient phenomena in turbulent boundary layers. Technical Report, Sandia National Laboratories Report SAND01-8108, Combustion Research Facility, Livermore, 2001.

Klimenko, A. Y. and Bilger, R. W. Conditional moment closure for turbulent combustion. *Progress in Energy and Combustion Science*, volume 25, no. 6: pages 595–687, 1999.

Kolmogorov, A. The local structure of turbulence in incompressible viscous fluid for very large Reynolds numbers (translation). *C.R. (Doklady) Acad. Sci. URSS*, volume 30: pages 301–305, 1941.

Kreyszig, E. *Advanced Engineering Mathematics, Seventh Ed.* John Wiley and Sons, New York, 1993.

Krueger, S. K. Linear eddy modeling of entrainment and mixing in stratus clouds. *Journal of the Atmospheric Sciences*, volume 50, no. 18: pages 3078–3090, 1993.

Krueger, S. K., Su, C. W. and McMurtry, P. A. Modeling entrainment and finescale mixing in cumulus clouds. *Journal of the Atmospheric Sciences*, volume 54, no. 23: pages 2697–2712, 1997.

Launder, B. E. Second-moment closure: present... and future? *International Journal of Heat and Fluid Flow*, volume 10, no. 4: pages 282 – 300, 1989.

Magnussen, B. F. On mathematical modeling of turbulent combustion with special emphasis on soot formation and combustion. *Symposium (International) on Combustion*, volume 16: pages 719–729, 1976.

McDermott, R., Kerstein, A., Schmidt, R. and Smith, P. The ensemble mean limit of the one-dimensional turbulence model and application to residual stress closure in finite volume large-eddy simulation. *Journal of Turbulence*, volume 6, no. 31: pages 1–33, 2005.

McMurtry, P. A., Menon, S. and Kerstein, A. R. A linear eddy sub-grid model for turbulent reacting flows: Application to hydrogen-air combustion. *Proceedings of the Combustion Institute*, volume 24: pages 271–278, 1992a.

McMurtry, P. A., Menon, S. and Kerstein, A. R. A subgrid mixing model for LES of nonpremixed turbulent combustion. *AIAA 92-0234 30th Aerospace Sciences Meeting and Exhibit*, 1992b.

McMurtry, P. A., Menon, S. and Kerstein, A. R. Linear eddy modeling of turbulent combustion. *Energy & Fuels*, volume 7, no. 6: pages 817–826, 1993.

Melaaen, M. C. *Analysis of curvilinear non-orthogonal coordinates for numerical calculation of fluid flow in complex geometries.* Ph.D. thesis, University of Trondheim, Division of Thermodynamics, 1990.

Menon, S. and Calhoon, W. H. Subgrid mixing and molecular transport modeling in a reacting shear layer. *Symposium (International) on Combustion*, volume 26, no. 1: pages 59–66, 1996.

Menon, S., McMurtry, P. A., Kerstein, A. R. and Chen, J. Y. Prediction of Nox Production in a Turbulent Hydrogen-Air Jet Flame. *Journal of Propulsion and Power*, volume 10, no. 2: pages 161–168, 1994.

Menon, S., McMurtry P., K. A. R. and Chen, J. A new unsteady mixing model to predict Nox production during rapid mixing in a dual-stage combustor. *AIAA 92-0233 30th Aerospace Sciences Meeting and Exhibit*, 1992.

Menon, S., P., M. and R., K. A. A linear eddy mixing model for large eddy simulation of turbulent combustion. *Large Eddy Simulations of Complex Engineering and Geophysical Flows, B. Galperin, S. Orszag eds. Cambridge University Press*, 1993.

Oevermann, M., Schmidt, H. and Kerstein, A. Investigation of autoignition under thermal stratification using linear eddy modeling. *Combustion and Flame*, volume 155, no. 3: pages 370 – 379, 2008.

Panchapakesan, N. R. and Lumley, J. L. Turbulence Measurements in Axisymmetrical Jets of Air and Helium. Part 1. Air jet. *Journal of Fluid Mechanics*, volume 246: pages 197–223, 1993a.

Panchapakesan, N. R. and Lumley, J. L. Turbulence measurements in axisymmetrical jets of air and helium. Part 2. Helium jet. *Journal of Fluid Mechanics*, volume 246: pages 225–247, 1993b.

Pit, F., Mory, M. and Bruel, P. Modéalisation par la fonction densité de probabilité du mélange de produits inertes ou réactifs par une turbulence homogène. *18ème Congrés Francais Mécanique*, 2007. URL `http://hdl.handle.net/2042/16063`.

Poinsot, T. and Veynante, D. *Theoretical and Numerical Combustion*. R.T. Edwards, Inc., Philadelphia, USA, 2001. ISBN 1930217056.

Pope, S. B. Pdf methods for turbulent reacting flows. *Progress in Energy and Combustion Science*, volume 11, no. 1-6: pages 119–192, 1985.

Pope, S. B. *Turbulent Flows*. Cambridge University Press, Cambridge, UK, 2000. ISBN 0-521-59886-9.

Ranganath, B. and Echekki, T. One-Dimensional Turbulence-based closure for turbulent non-premixed flames. *Progress in computational fluid dynamics*, volume 6, no. 7: pages 409–418, 2006.

Ranganath, B. and Echekki, T. One-dimensional turbulence-based closure with extinction and reignition. *Combustion and Flame*, volume 154, no. 1-2: pages 23–46, Jul 2008.

Reynolds, O. On the dynamical theory of incompressible viscous fluids and the determination of the criterion. *Philosophical Transactions of the Royal Society of London. A*, volume 186: pages 123–164, 1895. ISSN 02643820. URL `http://www.jstor.org/stable/90643`.

Sankaran, V. *Sub-grid combustion modeling for compressible two-phase reacting flows*. Ph.D. thesis, Georgia Institute of Technology, School of Aerospace Engineering, 2003.

Sankaran, V., Drozda, T. G. and Oefelein, J. C. A tabulated closure for turbulent non-premixed combustion based on the linear eddy model. *Proceedings of the Combustion Institute*, volume 32, no. 1: pages 1571 – 1578, 2009.

Sankaran, V. and Menon, S. Structure of premixed turbulent flames in the thin-reaction-zones regime. *Proceedings of the Combustion Institute*, volume 28: pages 203–209, 2000. Part 1.

Sankaran, V. and Menon, S. Subgrid combustion modeling of 3-d premixed flames in the thin-reaction-zone regime. *Proceedings of the Combustion Institute*, volume 30: pages 575–582, 2005. Part 1.

Sannan, S., Kerstein, A. R. and Weydahl, T. A combustion model based on LEM3D and RANS. Technical Report, SINTEF, TR A6672, Trondheim, 2008.

Sannan, S., Weydahl, T. and Kerstein, A. R. Stochastic simulation of scalar mixing capturing unsteadiness and small-scale structure based on mean-flow properties. *Paper in preparation*, 2009.

Schmidt, R. C., Kerstein, A. R. and McDermott, R. ODTLES: A multi-scale model for 3D turbulent flow based on one-dimensional turbulence modeling. *Computer Methods in Applied Mechanics and Engineering*, volume In Press, Corrected Proof, 2008.

Schmidt, R. C., Kerstein, A. R., Wunsch, S. and Nilsen, V. Near-wall LES closure based on one-dimensional turbulence modeling. *Journal of Computational Physics*, volume 186, no. 1: pages 317–355, 2003.

Schmidt, R. C., McDermott, R. and Kerstein, A. R. ODTLES: A model for 3d turbulent flow based on one-dimensional turbulence modeling concepts. Technical Report, Sandia National Laboratories Report SAND2005-0206, Combustion Research Facility, Livermore, 2005.

Shraiman, B. and Siggia, E. Scalar turbulence. *Nature*, volume 405: pages 639–646, 2000.

Smith, T. M. and Menon, S. Model simulations of freely propagating turbulent premixed flames. *Symposium (International) on Combustion*, volume 26, no. 1: pages 299 – 306, 1996.

Smith, T. M. and Menon, S. One-dimensional simulations of freely propagating turbulent premixed flames. *Combustion Science and Technology*, volume 128, no. 1-6: pages 99–130, 1997.

Sreenivasan, K. R. Fluid turbulence. *Reviews of Modern Physics*, volume 71, no. 2: pages S383–S395, 1999. Sp. Iss. SI.

Su, C. W., Krueger, S. K., McMurtry, P. A. and Austin, P. H. Linear eddy modeling of droplet spectral evolution during entrainment and mixing in cumulus clouds. *Atmospheric Research*, volume 48: pages 41–58, 1998.

Subramaniam, S. and Pope, S. A mixing model for turbulent reactive flows based on Euclidean minimum spanning trees. *Combustion and Flame*, volume 115, no. 4: pages 487–514, Dec 1998.

Taylor, G. Diffusion by continuous movements. *Proc. London Math. Soc.*, volume s2-20: pages 196–212, 1922.

Taylor, G. Statistical theory of turbulence. *Proceedings of the Royal Society of London Series A, Mathematical and Physical Sciences*, volume 151: pages 421–444, 1935.

Tecplot. `http://www.tecplot.com/`, June 2009.

Tennekes, H. and Lumley, J. *A First Course in Turbulence*. MIT Press, Cambridge, MA, 1972. ISBN 0262200198.

Tong, C. and Warhaft, Z. Passive scalar dispersion and mixing in a turbulent jet. *Journal of Fluid Mechanics*, volume 292: pages 1–38, 1995.

Turns, S. R. *An introduction to Combustion*. McGraw-Hill Book Co, Singapore, 2000. ISBN 0072300965.

Versteeg, H. and Malalasekera, W. *An introduction to computational fluid dynamics The finite volume method*. Longman, Essex, England, 1995. ISBN 0-582-21884-5.

Veynante, D. and Vervisch, L. Turbulent combustion modeling. *Progress in Energy and Combustion Science*, volume 28, no. 3: pages 193–266, 2002.

Villermaux, E. and Innocenti, C. On the geometry of turbulent mixing. *Journal of Fluid Mechanics*, volume 393: pages 123–147, Aug 25 1999.

Viswanathan, S. and Pope, S. B. Turbulent dispersion from line sources in grid turbulence. *Physics of fluids*, volume 20, no. 10, Oct 2008.

Warhaft, Z. The interference of thermal fields from line sources in grid turbulence. *Journal of Fluid Mechanics*, volume 144: pages 363–387, 1984.

Warhaft, Z. Passive scalars in turbulent flows. *Annual Review of Fluid Mechanics*, volume 32: pages 203–240, 2000.

Warhaft, Z. Turbulence in nature and in the laboratory. *Proceedings of the National Academy of Sciences, Suppl. 1*, volume 99: pages 2481–2486, 2002.

Warnatz, J., Mass, U. and Dibble, R. *Combustion, Physical And Chemical Fundamentals, Modeling And Simulation, Experiments, Pollutant Formation*. 3rd Ed. Springer-Verlag Berlin, 2001. ISBN 3-540-67751-8.

Weydahl, T., Sannan, S., Gran, I. and Kerstein, A. Modelingmolecularmixing in turbulent reacting flows. In: *Proceedings of the European Combustion Meeting*. Chania, Crete, 2007.

White, F. M. *Viscous Fluid Flow*. McGraw-Hill, Inc., New York, second edition, 1991. ISBN 0-07-100995-7.

Wolfram, S. *The Mathematica Book, 4th ed.* Wolfram Media/Cambridge University Press, 1999. ISBN 1-57955-044-5.

Woosley, S. E., Aspden, A. J., Bell, J. B., Kerstein, A. R. and Sankaran, V. Numerical simulation of low Mach number reacting flows - art. no. 012012. volume 125 of *Journal of Physics: Conference Series*, page 12012. 2008.

Wunsch, S. Stochastic simulations of buoyancy-reversal experiments. *Physics of Fluids*, volume 15, no. 6: pages 1442–1456, 2003.

Wunsch, S. and Kerstein, A. A model for layer formation in stably stratified turbulence. *Physics of Fluids*, volume 13, no. 3: pages 702–712, 2001.

Wygnanski, I. and Fiedler, H. Some measurements in the self-preserving jet. *Journal of Fluid Mechanics Digital Archive*, volume 38, no. 03: pages 577–612, 1969.

Appendix A

Block inversion with fixed sized mapping

The first version of the LEM used block inversion with fixed size as the turbulent mapping event. The model reproduces the main features of the experiment by Warhaft (1984) with line sources in decaying grid turbulence and the uniform transverse scalar gradient in non-decaying turbulence quantitatively developed by Corrsin (1952). The step by step derivation of the fixed size eddy model with block inversion is here presented in order to give an easy to follow guide to the derivation of the more general LEM with triplet maps of multiple sizes, which is the model version applied in the present work.

A fluid cell subject to rearrangement events, generally undergoes a random walk governed by the diffusivity D_{T} (Hinze, 1975)

$$D_{\mathrm{T}} = \frac{\overline{(\Delta X)^2}}{2t}. \tag{A.1}$$

where $\overline{(\Delta X)^2}$ is the mean square displacement of a given rearrangement event. By assuming that the mapping events are statistically independent, the mean square displacement for a single event becomes $\overline{\delta^2} = \overline{N}\overline{(\Delta X)^2}$, where $\overline{N}$ is the average number of events. The mean square displacement of a single size-l mapping is expressed as $\overline{\delta^2(l)}$. For the block inversion scheme the square displacement of a single size-l event given that the fluid cell, after displacement, is a distance z from the center of the mapping event, is

$$\delta^2(l|z) = (2z)^2. \tag{A.2}$$

The mean square displacement for a single size-l event is now

$$\overline{\delta^2(l)} = \frac{1}{l}\int_{-l/2}^{l/2} \delta^2(l|z)dz = \frac{l^2}{3}. \tag{A.3}$$

The size distribution for a fixed size l^*-mapping can be written:

$$f(l) = \begin{cases} 1 & \text{if } l = l^* \\ 0 & \text{otherwise} \end{cases} \tag{A.4}$$

The total frequency of displacements is given by

$$R = \overline{N}/t = \lambda^* \int l f(l) dl = \lambda^* l^*, \tag{A.5}$$

where λ^* is the fixed event frequency parameter with unit (length^{-1}time^{-1}). With fixed block inversion size, the frequency weighted average of Eq. (A.3) is simply

$$\overline{\delta^2} = R^{-1}\lambda^* \int l f(l)\overline{\delta^2(l)} dl = \frac{l^{*2}}{3}, \tag{A.6}$$

and the turbulent diffusivity becomes

$$D_{\mathrm{T}} = \frac{\overline{N}\overline{\delta^2}}{2t} = \frac{R\overline{\delta^2}}{2} = \frac{\lambda^* l^{3*}}{6}. \tag{A.7}$$

The locus for the next mapping event is sampled from a uniform distribution and the point in time from a Poisson distribution with rate $\lambda^* X$, where X is the domain size. This completes the description of the LEM with fixed size block inversion scheme.

The procedure for the derivation of the expressions for triplet maps is similar, however some differences exists. The eddy size l is not fixed, and the $f(l)$ distribution scales as $l^{4/3}$. By normalization we arrive at the distribution given in Eq. (3.16). The block mapping (A.2) is replaced by the triplet mapping, which yields the conditional mean square displacement

$$\begin{aligned} \delta^2(l|z) &= (4z)^2 && 0 \le |z| \le \frac{l}{6} \\ \delta^2(l|z) &= (l - 2|z|)^2 && \frac{l}{6} \le |z| \le \frac{l}{2}. \end{aligned} \tag{A.8}$$

See Kerstein (1991b) for a complete description of the derivation.

Appendix B

Momentum equation and Reynolds stresses in cylindrical coordinates

In the following section the momentum equations with turbulent transport are given in axis symmetrical cylindrical coordinates. Incompressible flow and constant properties are assumed. If we split velocities and pressure in a mean and fluctuating part, we get for the momentum equation in the x- and r-direction after averaging:

$$\begin{aligned}\frac{\partial}{\partial t}(\overline{u}_x)+\frac{1}{r}\frac{\partial}{\partial r}(r\overline{u}_x\overline{u}_r)+\frac{\partial}{\partial x}(\overline{u}_x\overline{u}_x)=-\frac{1}{\rho}\frac{\partial\overline{p}}{\partial x}+\\ \frac{1}{r}\frac{\partial}{\partial r}\left(r\overline{\tau}_{rx}-r\overline{u_x^{'}u_r^{'}}\right)+\frac{\partial}{\partial x}\left(\overline{\tau}_{xx}-\overline{u_x^{'}u_x^{'}}\right)\end{aligned} \tag{B.1}$$

and

$$\begin{aligned}\frac{\partial}{\partial t}(\overline{u}_r)+\frac{1}{r}\frac{\partial}{\partial r}(r\overline{u}_r\overline{u}_r)+\frac{\partial}{\partial x}(\overline{u}_r\overline{u}_x)=-\frac{1}{\rho}\frac{\partial\overline{p}}{\partial r}+\\ \frac{1}{r}\frac{\partial}{\partial r}\left(r\overline{\tau}_{rr}-r\overline{u_r^{'}u_r^{'}}\right)+\frac{\partial}{\partial x}\left(\overline{\tau}_{xr}-\overline{u_r^{'}u_x^{'}}\right)\end{aligned} \tag{B.2}$$

Thus, we have the following Reynolds stress tensor

$$\begin{pmatrix}-\overline{u_x^{'}u_r^{'}} & -\overline{u_x^{'}u_x^{'}}\\ -\overline{u_r^{'}u_r^{'}} & -\overline{u_r^{'}u_x^{'}}.\end{pmatrix} \tag{B.3}$$

Following Boussinesq, the Reynolds stresses in the x-direction are modeled as

$$\begin{aligned} -\overline{u_x' u_r'} &= \nu_t \left(\frac{\partial \overline{u}_x}{\partial r} + \frac{\partial \overline{u}_r}{\partial x} \right), \\ -\overline{u_x' u_x'} &= 2\nu_t \left(\frac{\partial \overline{u}_x}{\partial x} \right) - \frac{2}{3} k, \end{aligned} \tag{B.4}$$

where k is the turbulence kinetic energy.

Appendix C

Mathematical floor

The mathematical floor of a value a is defined as the nearest integer number that is smaller than a

$$\lfloor a \rfloor \equiv \max[n \in \boldsymbol{Z} | n \leq a]. \tag{C.1}$$